



Durham E-Theses

Deposition and characterisation of sputtered Nickel manganate thin films

Basu, Arnab

How to cite:

Basu, Arnab (2002) *Deposition and characterisation of sputtered Nickel manganate thin films*, Durham theses, Durham University. Available at Durham E-Theses Online: <http://etheses.dur.ac.uk/4112/>

Use policy

The full-text may be used and/or reproduced, and given to third parties in any format or medium, without prior permission or charge, for personal research or study, educational, or not-for-profit purposes provided that:

- a full bibliographic reference is made to the original source
- a [link](#) is made to the metadata record in Durham E-Theses
- the full-text is not changed in any way

The full-text must not be sold in any format or medium without the formal permission of the copyright holders.

Please consult the [full Durham E-Theses policy](#) for further details.

Deposition and Characterisation of Sputtered Nickel Manganate Thin Films

The copyright of this thesis rests with the author.
No quotation from it should be published without
his prior written consent and information derived
from it should be acknowledged.

By

Arnab Basu, BEng(Hons)

*A thesis presented in candidature for the degree of Doctor of
Philosophy in the University of Durham*

Department of Physics

November 2002



24 MAR 2003

Thesis

2002

BAS

ABSTRACT

This work investigates the structural and electrical properties of both bulk and rf magnetron sputtered thin films of spinel structured $Ni_xMn_{3-x}O_{4+\delta}$ material system. The distribution of the LDOS of the thin films is also studied using STS. A rf magnetron sputtering system capable of reactive sputtering in a range of argon/oxygen ambients was designed, constructed and commissioned in the first phase of this work. The system was optimised in terms of the effect of various process parameters on the growth rate using factorial experimental design technique. Incident power, substrate to target distance and oxygen percentage in the ambient was found to be the most significant.

The effect of different sintering temperatures was investigated for five different compositions of the $Ni_xMn_{3-x}O_{4+\delta}$ material system. Monophase material could not be prepared without prolonged annealing at 800°C after sintering at higher temperatures. This was in contradiction with the published phase diagram of the material and hence a modified scheme was proposed. The lattice parameter of the spinel phase increased with decreasing nickel content. Grain growth was found to be exponentially dependent on the sintering temperature. The $R-T$ characteristics below 300K followed the Shklovskii and Efros VRH model ($T_0 \sim 2 \times 10^5$ K) and a change to the NNH model ($\Delta E \sim 330$ meV) was observed above 300K. The resistivity of the material was dependent on both the ratio of $Ni:Mn$ and the oxygen stoichiometry (varying from 1.2 Kohm-cm up to 30 Kohm-cm).

The as-deposited films showed poor crystallinity, hence post deposition annealing at 800°C was required. The microstructure and the degree of preferred orientation were found to be dependent on the substrate temperature and post deposition annealing. The lattice parameter of the films was lower than the target. The NNH model best described the $R-T$ characteristics of the films deposited at low oxygen content <2.5% ($\Delta E \sim 360$ meV) whereas films deposited at higher oxygen content could be better described by the Shklovskii and Efros VRH model ($T_0 \sim 2.4 \times 10^5$ K). The resistivity of the films decreased with increasing oxygen in the ambient in the as-deposited state, however after annealing the resistivity of all the films became similar and much lower than the target.

The distribution of the LDOS of the films, using STS, was found to be parabolic and in agreement with the assumption in the Shklovskii and Efros VRH model. Additional features were observed in the LDOS with increasing temperatures ($\sim \pm 0.15$ eV and ~ 1.6 eV) however the changes were completely reversible with temperature.

DECLARATION

I declare that all the work in this thesis was carried out by the candidate unless stated otherwise. I also declare that none of this work has previously been submitted for any degree and that it is not being submitted for any other degree.



Dr A W Brinkman
Supervisor



Arnab Basu
Candidate

The copyright of this thesis rests with the author. No quotation from it should be published without prior written consent and information derived from it should be acknowledged.

ACKNOWLEDGEMENTS

I would like to take this opportunity to thank all the people who helped in the preparation of the thesis, specially my supervisor Dr A W Brinkman, to whom I wish to express my appreciation and gratitude for the valuable guidance and support. I would also like to thank Prof B K Tanner, Dr T P A Hase, Dr I Terry and Dr K Durose for all the valuable discussions, help and encouragement throughout the study.

I wish to extend my thanks to the technical staff of the department, especially Mr P Armstrong, Mr M Robertshaw and Mr S Lishman of the mechanical workshop for their effort and commitment during the construction of the sputtering system. I would also like to thank Mr John Dobson for all his enthusiasm and efforts to find various equipment and Mr N Thompson, Mr D Pattison, Mr G Dodsworth, Mr C Mullaney, Mr A Hunter and Mr J Scott for their technical support.

I would like to thank all the members of AMRI, Northumbria University in particular Prof P K Datta Dr Z Klusek, Pawel and Sebastian for carrying out the STM/STS experiments and all the help and guidance provided throughout the study. I thank Dr R Gover, Dr J S O Evans and all the members of the Solid State group in the Chemistry Department for allowing me to carry out the XRD work and the guidance provided with the analysis. I would like to thank Mr A Yates for all his help with the SEM.

I also thank all the past and present members of the research group Paul, Saleh, David, Mike, Ben, Guillaume, Nick, Harpreet, Andrew, Steve and Keriya for providing a great atmosphere in which to work and Rainer for all those valuable discussions and ideas.

I wish to express my thanks to Fujitsu Ltd and ATSI Inc for providing various pieces of equipment including rf power supplies, impedance matching circuitry, etc. I also acknowledge the financial support provided by the University of Durham and the provision of the ORS scholarship by the CVCP council.

On a more personal note, I would like to thank all my friends, specially Obu, Rose, Octav and Kelly and my family, in particular my parents back in India and my parent-in-laws in Belgium for their constant encouragement. Finally, special thanks goes to my wife, Beatrijs for her patience, understanding and support over the last three years and for all the help provided in preparing this thesis.

ABBREVIATIONS

AFM	<i>Atomic force microscope</i>
CITS	<i>Current imaging tunneling spectroscopy</i>
DC	<i>Direct current</i>
EBIC	<i>Electron beam induced current</i>
EDAX	<i>Energy dispersive analysis of x-rays</i>
FCC	<i>Face centred cubic</i>
FED	<i>Factorial experimental design</i>
FWHM	<i>Full width half maximum</i>
LDOS	<i>Local density of states</i>
LHS	<i>Left hand side</i>
NNH	<i>Nearest neighbour hopping</i>
NTCR	<i>Negative temperature coefficient of resistance</i>
RF	<i>Radio frequency</i>
RHS	<i>Right hand side</i>
R-T	<i>Resistance-temperature</i>
RTD	<i>Resistance temperature detectors</i>
SEM	<i>Scanning electron microscope</i>
STM	<i>Scanning tunneling microscope</i>
STS	<i>Scanning tunneling spectroscopy</i>
VRH	<i>Variable range hopping</i>
XAF	<i>Atomic number, absorption and fluorescence</i>
XPS	<i>Photoelectron spectroscopy</i>
XRD	<i>X-ray diffraction</i>

CONTENTS

Chapter 1 Introduction

1.1	Introduction	1
1.2	Historical Background	3
1.3	Motivation of Present Work	4
1.4	Scope of Present Work	5
1.5	Other Work	7
1.6	References	8

Chapter 2 Scientific Background

2.1	Introduction	9
2.2	Crystal Structure	9
2.3	Phase Diagram	13
2.4	Synthesis Routes	15
2.5	Conduction Models	16
2.5.1	NNH MODEL	17
2.5.2	MOTT VRH MODEL	18
2.5.3	SHKLOVSKII AND EFROS VRH MODEL	21
2.5.4	OTHER MODELS	23
2.6	Thin Films of Nickel Manganate	25
2.7	Conclusions	28
2.8	References	30

Chapter 3 Construction and Calibration of the RF Magnetron Sputtering System

3.1	Introduction	34
3.2	Theoretical Background	35
3.2.1	SPUTTERING	35

3.2.2	MAGNETRON SPUTTERING	35
3.2.3	RF SPUTTERING	36
3.2.4	REACTIVE SPUTTERING	37
3.3	Description of the Sputtering System	38
3.3.1	VACUUM SYSTEM	39
3.3.2	TARGET AND SUBSTRATE HANDLING SYSTEM	40
3.3.3	GAS HANDLING SYSTEM	42
3.3.4	TEMPERATURE CONTROL	43
3.4	Calibration of the Sputtering System	45
3.4.1	EFFECT OF TIME	46
3.4.2	EFFECT OF SUBSTRATE TO TARGET DISTANCE	47
3.4.3	EFFECT OF OXYGEN CONTENT IN THE AMBIENT	48
3.4.4	EFFECT OF SUBSTRATE TEMPERATURE	49
3.4.5	EFFECT OF PRESSURE	50
3.4.6	EFFECT OF POWER	51
3.5	Factorial Experimental Design Technique	52
3.5.1	MAIN EFFECTS	54
3.5.2	INTERACTION EFFECTS	56
3.5.3	HALF NORMAL PLOT	61
3.6	Conclusions	62
3.7	References	65

Chapter 4 Structural Properties of Bulk $Ni_xMn_{3-x}O_{4+\delta}$ Material System

4.1	Introduction	67
4.2	Experimental	68
4.2.1	CERAMIC PREPARATION	68
4.2.2	SCANNING ELECTRON MICROSCOPY	69
4.2.3	X-RAY DIFFRACTION	70
4.2.4	WEIGHT AND DIMENSION MEASUREMENT	70
4.3	Crystal Structure	70
4.3.1	PHASE ANALYSIS	71
4.3.2	ELEMENTAL ANALYSIS	81

4.4	Microstructure	84
4.4.1	GRAIN SIZE DISTRIBUTION	85
4.5	Macroscopic Aspects of the Material	91
4.5.1	SHRINKAGE	91
4.5.2	POROSITY	92
4.6	Conclusions	93
4.7	References	96

Chapter 5 Electrical Properties of Bulk $Ni_xMn_{3-x}O_{4+\delta}$ Material System

5.1	Introduction	98
5.2	Experimental	99
5.2.1	CONTACT FABRICATION	99
5.2.2	<i>R-T</i> MEASUREMENT SYSTEM	99
5.3	Electrical Characterisation	100
5.3.1	MOTT VRH MODEL	102
5.3.2	SHKLOVSKII AND EFROS VRH MODEL	103
5.3.3	ANALYSIS OF ' <i>p</i> '	106
5.3.4	RESISTIVITY	110
5.4	Conclusions	116
5.5	References	118

Chapter 6 Structural and Electrical Properties of $Ni_xMn_{3-x}O_{4+\delta}$ Thin Films

6.1	Introduction	119
6.2	Experimental	120
6.2.1	FILM DEPOSITION AND HEAT TREATMENT	120

6.2.2	ATOMIC FORCE MICROSCOPY	122
6.2.3	X-RAY DIFFRACTION	123
6.2.4	THICKNESS MEASUREMENT	123
6.2.5	CONTACT FABRICATION	123
6.2.6	<i>R-T</i> MEASUREMENT SYSTEM	124
6.3	Structural Characterisation	125
6.3.1	CRYSTAL STRUCTURE	125
6.3.2	MICROSTRUCTURE	132
6.4	Electrical Characterisation	137
6.4.1	RESISTIVITY	137
6.4.2	CHARGE TRANSPORT PROPERTIES	139
6.4.2.1	Mott VRH Model	140
6.4.2.2	Shklovskii and Efros VRH Model	141
6.4.2.3	NNH Model	143
6.4.3	ANALYSIS OF ' <i>p</i> '	144
6.5	Conclusions	148
6.6	References	151

Chapter 7 Electronic Properties of $Ni_xMn_{3-x}O_{4+\delta}$ Thin Films

7.1	Introduction	153
7.2	Theoretical Background	154
7.2.1	SCANNING TUNNELING MICROSCOPY	154
7.2.2	SCANNING TUNNELING SPECTROSCOPY	156
7.2.3	CURRENT IMAGING TUNNELING SPECTROSCOPY	158
7.3	Experimental	159
7.4	Effect of Post Deposition Annealing	160
7.5	Temperature Dependent Spectroscopy	163
7.6	Conclusions	167
7.7	References	169

Chapter 8 Conclusions and Scope for Future Work

8.1	Conclusions	170
8.2	Scope for Future Work	178
8.3	References	181

Appendix – I	List of Publications	I-i
---------------------	-----------------------------	------------

Introduction

1.1 INTRODUCTION

In today's world temperature is possibly the second most measured variable after time. As more and more emphasis is put on improving the quality of life and increasing personal levels of comfort, there is an ever-increasing demand for new technologies and products. Although it is not always apparent, most of the electrical gadgets used in everyday life, as diverse as hair driers, cash machines, televisions, etc. have some form of temperature sensor incorporated within them [1]. In medical science temperature measurement also plays a very important role [2]. Apart from the obvious measuring of the body temperature, most medical appliances such as x-ray and sterilisation machines all need some form of temperature monitoring and detection.

The devices that are commonly used as temperature sensors can be broadly divided into four categories [3]:

- (1) Resistance temperature detectors (RTD): these are wire windings or thin film serpentines commonly of metals such as copper, nickel or platinum, which



exhibit a change in resistance with a change in temperature. The response from these devices is linear, repeatable and stable. Platinum RTD are the most stable of all and are used as the standard international temperature reference. However these devices are generally quite expensive, which makes them unsuitable for high volume commercial applications.

- (2) Thermocouples: these devices consist of wires of two dissimilar metals welded together at both ends and any temperature difference between the junctions causes a change in the voltage between the two wires. Although the temperature range of application of these devices is quite large, the output voltages are very small and are highly susceptible to noise pick up by the wire loop.
- (3) Silicon based devices: these are based on silicon transistors, which show temperature dependence of the voltage output. These are relatively low cost devices with a higher output voltage than the thermocouples and hence they are quite widely used.
- (4) NTCR thermistors: these are perhaps the most widely used temperature sensing devices, due to the low cost and high sensitivity ($\sim 4\% / ^\circ\text{C}$). They are made from metal oxide ceramics and can be quite small in size, which makes it easy to incorporate them in other appliances. The resistance of these devices decreases with increasing temperature.

The global temperature sensor market in 2001 was estimated by Ernst & Young to be worth £840 million, out of which NTCR thermistors accounted for 37% of the market, which corresponds to \sim £310 million. The market has shown a steady growth of about 7.5% per annum since 1994 without any signs of saturation. The current size of the

market along with trends of steady growth provides the drive to improve the quality of the sensors. Furthermore the applications can be expected to become more demanding with progress in other technologies.

1.2 HISTORICAL BACKGROUND

The name thermistor is derived from thermally sensitive resistors. Michael Faraday, better known for his work in electromagnetic induction and electrochemistry, reported a negative temperature coefficient of resistance of Ag_2S in 1833 [4], which can be considered the first report on NTCR thermistors. However due to difficulties in production and limited applications, thermistors were not produced commercially until a century later. A lot of development work was carried out in the Phillips laboratories in The Netherlands [5] and the Bell telephone laboratory [6] in the USA during the 1940s to find ways of producing consistent and repeatable products. At that time most of the thermistors were produced in the form of discs and the tolerances were much higher than those acceptable today. The material systems used in the 1940s were either NiO and CoO or the $NiO-Co_2O_3-Mn_2O_3$ system.

In the 1950s and 1960s the driving force behind the progress in the technology was the increasing demand from the aerospace industry for more stable and accurate devices. This led to improvements in the materials and also to the development of the bead and encapsulated thermistors, which were more robust.

The increased reliability of the thermistors, compared to the early years of development led to its application in the health care industry in the form of electronic thermometers. Thermistors also provided an opportunity to use disposable temperature measurement devices, as they were now cheap to produce. The use of thermistors has continued to

grow throughout the 1980s and 1990s in the automotive, food processing, medical and telecommunication sectors.

Nickel manganate is one of the most important materials used in the production of thermistors and has been since the very beginning. Over time other metallic ions such as cobalt and copper have been added to the nickel manganate system to control its performance both in terms of long term stability, reproducibility and operating characteristics.

1.3 MOTIVATION OF THE PRESENT WORK

Thermistors of $Ni_xMn_{3-x}O_{4+\delta}$ are mainly produced as bulk devices in the form of beads, discs or tape casted chips [7, 8]. The properties of the thermistors depend in a poorly understood way on process variables such as the sintering temperature and time. The composition of the material is also very important, as it directly affects the electrical properties. The electrical conduction in nickel manganate is believed to result from phonon assisted hopping of electrons from Mn^{3+} to Mn^{4+} in the lattice. Although these devices have been produced commercially for the last fifty years the electrical conduction process is still not fully understood, as evidenced by often contradictory claims in the literature.

These devices are porous and the poor intergranular contact often leads to a lack of reproducibility. With the advancements in the thin film technology, one possible way to resolve this problem is by producing thin films with electrical properties similar to the bulk and in the 1990s some researchers produced thin films of nickel manganate, which exhibited promising results.

This work is aimed at producing thin films of nickel manganate using rf magnetron sputtering from a ceramic target and investigating the electrical properties in order to provide a better understanding of the charge transport mechanisms. This project will also attempt to shed some light on the effects of the composition of the $Ni_xMn_{3-x}O_{4+\delta}$ material system and the processing parameters on the electrical properties of bulk materials.

1.4 SCOPE OF PRESENT WORK

As mentioned in the previous section, this thesis is mainly devoted to investigating the electrical charge transport mechanism of the nickel manganate material system in both bulk and thin film form. This chapter will have provided a brief background of the thermistors and their applications. In addition, other commonly used temperature sensors were reviewed with their respective advantages and disadvantages.

Chapter 2 reviews what is known about the material including information about the crystal structure and the importance of the charge distribution in the different lattice sites. The chapter will also include a brief outline of the underlying theories that have been used throughout the thesis to explain and discuss the experimental findings. The conduction models commonly used to explain the charge transport in this kind of materials will be discussed and the various assumptions will be highlighted. Finally a short account of work undertaken by other researchers will be presented.

Chapter 3 contains the description of the rf magnetron sputtering system that was built during the course of this project. It also present results from a study of the effect of the various process parameters on the growth rate and discusses the statistical importance of

the parameters on the growth rate by analysing a factorial experimental design experiment.

The following two chapters (4 and 5) examine the results of a study of the bulk nickel manganate system undertaken as a part of the development of a suitable ceramic target. Chapter 4 is devoted to the presentation and discussion of both macroscopic and microscopic aspects of the structure of the material along with the effect of the heating regimes on the formation of nickel manganate. This is followed in chapter 5 by the electrical characterisation of the material and an attempt to identify the most suitable charge transport model.

Results from the study of nickel manganate thin films will be presented and discussed in the next two chapters. Chapter 6 is concerned with the structural and electrical properties of the films, together with the effect of the oxygen content in the sputtering environment on the electrical properties. The $R-T$ characteristics are also presented and discussed in terms of the various conduction models. Chapter 7 will be devoted to the scanning tunneling spectroscopy results of thin films. This is believed to be the first attempt to study the electronic structure of the material and also a first report of STS carried out above room temperature.

The concluding chapter will provide a summary of all the results presented and discussed in the previous chapters and will present some ideas on how to take this project further.

1.5 OTHER WORK

During the period of study a number of papers relating to the properties of nickel manganate have been submitted for publication and published [9-13]. Furthermore, some initial work was carried out on bismuth oxide based material suitable for high temperature thermistor applications and a paper was published [14]. Work relating to the bismuth based thermistor material and this thesis were presented at the EMRS Spring Meeting 2000, Strassbourg and the 8th International Conference on Electronic Ceramics and their Applications, Electroceramics VIII, 2002, Rome.

1.6 REFERENCES

- [1]. Sensors, www.sensorsmag.com/resources/businessdigest/sbd0301.shtml.
- [2]. Sachse, H.B. (1975) *Semiconducting temperature sensors and their applications*. John Wiley & Sons, New York.
- [3]. <http://bsunsrv1.kek.jp/~moffitt/temptute1.html>.
- [4]. Hill, D., Tuller, H. (1991) *Ceramic sensors: theory and practice, ceramic material for electronics*. Marcel Dekker Inc, New York.
- [5]. Macklen, E.D. (1979) *Thermistors*. Electrochemical Publications, Glasgow.
- [6]. Sensors, C. (2002) www.globalspec.com/cornerstone/ref/negtemp.html.
- [7]. Systems, I.S. www.thermal.invensys.com/product.
- [8]. www.electronics-cooling.com/html/body_sensors_pages_6.html.
- [9]. Basu, A., Brinkman, A.W., Klusek, Z., Datta, P.K., Kowalczyk, P. *In situ study of the effect of temperature on the electronic structure of $Ni_xMn_{3-x}O_{4+\delta}$ thin films using scanning tunnelling spectroscopy*, (2002) *Journal of Applied Physics*, **92**, 4123.
- [10]. Basu, A., Brinkman, A.W., Hase, T.P.A., Klusek, Z., Datta, P.K., Pierzgalski, S. *Effect of substrate temperature on the structural properties of rf magnetron sputter deposited $Ni_xMn_{3-x}O_{4+\delta}$ thin films*, (2002) *Thin Solid Films*, **In submission**.
- [11]. Basu, A., Brinkman, A.W., Schmidt, R. *Effect of oxygen partial pressure on the NTCR characteristics of sputtered $Ni_xMn_{3-x}O_{4+\delta}$ thin films*, (2002) *Journal of European Ceramic Society*, **In Press**.
- [12]. Schmidt, R., Basu, A., Brinkman, A.W. *Production of NTCR thermistor devices based on $NiMn_2O_{4+\delta}$* , (2002) *Journal of European Ceramic Society*, **In Press**.
- [13]. Basu, A., Brinkman, A.W., Schmidt, R., Klusek, Z., Kowalczyk, P., Datta, P.K. *A study of electronic states of $Ni_xMn_{3-x}O_{4+\delta}$ thin films using scanning tunneling microscopy and current imaging tunneling spectroscopy*, (2002) *Journal of European Ceramic Society*, **In Press**.
- [14]. Basu, A., Brinkman, A.W., Hashemi, T. *NTC characteristic of bismuth based ceramic at high temperature*, (2001) *International Journal of Inorganic Materials*, **3**, 1219.

Scientific Background

2.1 INTRODUCTION

This chapter is intended to provide a summary of the scientific principles that are relevant to understand and explain the various experimental results in the ensuing chapters. The structure of $Ni_xMn_{3-x}O_{4+\delta}$ will first be discussed, to be followed by a review of the phase diagram for the material system. The latter was used to determine the various compositions and the heat treatments used in chapter 4. The conduction models commonly applied in the literature to explain the charge transport properties will then be presented and discussed. Finally a brief review will be given of studies on nickel manganate thin films by other researchers.

2.2 CRYSTAL STRUCTURE

Nickel manganate crystallises in a spinel structure, which derives its name from the mineral and precious stone, spinel [1]. Ceramic spinels are an important and structurally interesting class of material and find a wide range of applications in industry. Chemically, spinels are very diverse and are formed by the crystallisation of the manganates, aluminates, titanates, ferrates, etc. of divalent metals such as cadmium,

cobalt, chromium, nickel, magnesium, zinc, etc. [2]. Spinels are normally described by the general formula AB_2O_4 where A represents one or more divalent metals which form oxides of the type AO and B represents one or more trivalent metals which form oxides of the form B_2O_3 . The structure is based on the oxygen atoms forming a FCC sub lattice containing both tetrahedral and octahedral interstices. The tetrahedral sites of this array are occupied by the A -atoms and the B -atoms are found in the octahedral sites [3]. Figure 2.1 (a) shows a spinel structure and figure 2.1 (b) illustrates the octahedral

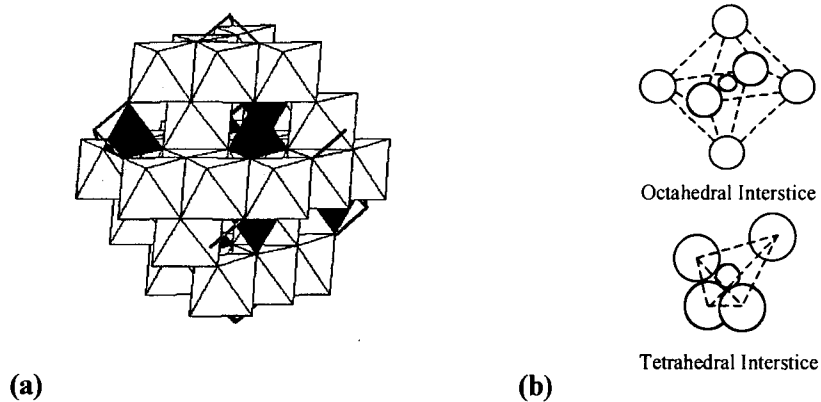


Figure 2.1 A schematic representation of (a) a unit cell of a spinel structure and (b) an octahedral and a tetrahedral interstices

and tetrahedral interstices. A spinel unit cell has 32 oxygen atoms, 8 atoms of A and 16 atoms of B giving a total of 56 atoms in a unit cell. There are 64 tetrahedral sites and 32 octahedral sites in a spinel unit cell. So the occupancy of the tetrahedral sites is $1/8$ and that of the octahedral sites is $1/2$ [4]. The set of occupied tetrahedral sites is called the A sublattice and each site is called an A -site and the set of occupied octahedral sites is called the B sublattice and each site is called a B -site.

A normal spinel unit cell can be illustrated by eight different layers, which are superimposed on each other [5]. The second, fourth, sixth and eighth layer contain the tetrahedral cations while the other four layers contain the octahedral cations and the oxygen atoms. The distribution of the cations in the crystal structure is a very important

factor to be considered when studying the structure of nickel manganate [6]. The Ni^{2+} ion has a strong preference for the octahedral (B) site, which results in a partially inverted structure and can be expressed as



where the square brackets indicate the occupancy in the octahedral sites, ν is the inversion parameter which takes the value 0 for a normal spinel and 1 for an inverse spinel [7]. When the value of ν is in between 0 and 1, it is referred to as a partially inverted spinel. In 1957, Sinha et. al. [8] reported, on the basis of x-ray diffraction studies, the value of ν to be 0 implying that the nickel ions occupied only A -sites in the crystal structure. Further support for this argument appeared to come from neutron diffraction experiments by Azaroff et. al. [7] in 1959. However, in 1961 O'keefe [9] proposed the value of ν to be 0.71 with the chemical formula



Then in 1962 Larson et. al. [10] proposed, on the basis of electrical conductivity analysis, the value of ν to be 1, which implied the structure to be a complete inverse spinel. The formula they proposed was

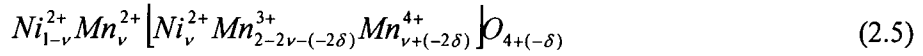


Boucher et. al. [11] found that the value of ν depended on the material preparation with $\nu = 0.74$ for samples quenched from 940°C, and $\nu = 0.9$ for material cooled slowly in the furnace. Brabers et. al. [12], using x-ray photoelectron spectroscopy, demonstrated

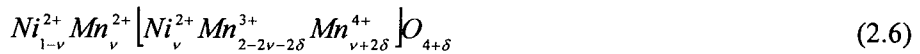
the existence of Mn^{2+} and Mn^{4+} in the material. Recently in 1996, Asbrink et. al. [13], using single crystals of nickel manganate, found the value of the inversion parameter to be 0.87. The formula proposed is shown below



Brabers found that the inversion parameter of material quench cooled from higher temperatures changed when reheated above 450°C and attributed it to cation migration from the octahedral sites. Macklen [14] found occurrence of oxygen loss when heated above 900°C in air. However when heated in an oxygen deficient atmosphere this loss occurred even at lower temperatures. When δ amount of oxygen from the molecule is lost from the system 2δ tetravalent manganese ions are converted into trivalent ions to maintain charge neutrality and the resulting cation distribution can be expressed as



However Feltz and Topfer [15] found that there was possibility of excess oxygen in the material, in which case the charge distribution could be described as



The distribution of the cations in the structure is important as it affects the conductivity of the material and it can be altered by either varying the amount of nickel or manganese in the system or by changing the oxygen stoichiometry. Hence it is possible to alter the conductivity by controlling these parameters and this will be discussed in chapter 5 and 6.

The lattice parameter of stoichiometric nickel manganate was reported to be $8.399 \pm 0.002 \text{ \AA}$ by Wickham [16] from x-ray diffraction studies. He also reported that the lattice constant increased with decreasing nickel content and for the composition $Ni_{0.75}Mn_{2.25}O_4$ the lattice constant was found to be $8.435 \pm 0.002 \text{ \AA}$. Brieu et. al. [17], using electron diffraction, found the lattice parameter of $Ni_{0.75}Mn_{2.25}O_4$ to be $8.43 \pm 0.001 \text{ \AA}$. However, Asbrink et. al. [13] found the lattice parameter of stoichiometric nickel manganate to be $8.379 \pm 0.001 \text{ \AA}$, which was lower than the value found by Wickham. Boucher et. al. [11] found that the lattice parameter a changed with varying inversion parameter ν in the following way

$$a = 8.441 - 0.057\nu \quad (2.7)$$

The inversion parameter was also found to be dependent on sintering temperature.

2.3 PHASE DIAGRAM

The phase diagram of $NiO-Mn_2O_3-O_2$ proposed by Wickham [16] in 1964 is shown in figure 2.2. The material was prepared by co-precipitating acetate precursors with oxalic

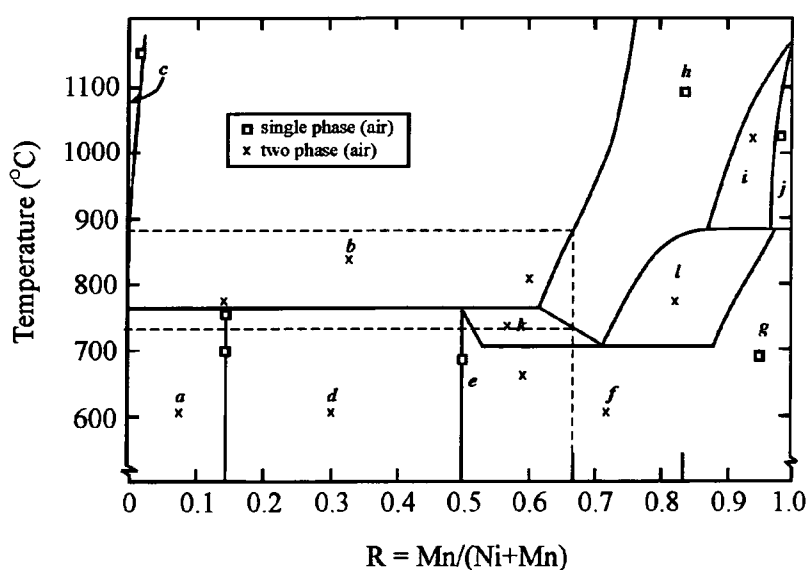


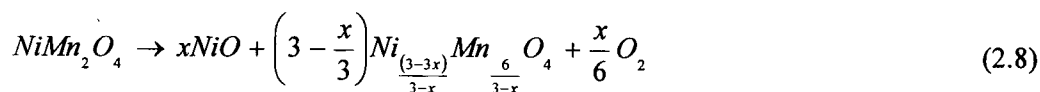
Figure 2.2 Phase diagram of the $NiO-Mn_2O_3-O_2$ material system reproduced from reference [16]

acid, which after drying were fired in air to obtain the compounds. The phases were identified using x-ray diffraction. The details of all the different phases present in each region are shown in table 2.1. However the region of interest for the current project is where the spinel phase exists without any other secondary phases (*h*). In stoichiometric nickel manganate the value of *R* is 0.667 which is shown by the broken lines (figure 2.2). The horizontal broken lines indicate the temperature range (730°C and 875°C) in which single phase $NiMn_2O_4$ can be obtained. Above 875°C *NiO* precipitates out

Region in the phase diagram	Phases present
<i>a</i>	<i>NiO</i> and cubic Ni_6MnO_8
<i>b</i>	Spinel $Ni_{3-x}Mn_xO_4$ and rock salt $Ni_{1-s}Mn_sO$
<i>c</i>	$Ni_{1-s}Mn_sO$
<i>d</i>	Cubic Ni_6MnO_8 and Ilmenite $NiMnO_3$
<i>e</i>	Ilmenite $NiMnO_3$
<i>f</i>	Ilmenite $NiMnO_3$ and Mn_2O_3
<i>g</i>	Ilmenite $NiMnO_3$ and co-existence of Mn_2O_3 and Mn_3O_4
<i>h</i>	Cubic spinel at $R < 0.807$ and spinel with tetragonal distortion at $R > 0.807$
<i>i</i>	Cubic and tetragonal spinel
<i>j</i>	Tetragonal spinel with composition close to Mn_3O_4
<i>k</i>	Spinel $Ni_{3-x}Mn_xO_4$ and ilmenite $Ni_{2-p}Mn_pO_3$
<i>l</i>	Spinel $Ni_{3-x}Mn_xO_4$ and ilmenite $Ni_{2-p}Mn_pO_3$

Table 2.1 Details of the phases present in the regions indicated in the phase diagram of the $NiO - Mn_2O_3 - O_2$ material system

of the material and this process can be expressed by the following equation [18]



Below 730°C nickel manganate undergoes phase change as following



However, it has been shown that this decomposition of nickel manganate at temperatures < 730°C can be prevented by suitable cation substitution, using either magnesium [19], zinc [20], cobalt [21], iron [22, 23] or lithium [23, 24]. Such substitution results in changes in the electrical properties of the material as well.

2.4 SYNTHESIS ROUTES

Nickel manganate has been produced using various methods and precursors. The most common way to synthesise nickel manganate has been by the conventional powder processing technique using oxide precursors (*NiO* and *Mn₂O₃*) [8, 25, 26]. This process was followed in this study and will be discussed in greater detail in chapter 4. Kamiyama et. al. [27] used *NiO* and *Mn₂O* to produce nickel manganate by sintering at 1300°C. Nickel manganate has also been produced from carbonates of nickel and manganese by Baliga et. al. [28] by calcining at 1000°C and annealing at 850°C. Gorgeu et. al. [27] synthesised nickel manganate from sulphates of nickel and manganese.

Nickel manganate can also be produced via wet chemical routes, which generally tend to be non-trivial due to the number of complex steps involved in the process. Two methods have been used for producing nickel manganate using wet chemical routes. Co-precipitation of hydroxides of nickel and manganese is one route, although there are

often problems with residual sodium from the sodium hydroxide used in the technique [29]. The other well established technique is that of co-precipitation of nickel and manganese oxalates [16, 30].

The wet chemical routes form nickel manganate at a much lower temperature than in the conventional powder processing techniques, where the sintering is typically carried out above 1100°C. In the wet chemical processing, the particle size of the precipitates tends to be much smaller than that obtained from the powder processing techniques, and hence the reaction can be achieved at a much lower temperature. However as mentioned earlier due to the complexity of the processing and due to the large amounts of chemical waste generated, these techniques are commercially less attractive.

2.5 CONDUCTION MODELS

The conduction in $Ni_xMn_{3-x}O_{4+\delta}$ is believed to be based on an 'electron hopping mechanism', where on thermal activation electrons hop between Mn^{3+} and Mn^{4+} ions present in the octahedral sites [7] of the crystal structure. The mechanism can be represented by



Macklen [7] suggested that electrons can only hop between cations of the same metal and the difference in the valence state needs to be 1. Hence electrons cannot hop from a Ni^{2+} to a Mn^{3+} or between Mn^{2+} and Mn^{4+} . He also proposed that cations in the tetrahedral sites do not take part in the conduction process as the sites are too far away from each other and the occupancy is low. This suggests that the conductivity of the material is strongly dependent on the ratio of the trivalent and tetravalent manganese

ions in the octahedral sites and that maximum conductivity would occur when the ratio is 1. This explains the significance of the charge distribution in the crystal structure discussed in section 2.2. The inversion parameter ν determines the ratio of the manganese ions in the different lattice sites and according to equation 2.4, the ratio of Mn^{3+} to Mn^{4+} is 1 when ν is 0.667. Hence any deviation of ν from 0.667 would suggest that the conductivity of the material would decrease. However the ratio of the cations would also change with a change in the oxygen stoichiometry of the material as discussed in section 2.2.

2.5.1 NNH MODEL

In nickel manganate the hopping takes place between localised electron states near the Fermi level. The rate of hopping from one localised state i to another j depends both on the physical separation r_{ij} and the difference in the energy ε_{ij} between the two states. For single electron hops the resistivity can be expressed as [31]

$$\rho \propto \exp\left(\frac{2r_{ij}}{a} + \frac{\varepsilon_{ij}}{k_b T}\right) \quad (2.11)$$

where a is the radius of the localised state and k_b is the Boltzmann constant. When the temperature is high the first term in the parentheses of equation 2.11 is greater than the second term and charge transfer takes place between two states close to each other. In this case (nearest neighbour) the r_{ij} is constant and the hopping takes place with constant activation energy. The resistivity can be expressed as

$$\rho = \rho_0 \exp\left(\frac{\Delta E}{k_b T}\right) \quad (2.12)$$

where ΔE is the activation energy required for an electron to hop and ρ_0 is a constant and often referred to as the resistivity at infinite temperature. When an electron hops from one site to the next it emits and absorbs phonons. For materials where the conduction is due to nearest neighbour hopping, a straight line can be obtained when the natural log of resistivity is plotted against the inverse of temperature. The activation energy can be found from the slope of the line and the intercept is the value of ρ_0 .

2.5.2 MOTT VRH MODEL

When both the terms in equation 2.11 are comparable, the hopping rate is not determined by the first term and the sites to which electrons hop are not determined by the separation between the two sites but are primarily dependent on the amount of energy required for the transition. Hence an electron may jump to a distant site if the energy required for the transition is sufficiently low. This is referred to as variable range hopping (VRH) and Mott [32] suggested that only the electrons very near to the

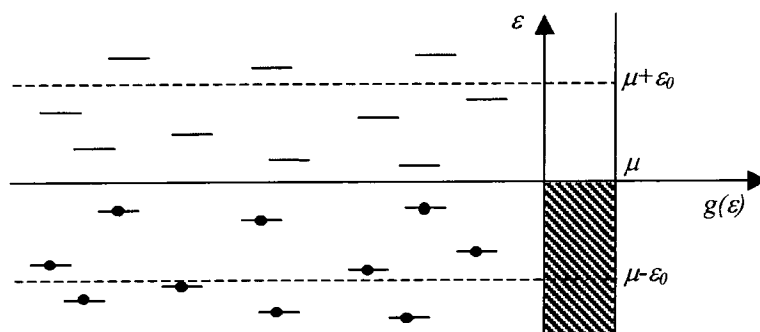


Figure 2.3 The band containing the states whose energies are separated from the Fermi level by less than ϵ_0 . The density of states diagram on the right shows the range of occupied states as the shaded area (reproduced from reference [31])

Fermi level μ actually contribute in such a mechanism as the energies involved are quite low. Figure 2.3 shows the energy range ($\mu + \varepsilon_0$ to $\mu - \varepsilon_0$) of the electrons which take part in such a mode of conduction. The model assumes a constant density of states $g(\mu)$ with energy around the Fermi level. Hence the density of states can be expressed in terms of charge carrier concentration $N(\varepsilon_0)$, which is the concentration of the states which can contribute to the conduction process.

$$N(\varepsilon_0) = 2g(\mu)\varepsilon_0 \quad (2.13)$$

In equation 2.11 the separation between the states r_{ij} can be replaced with the density of charge carriers $[N(\varepsilon_0)]^{-1/3}$. For a constant density of states the average energy separation of the electrons is taken to be ε_0 and (2.11) can be rewritten as

$$\rho = \rho_0 \exp \left[\frac{1}{N^{1/3}(\varepsilon_0) a} + \frac{\varepsilon_0}{k_b T} \right] \quad (2.14)$$

Using the relationship in 2.13 the above equation can be rewritten as

$$\rho = \rho_0 \exp \left[\frac{1}{[g(\mu)\varepsilon_0]^{1/3} a} + \frac{\varepsilon_0}{k_b T} \right] \quad (2.15)$$

The above expression gives the resistivity due to hopping between the sites in the energy band shown in figure 2.3. The numerical factors have been ignored in deriving the model. It is clear that at constant temperature when ε_0 increases so does the resistivity as ε_0 is in the numerator of the second term. Conversely, as ε_0 decreases the two terms in the exponent become similar and on further decrease of ε_0 the resistivity actually increases when the first term starts to become dominant. The minimum resistivity occurs when ε_0 has the following value

$$\varepsilon_0 = \varepsilon_0(T) = \frac{(k_b T)^3}{[g(\mu)a^3]^{\frac{1}{4}}} \quad (2.16)$$

The energy ε_0 changes with temperature and hence this is a process with changing activation energy. Substituting 2.16 in the expression 2.15, the resistivity can be written as

$$\rho = \rho_0 \exp\left(\frac{T_0}{T}\right)^{\frac{1}{4}} \quad (2.17)$$

where the characteristic temperature T_0 is given by

$$T_0 = \frac{1}{g(\mu)k_b a^3} \quad (2.18)$$

However Shklovskii and Efros [31], using a percolation method, have shown that the expression for T_0 had a numerical constant term β , which was found to be 21.2 ± 1.2 .

Thus the characteristic temperature T_0 should be written as

$$T_0 = \frac{\beta}{g(\mu)k_b a^3} \quad (2.19)$$

In this type of mechanism the average hopping length changes with temperature as opposed to a constant hopping length in the case of NNH, justifying the name variable range hopping.

2.5.3 SHKLOVSKII AND EFROS VRH MODEL

Shklovskii and Efros suggested that the assumption of a constant density of states around the Fermi level was not a good approximation and a more general expression for $g(\varepsilon)$ measured from the Fermi level was proposed by them [31]

$$g(\varepsilon) = \frac{\alpha \kappa^3 \varepsilon^2}{e^6} \quad (2.20)$$

where α is a numerical factor and κ describes the strength of the Coulomb interaction between the electrons. This differs from the Mott model in that the density of states has a parabolic distribution in energy. The mean interaction energy ε_D at the average distance r_D between electrons was given by

$$\varepsilon_D = \frac{e^2}{\kappa r_D} \quad (2.21)$$

Using the expression of density of states in (2.20) and using the relationship (2.11) and (2.13) an expression for resistivity can be derived [31] which can be expressed as

$$\rho = \rho_0 \exp\left(\frac{T_0}{T}\right)^{\frac{1}{2}} \quad (2.22)$$

where the characteristic temperature T_0 with an added numerical factor β_l ($\beta_l = 2.8$) is

$$T_0 = \frac{\beta_l e^2}{k_b \kappa \alpha} \quad (2.23)$$

It is noteworthy that the temperature dependence of the resistivity in the Shklovskii and Efros model is different from the Mott model.

Mansfield [33] later reported expressions of resistivity for both the variable range hopping models allowing for the temperature dependence of the pre-exponential factor. The Mott model shows a $T^{-1/2}$ dependence and the Shklovskii and Efros model exhibits a T dependence of the pre-exponential factor. Hence the resistivity expression for the two models (expressions (2.17) and (2.22)) can be rewritten as

Mott VRH model

$$\rho = C_0 T^{\frac{1}{2}} \exp\left(\frac{T_0}{T}\right)^{\frac{1}{4}} \quad (2.24)$$

Shklovskii and Efros VRH model

$$\rho = C_0 T \exp\left(\frac{T_0}{T}\right)^{\frac{1}{2}} \quad (2.25)$$

The above expressions clearly indicate that when the Mott VRH model is applicable a plot of $\ln(\rho * T^{-1/2})$ vs $T^{-1/4}$ should produce a straight line where the characteristic temperature T_0 can be determined from the slope of the line. Similarly a plot of $\ln(\rho * T)$ vs $T^{-1/2}$ should produce a straight line when the Shklovskii and Efros model is applicable.

Similarly, in the case of the NNH model the pre-exponential term ρ_0 contains temperature (T), hence a plot of $\ln(\rho_0 * T^{-1})$ vs T^{-1} can be used to describe the NNH model and the resistivity expression can be written as

$$\rho = C_0 T \exp\left(\frac{\Delta E}{k_b T}\right) \quad (2.26)$$

2.5.4 OTHER MODELS

The conduction in nickel manganate has often been described by hopping of small polarons from Mn^{3+} to Mn^{4+} . Small polarons are defects created when an electronic carrier becomes trapped at a given site as a consequence of the displacement of adjacent atoms or ions [34]. Conductivity is defined as

$$\sigma = ne\mu \quad (2.27)$$

The mobility μ as suggested by Tuller et. al. [34] is given by

$$\mu = \frac{P(1-c)e^2va^2 \exp\left(-\frac{\Delta E}{k_b T}\right)}{k_b T} \quad (2.28)$$

where $c = n/N$, where n is the electron concentration and N is the number of sites available per unit volume, a is the lattice parameter, ν is the phonon frequency, ΔE is the activation energy and P is a factor which gives the probability that an electron will transfer to the next site and is taken to be 1. Hence using equation (2.27) conductivity can be written as

$$\sigma = \frac{NPc(1-c)e^2va^2 \exp\left(-\frac{\Delta E}{k_b T}\right)}{k_b T} \quad (2.29)$$

The resistivity can be expressed as

$$\rho = C_0 T \exp\left(\frac{\Delta E}{k_b T}\right) \quad (2.30)$$

where $\Delta E/k_b$ is also expressed as B , the thermistor constant. A plot of $\ln(\rho \cdot T^{-1})$ vs T^{-1} should yield a straight line if this model is applicable. It is important to note that the temperature dependence of resistivity for both this model and the nearest neighbour model described in section 2.5.1 is the same. This makes it difficult to distinguish between the two mechanisms on the basis of resistance-temperature (R - T) measurements.

Several other empirical relations have been used in the literature to fit data from R - T measurements, without a sound theoretical basis for the relations.

Becker et. al. [35] in 1947 proposed a resistivity expression similar to that of the NNH or the small polaron hopping model, however the temperature dependence of the pre-exponential term was different

$$\rho = \rho_0 T^{-4.83} \exp\left(\frac{\Delta E}{k_b T}\right) \quad (2.31)$$

The activation energy ΔE was found to be 178 meV. In 1950, Bossom et. al. [36] fitted the resistivity data to the following expression

$$\rho = \rho_0 T^{-4.83} \exp\left(\frac{\Delta E}{k_b (T + \theta)}\right) \quad (2.32)$$

where θ was taken as 47.8 and the activation energy ΔE was found to be 193 meV.

More recently Feltz et. al. [18] fitted their R - T data to another resistivity expression

$$\rho = \rho_0 \left(\frac{T_1}{T}\right)^{2.91} \exp\left[B\left(\frac{1}{T} - \frac{1}{T_1}\right)\right] \quad (2.33)$$

Although these empirical models provided good fits to the electrical characteristics, they do not shed much light on the underlying processes responsible for the conduction in the material and hence will not be used in this work.

2.6 THIN FILMS OF NICKEL MANGANATE

Thin films of nickel manganate have been produced since the late 1980s, in order to solve some of the problems associated with bulk thermistors such as porosity, poor intergranular contact, their large size, etc. In 1989, Baliga et. al. [37] reported results of a study of $Ni_{0.6}Mn_{2.4}O_4$ thin films ($10\mu\text{m} - 12\mu\text{m}$) produced by rf magnetron sputtering in an ambient containing 0.01% oxygen followed by post deposition annealing at 250°C in an atmosphere with 0.1% oxygen. The films showed good NTCR characteristics with an activation energy of 327 meV, which was very similar to that of the bulk target material. The report also outlined the effect of varying the oxygen content in the sputtering environment on the properties of the films and showed that at higher oxygen content, the microstructure of the films changed significantly. The microstructure of those films was described as 'cauliflower type' by the authors and hence the study was restricted to films produced in very low oxygen contents ($<0.1\%$). The grain size of the films produced in low oxygen containing environments ranged from 200 to 300 nm. Following this the same authors published [28] further results of $Ni-Mn-O$ films deposited in the same way and found that the resistivity of films deposited in a pure argon atmosphere was higher ($\rho_{300K} = 20 \text{ Kohm-cm}$) than that of films deposited at 1% oxygen content ($\rho_{300K} = 0.5 \text{ Kohm-cm}$). The $R-T$ data were fitted to an expression similar to that of Becker et. al. (equation (2.31)) and did not show a good fit to the NNH nor to the polaronic hopping model. However in 1991 the same authors [38] again reported that the $R-T$ characteristics of films of $Ni-Mn-Co-O$ followed the Mott VRH

model in the temperature range of 200 to 300K. Baliga et. al. also attempted to fit the data to the Shklovskii and Efros VRH model which proved to be unsatisfactory.

A few years later Fau et. al. [39] deposited nickel manganate ($Ni_{0.75}Mn_{2.25}O_4$) thin films (30 – 2000 nm) in argon/oxygen mixed ambients on soda lime glass substrates and reported that the films exhibited poor crystallinity when deposited in pure argon or in an ambient containing more than 0.17% oxygen. The films showed a preferred orientation towards the <111> direction when deposited in ambients containing very small amounts of oxygen (0.09 – 0.17%) and the study was thus restricted to those films. The electrical characteristics were fitted to the polaronic hopping model (including the temperature dependence of the pre-exponential factor) and the resistivity was again found to be dependent on the oxygen content in the ambient. The resistivity of the films deposited in pure argon was 5.5 Kohm-cm at ~323 K reducing to 1.8 Kohm-cm for the films deposited in ambients containing 0.17% oxygen. The activation energy changed from 370 meV for films deposited in pure argon to 327 meV for films deposited in 0.17% oxygen containing ambients.

Recently Dannenberg et. al. [40] reported that rf sputtered films of $Ni_{0.48}Mn_{1.56}Co_{0.96}O_4$ did not fit well to either of the two variable range hopping models. Instead the authors claimed that thermopower measurements indicated a polaronic conduction model. They also proposed that as there was a change in the sign of thermopower (Q), the conduction mechanism changed from p -type (+ve value of thermopower Q) to n -type (-ve value of Q). Q was defined by the authors as

$$Q = \frac{k_b}{e} \ln \left(\frac{1}{\beta} \left[\frac{Mn^{3+}}{Mn^{4+}} \right] \right) \quad (2.34)$$

where β is a constant and the other notations have the usual meaning. The transition from p to n -type was observed when the percentage of oxygen in the sputtering ambient was increased above approximately 1%. The change in the sign of Q was explained by a change in the average oxidation state (more Mn^{4+}) of the manganese ions required to maintain charge neutrality, as the oxygen stoichiometry changed. They also reported a drop in the hopping activation energy with increasing oxygen in the sputtering ambient from 372 meV for films sputtered in pure argon to 282 meV for films sputtered in 2.5% oxygen. However the resistivity of the films decreased with increasing oxygen in the sputtering environment which was consistent with the findings of other authors.

Nickel manganate films were also produced by electrophoretic deposition by Lindner et. al. [41]. A very high deposition rate was achieved using this technique and 10 – 100 μm films were achieved, however the microstructure of the films showed a very porous and ‘loose’ structure even after sintering at 1050°C. Long annealing was required after the initial sintering at the same temperature to obtain phase purity although no x-ray or neutron diffraction results were reported. The R - T characteristics were fitted to a NNH / polaronic model and there was some indication that the conductivity varied with thickness, although no systematic trends could be identified. This perhaps was due to the highly porous structure of the films and the resulting variation in density could have contributed to this difference.

In the mid 1990s electron beam evaporation was used to grow nickel manganate films (~30 μm) and promising results were reported by Parlak et. al. [42] Beckham [29] and later by Schmidt et. al. [26]. Although the latter reported that there was loss of metallic stoichiometry due to preferential evaporation of nickel from the source powder. The films showed poor crystallinity in the as-deposited state and hence post deposition

annealing was necessary. Beet annealed the films at 500°C, which is a temperature regime in which nickel manganate does not exist as a single phase. Parlak et. al. annealed the films in different ambients at similar temperatures. A lowering of both the resistivity ($\rho_{\text{annealed}} = 12 \text{ ohm-cm}$, $\rho_{\text{as-deposited}} = 4600 \text{ ohm-cm}$) and the activation energy ($\Delta E_{\text{annealed}} = 344 \text{ meV}$, $\Delta E_{\text{as-deposited}} = 515 \text{ meV}$) was observed after annealing. The electrical characteristics were fitted to the polaronic model. Schmidt et. al. [26] later reported that the conduction of the electron beam evaporated films could be better explained using the Shklovskii and Efros VRH model.

Schmidt et. al. [30] also reported the preparation and properties of screen printed films of nickel manganate. The powder used for producing the paste for the printing process was synthesised by co-precipitation of nickel and manganese oxalates. An additional glass phase had to be added to overcome the problem of porosity. The thickness of the films was $\sim 32 \mu\text{m}$, much higher than the thickness of all the other films reported so far. The electrical characteristics followed the Shklovskii and Efros VRH model with a characteristic temperature of $\sim 2 \times 10^5 \text{ K}$.

2.7 CONCLUSIONS

A summary of the scientific background required as a foundation for the discussion of the results in subsequent chapters has been outlined in this chapter. The importance of the charge distribution in the crystal structure of nickel manganate along with a brief summary of the results obtained by other researchers were presented. The phase diagram of the nickel – manganese – oxide system has been described and will be referred to in later chapters.

A general description of the various conduction models used to explain the charge transport in the material was given. The dependence of resistivity on the temperature was also discussed for the various models and it was noted that the temperature dependence of the NNH model of electrons and the polaronic model, which essentially is a nearest neighbour hopping process, is the same. Other empirical models used in the literature to describe the electrical characteristics in nickel manganate have been presented.

Finally the work of other researchers on thin films of nickel manganate available in the literature was reviewed. It was evident from this review that the charge transport mechanism in nickel manganate is still not fully understood, resulting in different interpretations of results. The prevailing view on the conduction mechanism in this material is that it is due to polaronic hopping between nearest neighbours, although in many cases the characteristics have been shown to deviate from such behaviour.

Experimental results from the current work will be presented and discussed in the next five chapters. Chapter 3 is devoted to a description of the design and construction of the rf magnetron sputtering system developed during the course of this work and to analysis and optimisation of the performance of the system, in terms of the effects of various process parameters on the growth rates.

2.8 REFERENCES

- [1]. Norton, F.H. (1974) *Elements of ceramics*. Addison-Wesley Publishing Company, Reading, Massachusetts.
- [2]. Koller, A. (1994) Structure and properties of ceramics. In *Materials Science Monographs 80* Elsevier, Amsterdam.
- [3]. O'Neill, H.S.C., Navrotsky, A. *Simple spinels: crystallographic parameters, cation radii, lattice energies, and cation distribution*, (1983) *American Mineralogist*, **68**, 181-194.
- [4]. Grimes, R., Anderson, A., Heuer, A. *Predictions of cation distribution in AB_2O_4 spinels from normalised ion energies*, (1989) *Journal of American Chemical Society*, **111**, 2168.
- [5]. Al-Shahrani, A.A. (1993) Preparation and characterisation of ceramic and thin film Zn_2SnO_4 . PhD Thesis in *Physics* University of Durham, Durham.
- [6]. Hashemi, T., Brinkman, A.W. *X-ray photoelectron spectroscopy of nickel manganese oxide thermistors*, (1992) *Journal of the Materials Research Society*, **7**, 1278-1282.
- [7]. Macklen, E.D. (1979) *Thermistors*. Electrochemical Publications, Glasgow.
- [8]. Sinha, A.P.B., Sinjana, N.R., Biswas, A.B. *On the structures of some manganites*, (1957) *Acta Crystallographia*, **10**, 439-440.
- [9]. O'keefe, M. *Cation valencies and distribution in spinel structures containing manganese*, (1961) *Journal of Physics and Chemistry of Solids*, **21**, 172-178.
- [10]. Larson, E.G., Arnott, R.J., Wickham, D.G. *Preparation, semiconduction and low-temperature magnetization of the system $Ni_{1-x}Mn_{2+x}O_4$* , (1962) *Journal of Physics and Chemistry of Solids*, **23**, 1771-1781.
- [11]. Boucher, B.P., Buhl, R., Perrin, M. *Etude cristallographique du manganite spinelle cubique $NiMn_2O_4$ par diffraction de neutron*, (1969) *Acta Cryst*, **B25**, 2326-2333.
- [12]. Brabers, V.A.M., Van Setten, F.M., Knapen, P.S.A. *X-ray photoelectron spectroscopy study of the cation valencies in nickel manganite*, (1983) *Journal of Solid State Chemistry*, **49**, 93-98.
- [13]. Asbrink, S., Waskowska, A., Drozd, M., Talik, E. *Physical properties and X-ray diffraction of $NiMn_2O_4$ single crystal below and above the ferrimagnetic transition at $T_c=145$* , (1996) *Journal of Physics and Chemistry of Solids*, **58**, 725-729.

- [14]. Macklen, E.D. *Electrical conductivity and cation distribution in nickel manganite*, (1986) *Journal of Physics and Chemistry of Solids*, **47**, 1073-1079.
- [15]. Feltz, A., Topfer, J. *Bildung von Defektspinellen und Phasenbeziehungen im System $Ni_xMn_{3-x}O_4$* , (1989) *Zeitschrift fuer anorganische und allgemeine Chemie*, **576**, 71-80.
- [16]. Wickham, D.G. *Solid-phase equilibria in the system $NiO-Mn_2O_3-O_2$* , (1964) *Journal of Inorganic Nuclear Chemistry*, **26**, 1369-1377.
- [17]. Brieu, M., Couderc, J.J., Rousset, A., Legros, R. *TEM Characterization of nickel and nickel-cobalt manganite ceramics*, (1993) *Journal of the European Ceramic Society*, **11**, 171-177.
- [18]. Feltz, A., Topfer, J., Schirrmeister, F. *Conductivity data and preparation routes for $NiMn_2O_4$ thermistor ceramics*, (1992) *Journal of the European Ceramic Society*, **9**, 187-191.
- [19]. Feltz, A., Neidnicht, B. *Investigation on electronically conducting oxide systems XX. $MgNiMnO_4$ and properties of $Mg_xNiMn_{2-x}O_4$ spinels*, (1991).
- [20]. Guillemet-Fritsch, S., Baudour, J.L., Chanel, C., Bouree, F., Rousset, A. *X-ray and neutron diffraction studies on nickel zinc manganite $Mn_{2.35-x}Ni_{0.65}Zn_xO_4$* , (2000) *Solid State Ionics*, **132**, 63-69.
- [21]. de Vidales, J.L.M., Garcia-Chain, P., Rojas, R.M., Vila, E., Garcia-Martinez, O. *Preparation and characterization of spinel-type Mn-Ni-Co-O negative temperature coefficient ceramic thermistors*, (1998) *Journal of Materials Science*, **33**, 1491-1496.
- [22]. Brabers, V.A.M. *Cation migration cation valencies and the cubic - tetragonal transition in $Mn_xFe_{3-x}O_4$* , (1971) *Journal of Physics and Chemistry of Solids*, **32**, 2181-2191.
- [23]. Sarrion, M.L.M., Marales, M. *Preparation and characterisation of NTC thermistors : nickel manganite doped with lithium*, (1995) *Journal of the American Ceramic Society*, **78**, 915-921.
- [24]. Topfer, J., Feltz, A., Graf, D., Hackl, B., Raupach, L., Weissbrodt, P. *Cation valencies and distribution in the spinels $NiMn_2O_4$ and $M_zNiMn_{2-z}O_4$ ($M = Li, Cu$) studied by XPS*, (1992).
- [25]. Parlak, M. (1998) Negative temperature coefficient (NTC) thermistor pellets and thin film studies, Internal Report, University of Durham, Department of Physics, Durham.

- [26]. Schmidt, R., Brinkman, A.W. *Preparation and characterisation of NiMn₂O₄ films*, (2001) International Journal of Inorganic Materials, **3**, 1215.
- [27]. In Schmidt, R. (1999) Thin film NTC thermistors., Internal Report, University of Durham, Department of Physics, Durham.
- [28]. Baliga, S., Jain, A.L., Zachofsky, W. *Sputter deposition and characterisation of Ni-Mn-O and Ni-Co-Mn-O spinels on polyamide and glass substrates*, (1990) Applied Physics A : Solids and Surfaces, **50**, 472-477.
- [29]. Beckham, M (1998) Thick film NTC thermistor structures, MSci Final Year Project Report in *Physics* University of Durham, Durham.
- [30]. Schmidt, R., Stiegelschmitt, A., Roosen, A., Brinkman, A.W. *Preparation and Performance of Thick Film NTC Thermistors*, (2002) Key Engineering Materials, **206-213**, 1417-1420.
- [31]. Shklovskii, B.I., Efros, A.L. (1984) *Electronic properties of doped semiconductors*. Springer - Verlag, Berlin.
- [32]. Mott, N.F., Davis, E.A. (1979) *Electronic Processes in Non-crystalline Materials*. Clarendon Press, Oxford.
- [33]. Mansfield, R. Hopping conduction in III-V compounds. In *Hopping transport in Solids* (M. Pollak and B. Shklovskii, eds), Elsevier Science, Amsterdam (1991).
- [34]. Tuller, H.L., Nowick, A.S. *Small polaron electron transport in reduced CeO₂ single crystals*, (1977) Journal of Physics and Chemistry of Solids, **38**, 859-867.
- [35]. Becker, J.A., Green, C.B., Pearson, G.L. *Properties and use of thermistors- Thermally sensitive resistors* (1947) Bell Systems Technical Journal, **26**, 170.
- [36]. Bossom, G., Gutman, F., Simmons, L.M. (1950) Journal of Applied Physics, **21**, 1267.
- [37]. Baliga, S., Jain, A.L. *Deposition and properties of rf magnetron sputtered Ni_{0.6}Mn_{2.4}O₄*, (1989) Materials Letters, **8**, 175-178.
- [38]. Baliga, S., Jain, A.L. *Hopping conduction in sputtered Ni-Co-Mn-O spinel films*, (1991) Materials Letters, **11**, 226-228.
- [39]. Fau, P., Bonino, J.P., Demai, J.J., Rousset, A. *Thin films of nickel manganese oxide for NTC thermistor applications*, (1993) Applied Surface Science, **65/66**, 319-324.
- [40]. Dannenberg, R., Baliga, S., Gambino, R.J., King, A.H., Doctor, A.P. *Resistivity thermopower and the correlation to infrared active vibrations of*

- Mn_{1.56}Co_{0.96}Ni_{0.48}O₄ spinel films sputtered in an oxygen partial pressure series,* (1999) *Journal of Applied Physics*, **86**, 514-523.
- [41]. Lindner, F., Feltz, A. *Thin layer NTC semiconductor ceramics based on NiMn₂O₄ and Zn_zNiMn_{2-z} (z = 1/3, 2/3),* (1993) *Journal of the European Ceramic Society*, **11**, 269-274.
- [42]. Parlak, M., Hashemi, T., Hogan, M.J., Brinkman, A.W. *Effect of heat treatment on nickel manganite thin film thermistors deposited by electron beam evaporation,* (1999) *Thin Solid Films*, **345**, 307-311.

Construction and Calibration of the RF Magnetron Sputtering System

3.1 INTRODUCTION

This is the first of five chapters where results from the experimental work carried out in the project are presented and discussed. The present chapter focuses on the design and construction of the rf magnetron system which was used in this project to deposit thin films of nickel manganate. The first half of the chapter is primarily devoted to a description of the sputtering system and it is worth mentioning here that the design and construction took a significant amount of time for completion. Many of the results presented in the later chapters were entirely dependent on the successful construction of the sputtering system. The effect of the various process parameters on the deposition rate of the system will be discussed, together with the results of a factorial design experiment. Factorial design experimentation is a statistical method by which effects of multiple process parameters on properties of an end product of a process can be studied simultaneously. This study was aimed at providing a starting point for the fabrication of reproducible thin films for structural and electrical characterisation.

3.2 THEORETICAL BACKGROUND

3.2.1 SPUTTERING

The phenomenon of sputtering was discovered more than 150 years ago in a gas discharge tube by Grove [1]. Since then the technique has been greatly developed and is now used for a variety of applications. Sputtering may be defined as the ejection of particles from a material when it is bombarded with high energy ions. When a large voltage is applied across a pair of electrodes in a low-pressure gas, the gas is ionised and a glow discharge or plasma is created [2]. The ions in the plasma are very energetic and being positively charged are attracted towards the cathode and on striking cause the ejection or sputtering of cathode material. Argon is the gas most commonly used for sputtering, as it provides comparatively large ions for sputtering and it being inert avoids any chemical reaction with the target [3]. The sputtering yield depends mainly on the energy transfer from the incident particles to the cathode material, angle of incidence and also on whether the impinging particle is ionised or not [4]. One of the main advantages of the process is that sputtering is not strongly dependent on the cathode or the target temperature. This makes the process suitable for a very wide range of materials.

3.2.2 MAGNETRON SPUTTERING

Planar magnetrons, which are the most common, were first introduced in the 1970s [5] to increase deposition rates and reduce substrate heating by confining the plasma to the target. The important aspects of magnetron sputtering are shown in figure 3.1 [6]. The cathode, commonly in the shape of a circular disc, is located above an arrangement of permanent magnets inside, which provides a field that confines the electrons above and close to the target. The cathode is connected to a power supply and the glow discharge is ignited. The region becomes densely populated with electrons from the ionised gas

which under the influence of the Lorentz force from the magnets and the negative cathode potential travel along helical paths [4] to the outer perimeter of the target where they are collected by a grounded anode preventing them from reaching the substrate. The configuration ensures a long path length for the electrons and as a result a

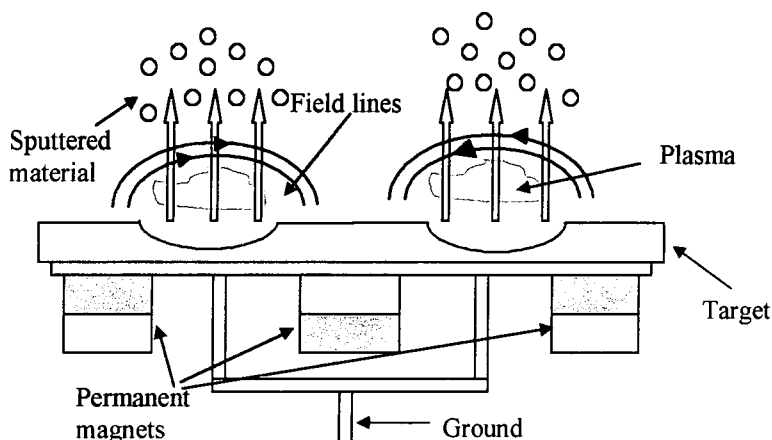


Figure 3.1 A schematic illustration of a magnetron cathode showing the basic principles of operation (reproduced from reference [6])

high plasma density over the cathode with a correspondingly high number of positively charged ions, leading in turn to a high deposition rate.

3.2.3 RF SPUTTERING

DC sputtering cannot be used with insulators, as charge build-up at the cathode surface rapidly extinguishes the plasma and stops the sputtering process [7]. In such cases rf sputtering must be used. In a rf discharge the electrons oscillate in the changing field thus gaining energy creating ions and more electrons by impact ionisation. The insulating target is placed on the cathode, which has a metal backing plate. The plasma, the target and the metal plate act as capacitors with the potential at the surface of the target alternating between positive and negative. During the negative half cycle the

positive ions bombard the surface of the target causing sputtering of the target. As the substrate holder, chamber walls, etc. are all grounded they effectively act as an anode of much greater area [8]. Since the capacitive reactance is inversely proportional to the area a greater proportion of the potential will be dropped across the smaller cathode ensuring a higher field near the cathode and preventing ion bombardment of the substrate during the positive half cycle. The rf power supply operates at 13.56 MHz with peak-to-peak voltages above 1KV. To ensure maximum transfer of power to the plasma, it is generally necessary to include an impedance matching unit between the rf power supply and the cathode. Impedance matching generally consists of a number of variable reactive components, which must be adjusted to minimise the reflected power [9].

3.2.4 REACTIVE SPUTTERING

Reactive sputtering has been successfully used to produce a number of different films. In this process at least a fraction of one or more of the film's constituents is introduced into the deposition chamber in the vapour phase. There are applications where one of the components is entirely derived from the gaseous phase e.g. nitrogen is introduced as a gas for depositing aluminium nitride films [10] and oxygen has been used to produce films of RuO_2 [11]. The chemical reaction may take place at the target surface, in the gaseous phase or at the substrate although gas phase reactions take place only when the gas pressure is very high. Baliga et. al. [12] have successfully used a mixture of oxygen and argon for depositing films of nickel manganese cobalt oxides although the percentage of oxygen used in the deposition was very low.

In this project a rf magnetron system capable of reactive sputtering was designed which will be discussed in the following section.

3.3 DESCRIPTION OF THE SPUTTERING SYSTEM

The principal aim was to build a sputtering system, which would be able to produce thin films of nickel manganate from a ceramic target with properties similar to those of the target. As discussed in the previous section, it was necessary to use rf power as the target was not a good electrical conductor at room temperature. To achieve properties similar to that of the bulk material, it was essential to control and monitor certain process parameters, such as the oxygen content in the sputtering environment. All these factors were taken into consideration while designing the system and will be described in the following sections.

An existing cylindrical stainless steel chamber, internal diameter 305 mm and depth 125 mm, was adapted for use as the main deposition chamber, as illustrated in figure 3.2.

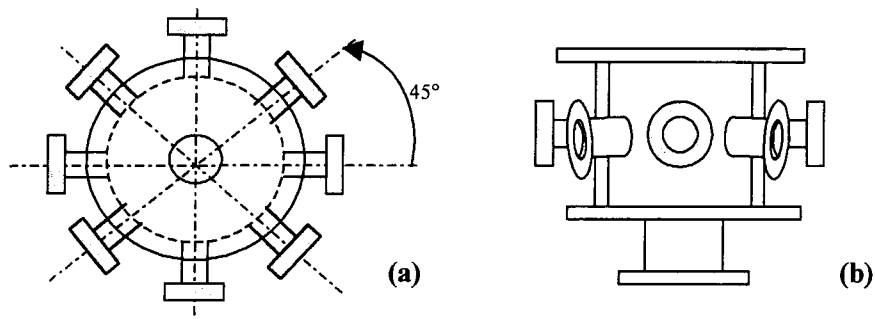


Figure 3.2 Schematic representation of the stainless steel chamber used as the sputtering chamber (a) plan view and (b) side view

The chamber was not high enough to accommodate a vertical sputtering arrangement where the cathode was to be attached to one of the radial ports. Thus, a 121 mm high collar was added in between the chamber and the top plate to increase the overall height of the chamber and to make it suitable for vertical sputtering. The chamber was mounted on a specially designed frame (figure 3.3) with a mechanism to lift the top plate of the deposition chamber for removal of deposited films and reloading of

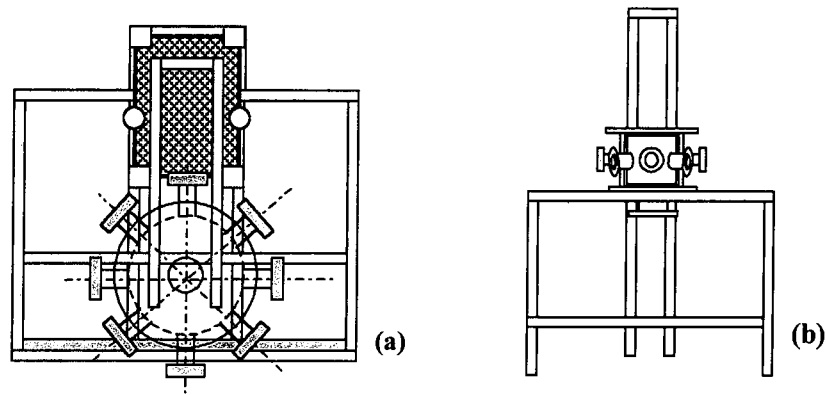


Figure 3.3 Schematic representation of the frame, the position of the deposition chamber and the mechanism for lifting the top plate in (a) plan view and (b) front view

substrates. The functional parts of the sputtering system can be essentially divided into four groups, which are as follows:

1. vacuum system
2. target and substrate handling system
3. gas handling system
4. temperature control

3.3.1 VACUUM SYSTEM

The system was evacuated using a combined Edwards E2M5 rotary backed turbomolecular (Leybold 361) pump, which could pump the system to a base pressure of $\sim 8 \times 10^{-7}$ mbar. The turbo pump was fitted to the bottom of the chamber and connected to the rotary pump by flexible pipes. The latter was placed on a rubber mat to minimise the transmission of vibration from the rotary pump to the turbo pump. The pressure of the system was monitored using both pirani and penning gauges controlled by a Leybold Combivac CM31 controller. The system took approximately 12 hours to pump down to the base pressure level. The sputtering was carried out at Ar/O_2 pressures

of around 5×10^{-2} mbar with the turbo pump switched off. The chamber was continuously pumped during sputtering using the rotary pump and the second pirani gauge placed at the bottom of the chamber was used to monitor the pressure.

3.3.2 TARGET AND SUBSTRATE HANDLING SYSTEM

An on-axis sputtering [13] configuration with the target placed directly beneath the substrates was used as illustrated in figure 3.4. The target was prepared following a conventional powder processing technique using oxide precursors and will be discussed in detail in chapter 4. The target was attached to a 33 mm diameter MiniMak rf

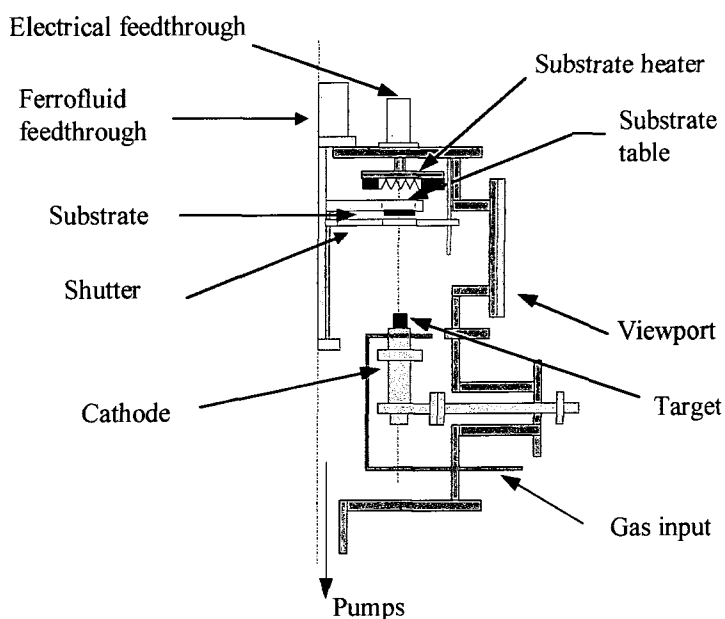


Figure 3.4 A schematic representation of the sputtering configuration used in the project showing the important features

magnetron cathode by conductive silver paste. A water chiller unit was used to provide continuous cooling water (3°C) required by the cathode during sputtering. A Pearl Kogyo RP500C rf power supply and automatic impedance matching circuitry was used to provide the necessary power.

Substrates were placed on a round table designed to hold up to eight square substrates (maximum 24 x 24 mm) as shown in figure 3.5 (a). The substrate table was made out of copper because of its good electrical and thermal conductivity to which the substrates,

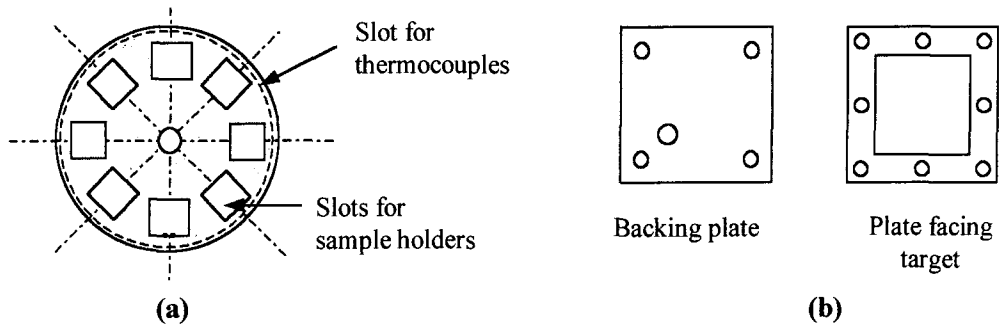


Figure 3.5 Schematic diagram of (a) the substrate holding table and (b) a substrate holder

individually mounted on copper substrate holders (figure 3.5 (b)), were attached. The backing plate of the holder was designed to ensure uniform heating of the substrates. The extra hole in the backing plate was made to allow the thermocouple tip, used for monitoring the temperature, to touch the substrate. The substrate table was suspended

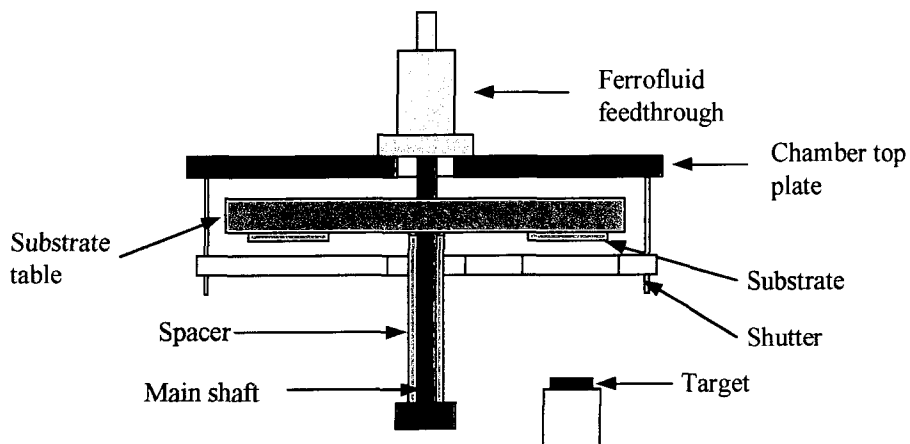


Figure 3.6 Schematic arrangement inside the sputtering chamber showing the substrate table, shutter and other details

on a stainless steel shaft connected to a ferrofluid feedthrough fitted on the top plate of the chamber, which allowed the table to be rotated. The distance from the table to the

cathode could be altered by changing the length of the spacers fitted between the base of the shaft and the table. This allowed positioning of the table anywhere along the shaft in a simple way. A shutter was placed in between the substrate table and the target and was fixed using screws attached to the top plate of the chamber so that deposition took place on only one substrate at a time.

3.3.3 GAS HANDLING SYSTEM

One of the important parameters of the sputtering process was the oxygen content in the ambient. A varying mixture of argon and oxygen had to be introduced during sputtering in order to adjust the oxygen stoichiometry of the deposited films. It was essential that the composition of the sputtering gas could be controlled accurately throughout the sputtering process. A system was designed where the argon and the oxygen first passed through mass flow controllers and then through a tube filled with glass balls which ensured a good mixing of the gases. Valves were located before each mass flow controller in the pipe-work to ensure that supply could be cut off at any time. The mass flow controllers were individually calibrated for the particular gas handled and were operated using a custom built controller with a digital display of the flow rate. An Anacon Model 78 oxygen sensor was placed in-line to monitor the percentage of oxygen in the gas mix. The gas was then passed through an on/off and a needle valve, which controlled the volume of gas admitted to the chamber and thus the pressure during sputtering. The arrangement is illustrated in figure 3.7. The oxygen sensor was calibrated using oxygen free nitrogen and air. The gas was introduced into the system through a stainless steel pipe made into a ring, which surrounded the cathode. The end of the pipe was sealed and small holes were drilled in the section around the cathode. The arrangement is shown in figure 3.8 and ensured an uniform distribution of the

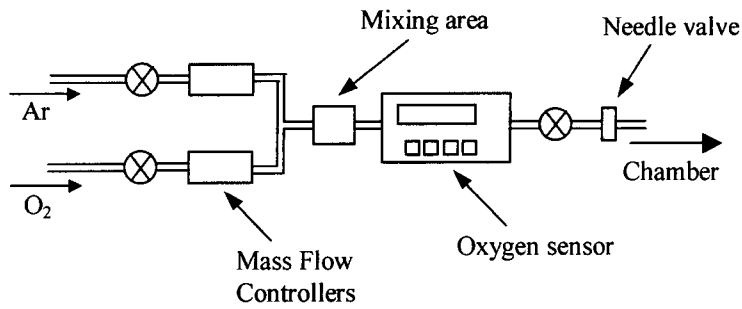


Figure 3.7 Schematic arrangement of the gas handling system used for mixing argon and oxygen

sputtering gas around the cathode. This configuration had been used by Hong et. al. [14] who reported an improvement in the thickness distribution in films when the

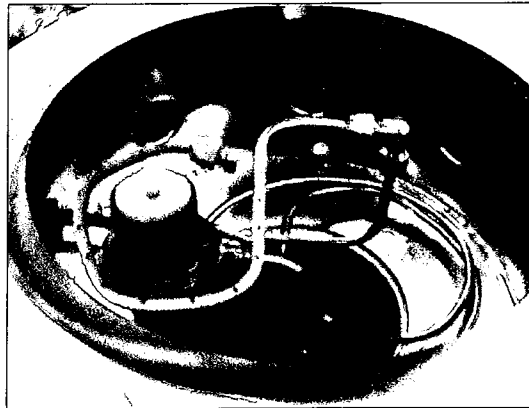


Figure 3.8 Photograph illustrating the gas ring around the cathode used in the system along the target

distance between the cathode and the gas ring was increased. However in this work the position of the ring was kept constant at about 10 mm above the target.

3.3.4 TEMPERATURE CONTROL

Provision was made to monitor and control the temperature of the substrate during sputtering. A conventional tungsten filament heater assembly (figure 3.9 (a)) was designed and fitted on the top plate above the sputtering position, i.e. directly above the

target as shown in figure 3.9 (b). All eight thermocouples (one per substrate) were connected via a vacuum feedthrough to a switch box, which was used to connect the relevant thermocouple to the controller. A 5 mm thick copper block was placed on the backing plate of the substrate holder, which acted as a temperature stabilising block and ensured an even distribution of heat over the backing plate of the substrate holder. A polished steel plate was placed above the heater assembly as a heat reflector. The

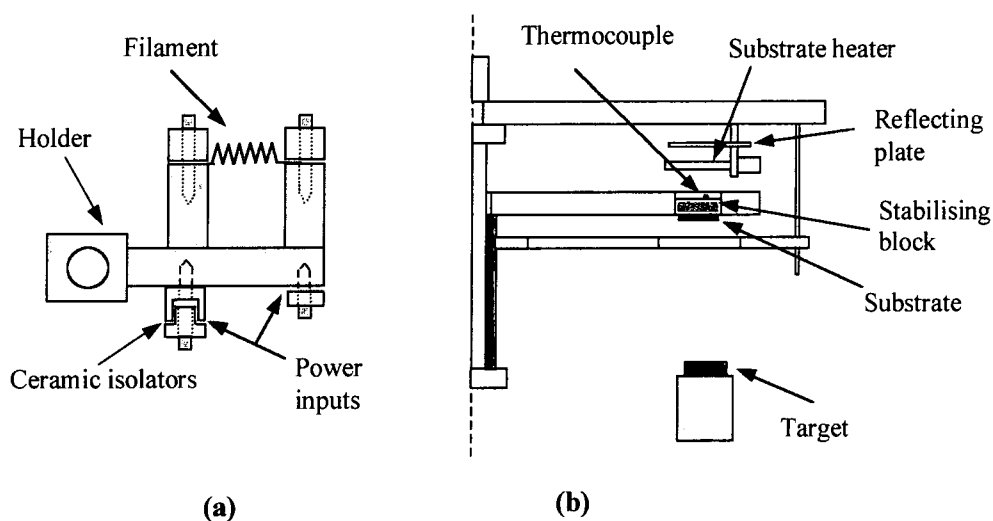


Figure 3.9 Schematic diagram of (a) the substrate heater arrangement and (b) the position of the substrate heater

temperature was monitored and controlled using an Eurotherm 810 temperature controller via a thyristor pack and a high current transformer (90 amps and 10 volts output). Substrates were heated prior to the deposition and adequate time was allowed for the temperature to stabilise before commencing sputtering.

The system specification can be summarised as follows :

- (a) The system could be pumped down to a base pressure of $\sim 10^{-7}$ mbar
- (b) Eight films could be deposited in one vacuum cycle

- (c) The distance between the substrate table and the target could be altered in the range of 20 – 50 mm
- (d) The sputtering gas composition (argon / oxygen) could be controlled down to 0.3% oxygen
- (e) Substrates could be heated upto 250°C and the temperature could be monitored during the entire growth

Figures 3.10 (a) and (b) show pictures of the system.

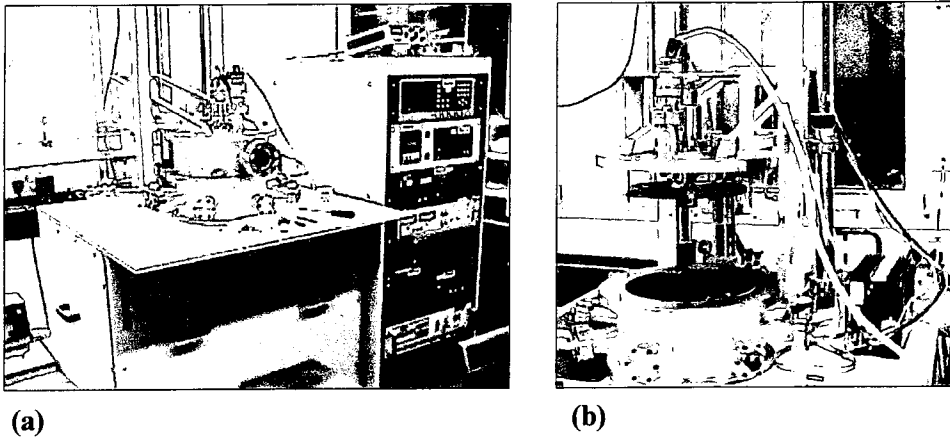


Figure 3.10 Pictures of the sputtering system (a) illustrating the controller unit and (b) with the top plate lifted

3.4 CALIBRATION OF THE SPUTTERING SYSTEM

The effects of a number of process parameters on the deposition rate have been studied. All the films were deposited on <100> silicon substrates and the thickness was measured using an Alpha step 200 (Tencor Instruments) profilometer. In this section each of the following process parameters have been studied individually while the others were kept constant. The error bars represents the spread of the data based on three

(unless stated otherwise) different measurements, where the data point represents the mean value.

1. Time
2. Distance between the substrate and the target
3. Oxygen content in the ambient
4. Substrate temperature
5. Pressure
6. Power

3.4.1 EFFECT OF TIME

In order to produce films of different thickness it was essential to know whether the deposition rate varied with time. The films were deposited using the following conditions:

Power	25 watts
Pressure	$\sim 5 \times 10^{-2}$ mbar
Gas composition	Pure argon
Target to substrate distance	50 mm

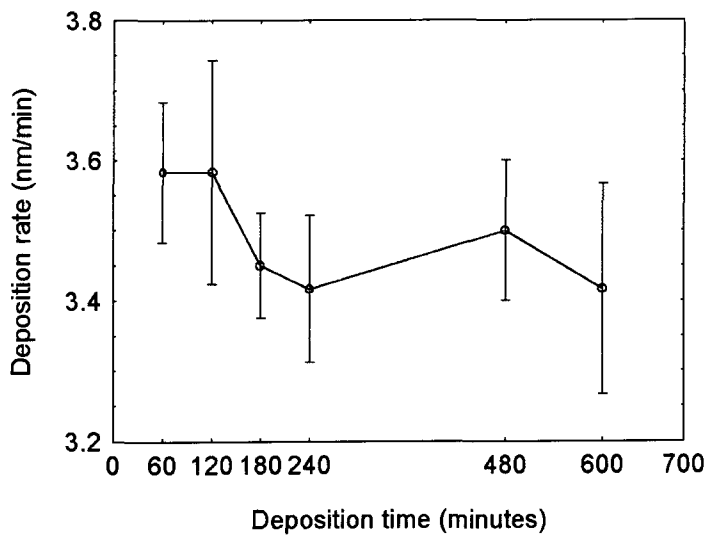


Figure 3.11 Plot showing the variation of the deposition rate as a function of deposition time

The results are shown in figure 3.11 and they indicated that at the above conditions, the deposition rate did not change significantly as a function of time. However, the films deposited for 60 and 120 minutes had a marginally higher deposition rate of ~ 3.6 nm/min, compared to the ones deposited for a longer time, which had a deposition rate of ~ 3.4 nm/min.

3.4.2 EFFECT OF SUBSTRATE TO TARGET DISTANCE

The films were deposited using similar conditions to those described in the previous section, but the distance between the target and the substrate was varied. The results can be seen in figure 3.12. The deposition rate increased as the substrate was brought closer

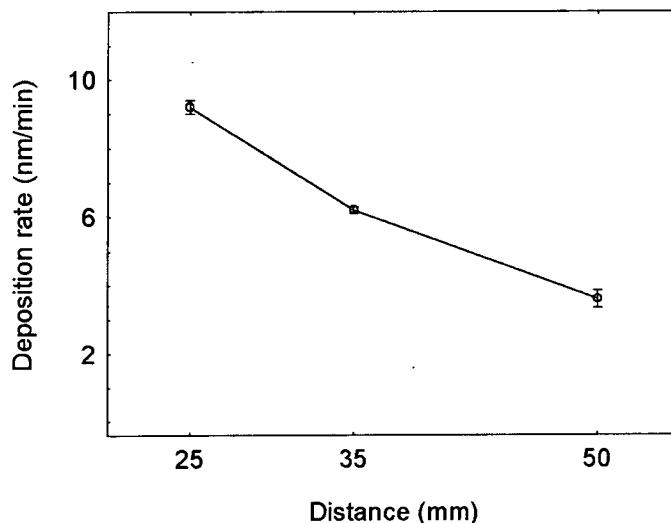


Figure 3.12 Plot showing the variation of the deposition rate with increasing distance between the target and the substrate

to the target. Jaing et. al. [15] had pointed out that the emission from the sputtering of the target should follow a cosine law, from which can be inferred that there would be some particles emitted at low angles that would not reach the substrate. The effect increases as the substrate is placed further away from the target. Additionally some of the sputtered atoms will be deflected as a result of collision with gas atoms. Hence the

deposition rate was expected to decrease as the distance between the target and substrate increased.

3.4.3 EFFECT OF OXYGEN CONTENT IN THE AMBIENT

The effect of the oxygen content in the sputtering ambient on the deposition rate was investigated using the same conditions as described in section 3.4.1 apart from the distance between the substrate and the target which was reduced to 25mm. The results are shown in figure 3.13. It was evident that the deposition rate decreased as the oxygen content in the environment increased. The deposition rate decreased almost by a factor of three for films deposited in a high oxygen content (15%) compared to the ones deposited in a lower oxygen containing environment (0.3%). Such behaviour has been

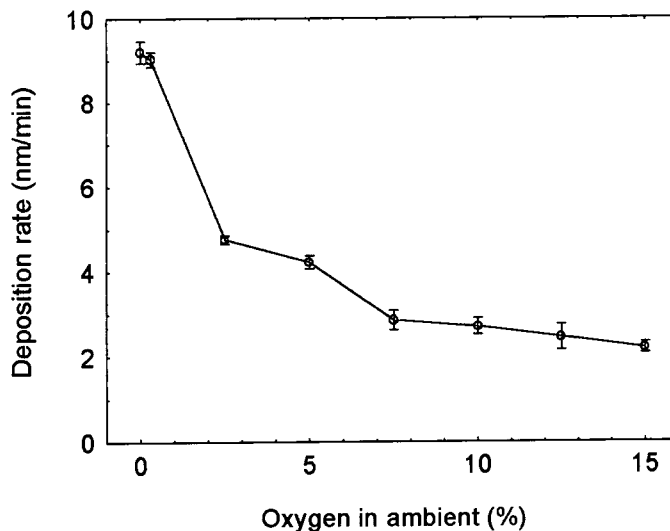


Figure 3.13 Plot showing the variation of the deposition rate as a function of oxygen content in the sputtering environment (data based on two measurements, where the data point represents the mean value)

commonly observed by other researchers who also reported a fall in the deposition rate with increasing amounts of oxygen in the sputtering gas. A model for this has been suggested by Jones et. al. [16] for SiO_2 films produced by rf sputtering in which they assumed that the Si and O_2 atoms were sputtered as alternate layers. The oxygen layer

after sputtering was immediately replaced by the oxygen present in the ambient. However this would suggest that the process cannot proceed once the oxygen content in the ambient reached above a certain level. But in reality, Jones et. al. suggested that this effect actually saturates above a certain partial pressure of oxygen and the deposition rate remains constant thereafter. Similar behaviour was observed for films deposited in this work as well. There was a considerable drop in the deposition rate between the films deposited in 1% and 5% oxygen. But the rate remained very similar for the films deposited with 12.5% and 15% oxygen in the environment. It is also well known that the deposition rates of the metals are much higher than the corresponding oxides and it has been reported [17, 18] that when reactive sputtering is carried out with metallic targets in oxygen containing environments, the sputtering rate drops due to oxide formation on the surface.

3.4.4 EFFECT OF SUBSTRATE TEMPERATURE

The films were also deposited with similar deposition conditions to those described in section 3.4.1 but at different substrate temperatures. Figure 3.14 shows the results,

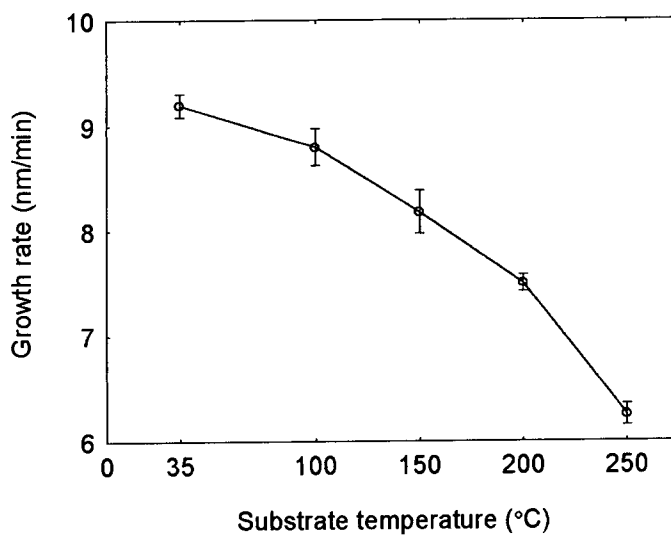


Figure 3.14 Plot showing the variation of the deposition rate with increasing substrate temperature

which indicated a decrease in the deposition rate as the substrate temperature increased. Other researchers sputtering SiO_2 [19], gallium arsenide [20] and germanium [21] also observed this type of dependence of the growth rate on substrate temperatures due to increased thermal energies. It is believed to be the result of greater re-evaporation of incident species at high substrate temperatures. However, Krikorian et. al. [17] found when using dc reactive sputtering for Al_2O_3 , that the trend was reversed and the deposition rate actually increased at higher temperatures. This was thought to be due to the fact that the rate of reaction of the oxygen atoms with the aluminium atoms to form Al_2O_3 increased with increasing substrate temperature.

3.4.5 EFFECT OF PRESSURE

The effect of pressure during sputtering was studied in the range of 5×10^{-1} mbar down to 5×10^{-2} mbar. The other growth conditions were similar to those listed in section 3.4.1. The results are shown in figure 3.15 and indicated that the deposition rate was largely independent of the pressure in the chamber. Generally, the rate is linearly dependent on the pressure for sputtering up to a critical pressure, as the ion density

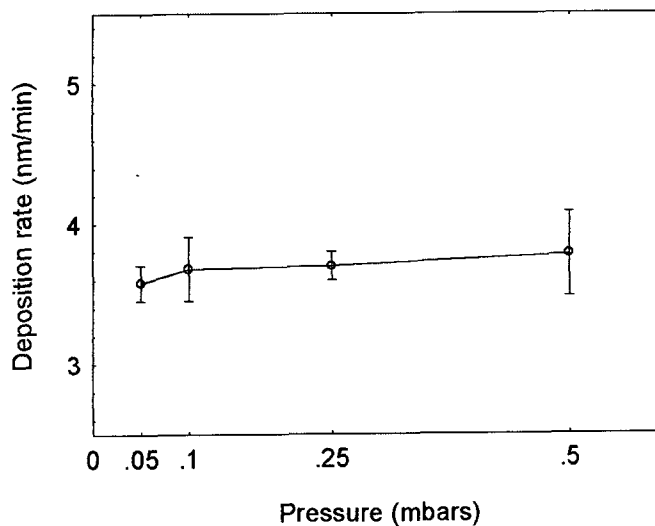


Figure 3.15 Plot showing the variation of the deposition rate with increasing pressure during sputtering

increases. Above a certain pressure, a large percentage of the sputtered species returns to the cathode by back diffusion. For reactive sputtering it was found that the sputtering rate was not highly dependent on the sputtering pressure [17]. Although an increase can be seen in the deposition rate in figure 3.15, the magnitude of the increase is only $\sim 7\%$ between the films deposited at 5×10^{-2} and 5×10^{-1} mbar, an order of magnitude change in the pressure.

3.4.6 EFFECT OF POWER

Varying the incident power resulted in an almost linear increase in the deposition rate with increasing power (figure 3.16). For the films sputtered using 50, 60 and 70 watts power, the time of sputtering had to be shortened to 25, 20 and 15 minutes respectively. Cracks appeared on the target when 60 and 70 watts power was used for more than 30 minutes. This was due to excessive heating of the top half of the target as a result of increased ion bombardment. The bottom of the target remained relatively cold as this was cooled by water. As the target was not a good conductor of heat, a significant temperature gradient developed and hence cracks appeared on the surface and the experiments had to be repeated with new targets.

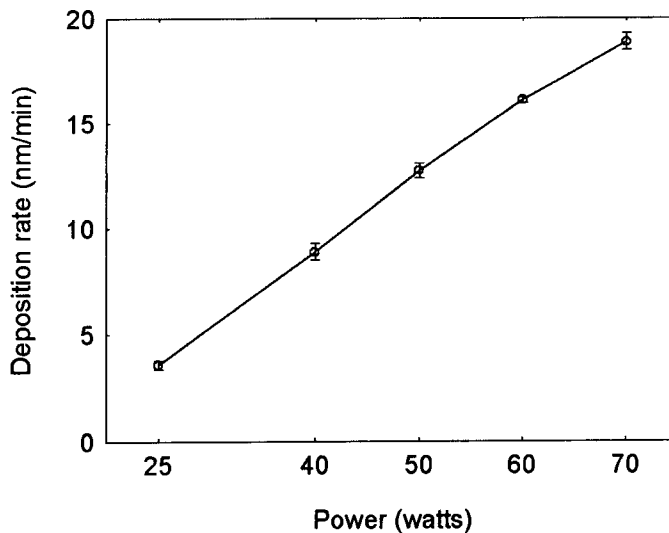


Figure 3.16 Variation of the deposition rate with increasing power used for sputtering (based on two measurements)

The above results showed the dependency of the deposition rate on various process parameters during sputtering. However in this study it was difficult to assess the effect of these parameters when more than one was altered. It appeared that the effects of pressure and time on the deposition rate were not very significant and subsequent study focussed on the four remaining parameters, namely the incident power, substrate to target distance, substrate temperature and the oxygen content in the ambient. To investigate the interaction of these four parameters on the deposition rate a large number of experiments would have been required which was not feasible in the time scale of the project and thus factorial experimental design (FED) technique [22] was employed. This provided a simple and effective way to highlight the important parameters and their interdependencies.

3.5 FACTORIAL EXPERIMENTAL DESIGN TECHNIQUE

Statistical methods have been used to optimise and study the effect of process parameters in a wide range of fields. Researchers have used different experimental design techniques, such as factorial experimental design (FED) and the orthogonal array technique [23, 24] to optimise properties of films produced by rf magnetron sputtering. In this study 16 two level experiments with four factors were carried out. The factors identified in the preliminary studies (section 3.4.1 to 3.4.6) as having the greatest impact on the growth rate were selected for the factorial analysis namely incident power, oxygen content in the environment, substrate to target distance and substrate temperature. The levels of each of the factors were carefully determined, which in case of the distance between the substrate and target and power were the limits of the system. Details of the actual levels of the factors and the design of the experiments are shown in table 3.1 and 3.2 respectively.

Factors	Level 1 (-)	Level 2 (+)
A. Substrate to target distance	25 mm	50 mm
B. Substrate temperature	35°C	200°C
C. Argon / oxygen ratio	1%	10%
D. Incident power	20W	30W

Table 3.1 Details of the levels chosen for each factor for the factorial design experiments

The (-) and the (+) signs are used as codes for the levels (for example *B+* refers to a substrate temperature of 200°C etc.) when describing the various experiments and this convention will be followed for the rest of the chapter.

Experiment number	A	B	C	D
1	-	-	-	-
2	-	-	-	+
3	-	-	+	-
4	-	-	+	+
5	-	+	-	-
6	-	+	-	+
7	-	+	+	-
8	-	+	+	+
9	+	-	-	-
10	+	-	-	+
11	+	-	+	-
12	+	-	+	+
13	+	+	-	-
14	+	+	-	+
15	+	+	+	-
16	+	+	+	+

Table 3.2 The details of all the 16 experiments that were carried out showing the levels of each factor in the experiments

The time of deposition was kept constant at 120 minutes and deposition rate as deduced from the thickness of the film was used as the response. The thickness was measured at four different positions using an Alpha step profilometer and the average was used for the calculation of the rate of deposition. The results of the measurements along with the actual levels of the parameters are shown in table 3.3.

Experiment number	Distance (mm)	Temperature (°C)	Oxygen (%)	Power (watts)	Deposition rate (nm/min)
1	25	35	1	20	5.00
2	25	35	1	30	9.02
3	25	35	10	20	3.13
4	25	35	10	30	5.88
5	25	200	1	20	4.63
6	25	200	1	30	8.07
7	25	200	10	20	7.02
8	25	200	10	30	6.61
9	50	35	1	20	3.84
10	50	35	1	30	6.79
11	50	35	10	20	2.36
12	50	35	10	30	2.72
13	50	200	1	20	3.75
14	50	200	1	30	6.88
15	50	200	10	20	2.73
16	50	200	10	30	3.55

Table 3.3 Details of all the experiments showing the actual levels of the factors and the results obtained

3.5.1 MAIN EFFECTS

The average effect of each individual factor on the growth rate was calculated by computing the difference between the average of the response of all the experiments where the level of the factor was (+) and where the level was (-). So for the factor *A*, the effect can be expressed as [25]

$$ME(A) = \bar{z}(A+) - \bar{z}(A-) \quad (3.1)$$

where \bar{z} is the mean growth rate. The effects for each of the four factors were calculated and are shown graphically in figure 3.17, which is also known as the main effect plot. The lines join the average values of the responses at each level of the factor in question.

It is quite clear from figure 3.17 that the effect of factors A and C on the deposition rate

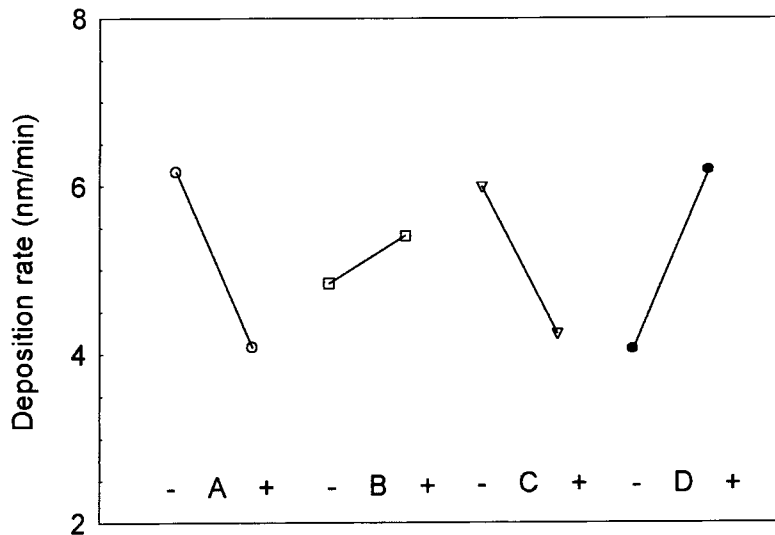


Figure 3.17 The main effects plot showing the individual effect of each of the factors on the growth rate

is the opposite of the factors B and C . Factor A is the distance between the target and the substrate and the deposition rate was higher when the distance was small as seen in section 3.4.2. Interestingly, the growth rate increased as factor B , which was the substrate temperature, increased in contradiction to the results of section 3.4.4 and underlines the need to consider the inter-dependencies of the parameters. However as discussed there, this was possibly due to the presence of oxygen in the ambient, which reacted faster to form the compound on the surface as the temperature increased. It can also be seen from figure 3.17 that the growth rate was relatively little affected by substrate temperature compared to the other factors. The other three factors were almost equally important in their influence on the growth rate. One of the interesting things that

can be done using FED is to determine the combined effects of these factors on the growth rate. These combined effects would be discussed in the next section.

3.5.2 INTERACTION EFFECTS

Interaction effects are a measure of joint effects between two or more factors. The interaction effect of two factors (e.g. A and B) can be described as the equivalent expression

$$INT(A, B) = \frac{1}{2} \{ \bar{z}(B+ | A+) - \bar{z}(B- | A+) \} - \frac{1}{2} \{ \bar{z}(B+ | A-) - \bar{z}(B- | A-) \} \quad (3.2)$$

or

$$INT(A, B) = \frac{1}{2} \{ \bar{z}(A+ | B+) - \bar{z}(A- | B+) \} - \frac{1}{2} \{ \bar{z}(A+ | B-) - \bar{z}(A- | B-) \} \quad (3.3)$$

where $\bar{z}(B+ | A+)$ denotes the average of all responses of the experiments where both A and B are + and so on. The expression in the first part of the RHS of (3.2) gives the measure of the main effect of B when A is + and is called the conditional main effect of B at the + level of A . Similarly the second part of the RHS estimates the main effect of B when A is - and is called the conditional main effect of B at the - level of A . Notationally these are expressed as

$$ME(B | A+) = \bar{z}(B+ | A+) - \bar{z}(B- | A+) \quad (3.4)$$

and

$$ME(B | A-) = \bar{z}(B+ | A-) - \bar{z}(B- | A-) \quad (3.5)$$

Therefore the interaction between the factors A and B can be expressed as follows

$$\begin{aligned}
 INT(A, B) &= \frac{1}{2} \{ME(B^+ | A^+) - ME(B^+ | A^-)\} \\
 &= \frac{1}{2} \{ME(A^+ | B^+) - ME(A^+ | B^-)\}
 \end{aligned}
 \tag{3.6}$$

A large interaction between two factors would mean a large difference between the two terms in equation 3.6, suggesting that the effect of one factor depends strongly on the

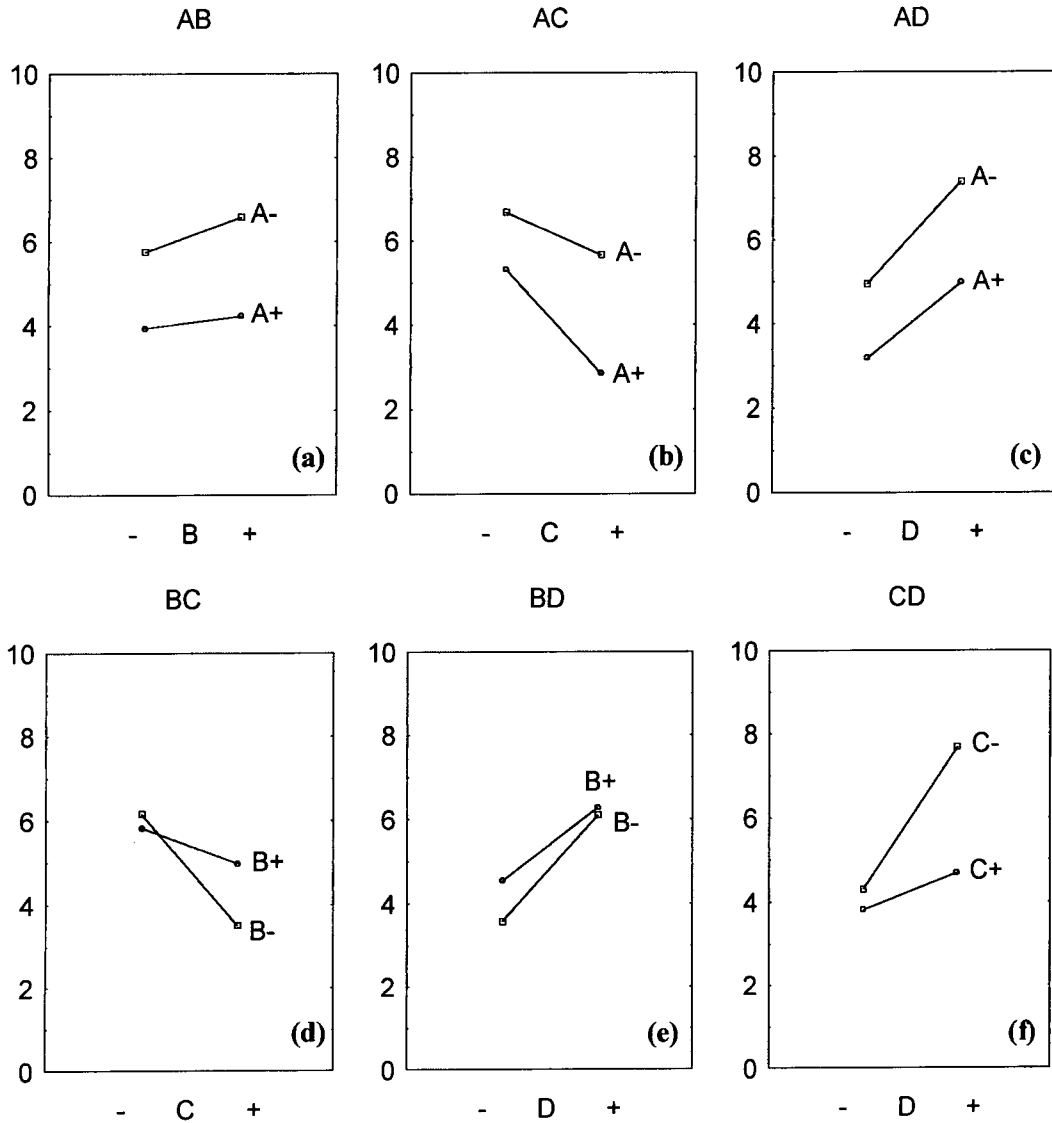


Figure 3.18 Interaction plots showing the effects of (a) distance and temperature, (b) distance and oxygen content, (c) distance and power, (d) temperature and oxygen content, (e) temperature and power and (f) oxygen content and power

level of the other factor. The interaction plots depicting the effects of $INT(A,B)$, $INT(A,C)$, $INT(A,D)$, $INT(B,C)$, $INT(B,D)$ and $INT(C,D)$ are shown in figures 3.18 (a), (b), (c), (d), (e) and (f) respectively.

Figures 3.18 (a), (b) and (c) clearly show that when the distance between the target and the substrate was lower the deposition rate was higher independently of the other factors, although in a higher oxygen containing environment the rate was even lower than in environments containing little oxygen.

However, figure 3.18 (d) shows an interesting effect, where in low oxygen containing ambients the deposition rate was higher at low substrate temperatures, whereas for higher oxygen containing ambients the trend reversed and the deposition rate was greater when the temperature was higher. This again gave a good indication that the reaction of oxygen with the deposited material, which increased at higher temperatures, was an important factor in determining the growth rate. This effect was more clear when the plot of $INT(B,C)$ was compared with that of $INT(C,B)$, which are shown in figure 3.19.

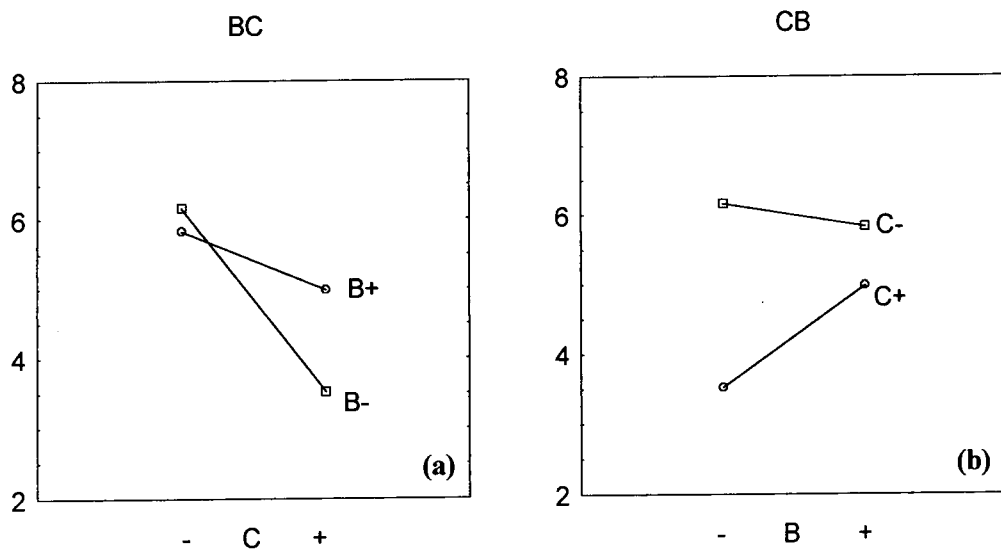


Figure 3.19 Comparison between the interaction plots of (a) temperature and oxygen and (b) oxygen and temperature

Figure 3.19 (a) showing the plot of $INT(B,C)$ is a synergistic plot where the deposition rate decreases with increasing oxygen. The plot of $INT(C,B)$ shows an antagonistic pattern where for low oxygen containing ambients, the deposition rate goes down with increasing temperature but for ambients containing a higher oxygen level the deposition rate increases.

Figure 3.18 (f) indicated that at high power, the rate of deposition was much higher when the oxygen content was lower, but at lower power levels the rate was very similar for both high oxygen and low oxygen containing environments. This suggested that at high incident power the rate was greatly affected by the oxygen content because the number of ions striking the target was high and to replenish the oxygen on the target surface at such a fast rate, a greater concentration of oxygen in the ambient was necessary. Hence for lower oxygen containing ambients the rate was high while in ambients with high oxygen concentration the deposition rate was lower. However when incident power was low the oxygen replenishment of the target could only occur at a much slower rate and thus a lower concentration of oxygen was enough to slow down the rate of deposition. Similarly figure 3.18 (e) showed that the deposition rate at high power was marginally higher for films deposited at high temperatures compared to those deposited at low temperature. At high power the dominant factor was the number of sputtered species ejected from the target and hence when the temperature was changed the difference in deposition rates was very small. However, at low power the reaction of oxygen with the deposited material became dominant and the deposition rate was much higher when sputtering was done at elevated temperatures.

The effect of interaction between three factors (e.g. A , B and C) can be obtained by determining the value of $INT(A,B)$ when C is + and the value of $INT(A,B)$ when C is -.

Notationally this can be expressed as

$$INT(A, B, C) = \frac{1}{2} INT(A, B | C +) - \frac{1}{2} INT(A, B | C -) \quad (3.7)$$

Interaction plots of the above can be done by plotting the different combinations of the levels of the factors *B* and *C* against *D*. This is shown in figure 3.20. It is evident that the largest deposition rate was achieved with high power, low oxygen in the ambient

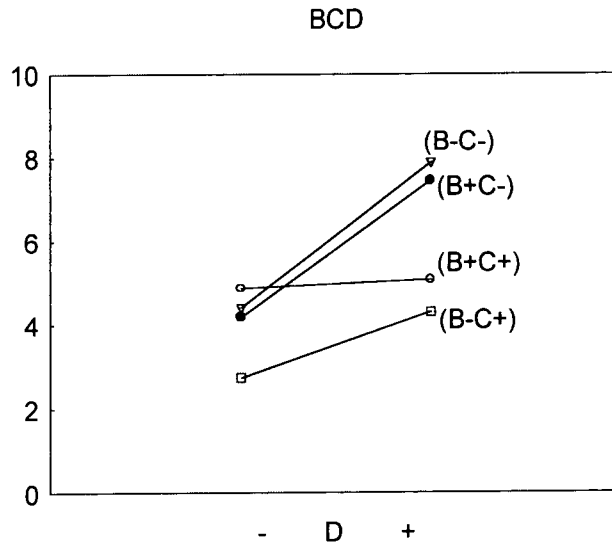


Figure 3.20 Interaction plot showing the combined effect of the substrate temperature, oxygen content in the ambient and power on the deposition rate

and at low substrate temperature. This again indicated that the incident power was the most dominant factor in determining the deposition rate in the sputtering process. But at low power the fastest rate was achieved when both the oxygen content and the substrate temperature were high. This was also seen in the previous interaction plots of the two factors. The other interaction plots are not discussed here, as they did not reveal anything more than what was already discussed.

The interaction effect of all four factors can be calculated in a similar way as for three factors and can be expressed as

$$INT(A, B, C, D) = \frac{1}{2}INT(A, B, C | D+) - \frac{1}{2}INT(A, B, C | D-) \quad (3.8)$$

where $INT(A, B, C | D+)$ represents the values of the interaction of A , B and C calculated using equation 3.7 when D is +.

The values of all the effects of each factor and all the interactions are shown in table 3.4.

Effect	Value	Effect	Value	Effect	Value
A	-2.09	AC	-0.72	ABC	-0.59
B	0.56	AD	-0.31	ABD	0.54
C	-1.74	BC	0.89	ACD	0.02
D	-2.13	BD	-0.38	BCD	-0.29
AB	-0.26	CD	-1.25	ABCD	0.35

Table 3.4 Calculated values of the effects of each main factor and all the interaction factors

3.5.3 HALF NORMAL PLOT

Half normal plots are widely used to assess the distribution of data and in this specific case the values of effects of all the main and interaction factors. This was done by arranging the absolute value of the effects in ascending order and plotting against the following

$$\Phi^{-1}\left(0.5 + \left(\frac{0.5[i - 0.5]}{I}\right)\right) \quad (3.9)$$

where Φ^{-1} is the inverse of cumulative distribution function also known as the percent point function and $i = 1 \dots I$ where I is the number of effects. The plot should produce a

straight line and any deviation from this line would be an indication that the points are not normally distributed. In case of factorial experimental design the values of the effect(s), which deviate from the line in a half normal plot indicate that these factors have a high statistical significance for the response of the experiment. The half normal plot is shown in figure 3.21 and it was evident that the factors *D* and *A* had the highest

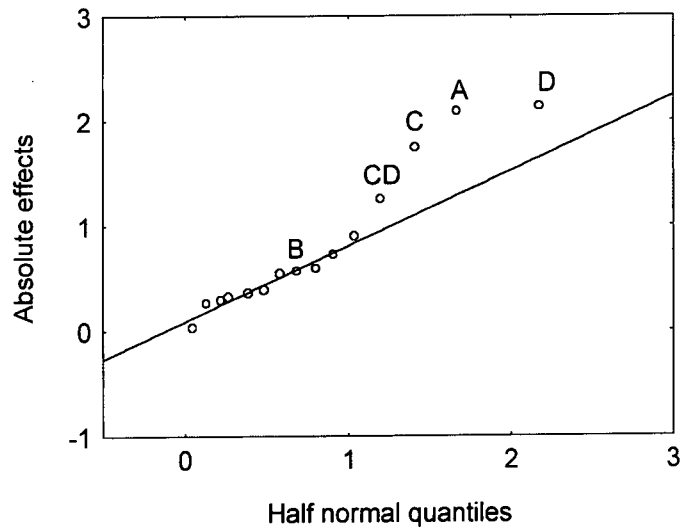


Figure 3.21 Half normal plot showing the significance of the factors *A*, *D*, *C* and the interaction factor *CD*

significance followed by *C* and the interaction *CD*. Their importance was also obvious from the main effect plots and the interaction plots where it was apparent that the target to substrate distance (*A*) and the incident power (*D*) had the greatest influence on the growth rate. From the experiments it was also evident that the oxygen content in the ambient (*C*) played a crucial part.

3.6 CONCLUSIONS

A rf magnetron sputtering system was designed and built for depositing nickel manganate thin films from ceramic targets. A conventional on-axis-sputtering configuration with the substrates positioned above and facing the target was used. The

system was capable of depositing eight films per vacuum cycle and it was possible to control the temperature of the substrates, which could be heated up to 250°C. Sputtering could be carried out in a range of oxygen/argon mixed environments and the composition and rate of flow of the gas could be controlled and monitored. Provision was also made to allow alteration of the distance between the target and the substrates.

The effect of the various process parameters on the growth rate was studied and the growth rate was found to be strongly dependent on the incident power, target to substrate separation, substrate temperature and oxygen content in the sputtering gas. However, the growth rate was found not to be highly dependent on the sputtering pressure and remained largely unchanged when sputtering was done for up to 10 hours. These effects were expected and were consistent with the findings of other researchers.

To assess the degree of influence of the parameters on the deposition rate and also to understand the effects of the inter-dependency of several parameters, a factorial design experiment was carried out. Four of the more important parameters, namely substrate to target distance, power, oxygen content in the ambient and substrate temperature at two levels were chosen for these experiments. The experiment highlighted the effect of the interdependence of the substrate temperature and oxygen content in the sputtering environment on the growth rate. The results showed that the power, the oxygen content in the ambient, the target to substrate separation and the interaction between the incident power and the oxygen content were the most significant factors influencing the growth rate. This finding was consistent with the physical relevance of the different mechanisms, which played an important role in determining the deposition rate of the sputtering process.

The next chapter is devoted to the study of various structural properties of the $Ni_xMn_{3-x}O_{4+\delta}$ material system. This will cover both the microscopic and macroscopic aspects of the structure. Discussions about the formation of single phase spinel nickel manganate will also be covered in the chapter. This was necessary to be able to produce a good quality target material for producing thin films, properties of which will be discussed in later chapters.

3.7 REFERENCES

- [1]. Grove, W.R. *On the electro-chemical polarity of gases*, (1852) Philosophical Transaction of the Royal Society of London, **142**, 87.
- [2]. Chopra, K.L. (1969) *Thin film phenomena*. McGraw-Hill Book Company, New York.
- [3]. 98/1 Reactive Sputtering. In *Handbook of thin film process technology* (D. A. Glocker, S. I. Shah and W. D. Westwood, eds), Institute of Physics Publishing, Bristol and Philadelphia (1995).
- [4]. Vossen, J.L., Kern, W. (1991) *Thin film processes II*, Academic Press, Boston.
- [5]. Chapin, J.S. *Sputtering process and apparatus*, (1974) Research and Development Magazine, **25**, 37.
- [6]. Marrows, C.H. (1997) Indirect exchange coupling in sputtered magnetic multilayers. PhD thesis in *Physics and Astronomy*, University of Leeds, Leeds.
- [7]. Probyn, B.S. *Sputtering of insulators in a rf discharge*, (1968) Vacuum, **18**, 253.
- [8]. Logan, J.S., Mazza, N.M., Davidse, P.D. *Electrical characterization of radio-frequency sputtering gas discharge*, (1969) Journal of Vacuum Science and Technology, **6**, 120.
- [9]. Jackson, G.N. *RF Sputtering*, (1970) Thin Solid Films, **5**, 209-246.
- [10]. Okano, H., Tanaka, N., Shibata, K., Nakano, S. *GHz-band surface acoustic wave devices using aluminium nitride thin-films deposited by electron-cyclotron-resonance dual ion beam sputtering*, (1993) Japanese Journal of Applied Physics, **32**, 4052.
- [11]. Lim, W.T., Cho, K.R., Lee, C.H. *Structural and electrical properties of rf-sputtered RuO₂ films having different conditions of preparation*, (1999) Thin Solid Films, **348**, 56-62.
- [12]. Baliga, S., Jain, A.L. *Ni-Mn-O, Cu-Mn-O, Ni-Co-Mn-O films by sputtering and evaporation for infrared detection*, (1990) Proceedings of the 2nd International Conference on Electronic Materials, 393-396.
- [13]. Ohring, M. (1992) *The material science of thin films*. Academic Press, Boston.
- [14]. Hong, S., Kim, E., Jiang, Z.T., Bae, B.S., No, K., Lim, S., Woo, S.G., Koh, Y. *Effects of gas ring position and mesh introduction on film quality and thickness uniformity*, (1997) Materials Science and Engineering, **B45**, 98-101.

- [15]. Jaing, C.C., Cheng, M.H., Chen, J.S., Tsai, C.H., Yeh, P.S., Kao, J.S., Hsiao, H.Y. *Studying layer uniformity of sputter coatings by intensity distribution of plasma spectrum*, (2001) *Applied Surface Science*, **169-170**, 649-653.
- [16]. Jones, R.E., Winters, H.F., Maissel, L.I. *Effect of oxygen on the rf sputtering rate of SiO₂*, (1968) *Journal of Vacuum Science and Technology*, **5**, 84.
- [17]. Maissel, L.I., Glang, R. (1970) *Handbook of thin film technology*. McGraw-Hill, New York.
- [18]. Frach, P., Heisig, U., Gottfried, C. *Aspects and results of long term stable deposition of Al₂O₃ with high rate pulsed reactive magnetron sputtering*, (1993) *Surface and Coating technology*, **59**, 177-182.
- [19]. Davidse, P.D., Maissel, L.I. *Dielectric films through rf sputtering*, (1966) *Journal of Applied Physics*, **37**, 574-579.
- [20]. Evans, T. *Effect of gaseous environment on the structure of sputtered GaAs films on NaCl substrates*, (1966) *Philosophical Magazine*, **13**, 717.
- [21]. Krikorian, E., Sneed, R.J. *Epitaxial deposition of germanium by both sputtering and evaporation*, (1966) *Journal of Applied Physics*, **37**, 3665.
- [22]. Finney, D.J. (1963) *An introduction to the theory of experimental design*. The University of Chicago Press, Chicago.
- [23]. Defay, E., Laberre, M., Semmache, B., Troccaz, M., Barbier, D. *Optimisation of RF magnetron sputtering and RTA-crystallisation of Pb(Zr_{0.52}Ti_{0.48})O₃ thin films by means of the orthogonal array method*, (1998) *Materials Science and Engineering*, **B55**, 123-129.
- [24]. Akiyama, M., Nonaka, K., Xu, C.N., Shobu, K., Watanabe, T. *Statistical approach for optimising sputtering conditions of highly orientated aluminum nitride films*, (1998) *Thin Solid Films*, **315**, 62-65.
- [25]. Wu, C.F.J., Hamada, M. (2000) *Experiments: Planning, Analysis and Parameter Design Optimisation*. John Wiley & Sons Inc, New York.

Structural Properties of Bulk $Ni_xMn_{3-x}O_{4+\delta}$ Material System

4.1 INTRODUCTION

Following the brief description of the construction and performance of the sputtering system, this chapter investigates in more detail the properties of bulk $Ni_xMn_{3-x}O_{4+\delta}$ material systems. Material with five different values of x (1, 0.87, 0.81, 0.77 and 0.74) was prepared in an attempt to vary the ratio of trivalent and tetravalent manganese ions, which are believed to be responsible for conduction in the material. These compositions were chosen so that the same sintering and annealing regime could be followed while still obtaining single phase material. In the literature, the electrical and to a lesser extent the structural properties of a few compositions, such as $x=0.6$ and $x=0.75$ [1] often with addition of other elements such as *Cu*, *Co*, *Li*, etc. [2-4] have been studied. However very few studies have been carried out on both the structural and the electrical properties of the various compositions prepared in this work. This chapter will consider structural aspects such as microstructure, grain size distribution, porosity, shrinkage and the formation of the material by analysis of phases, as a function of sintering and annealing temperature.

4.2 EXPERIMENTAL

4.2.1 CERAMIC PREPARATION

The material was prepared following a conventional ceramic powder processing route, using oxide precursors. Commercial grade nickel oxide (NiO purity 99%) and manganese oxide (Mn_2O_3 purity 98%) procured from Sigma Aldrich was weighed in molar ratios according to the composition using an Oertling NB53 digital scale. The ratio of NiO to Mn_2O_3 used for the five compositions was as follows :

- (a) 1 : 1 for the composition $NiMn_2O_{4+\delta}$,
- (b) 1:1.22 for the composition $Ni_{0.87}Mn_{2.13}O_{4+\delta}$,
- (c) 1: 1.35 for the composition $Ni_{0.81}Mn_{2.19}O_{4+\delta}$,
- (d) 1: 1.43 for the composition $Ni_{0.77}Mn_{2.23}O_{4+\delta}$ and
- (e) 1: 1.52 for the composition $Ni_{0.74}Mn_{2.26}O_{4+\delta}$.

As per the convention followed in the phase diagram of this material system shown in section 2.3, the different compositions will be referred to from now on by the R value, which is the molar percentage of manganese. Hence, the compositions (a), (b), (c), (d) and (e) would be referred to as N2/0.66, N2/0.71, N2/0.73, N2/0.74 and N2/0.75 respectively for the materials annealed after sintering and NQ/0.66, NQ/0.71, NQ/0.73, NQ/0.74 and NQ/0.75 respectively for the materials which were immediately quenched after sintering.

The powders were mixed intimately using pestle and mortar and pressed into 13 mm diameter pellets under a pressure of 0.7 KN mm⁻² using an Apex 10 ton hydraulic press. The pellets were released from the die and placed on a bed of powder of the same composition on an Alsint boat to prevent any contamination from the boat surface onto the pellets. The pellets were then sintered in a Lenton air oven, fitted with an Eurotherm 810 programmable temperature controller, at five different temperatures (800°C, 900°C,

1000°C, 1100°C and 1200°C) for 24 hours. One set of pellets was quenched from the sintering temperature in liquid nitrogen for rapid cooling and another set was cooled down to 800°C in the furnace and annealed for 40 hours. Following the annealing these

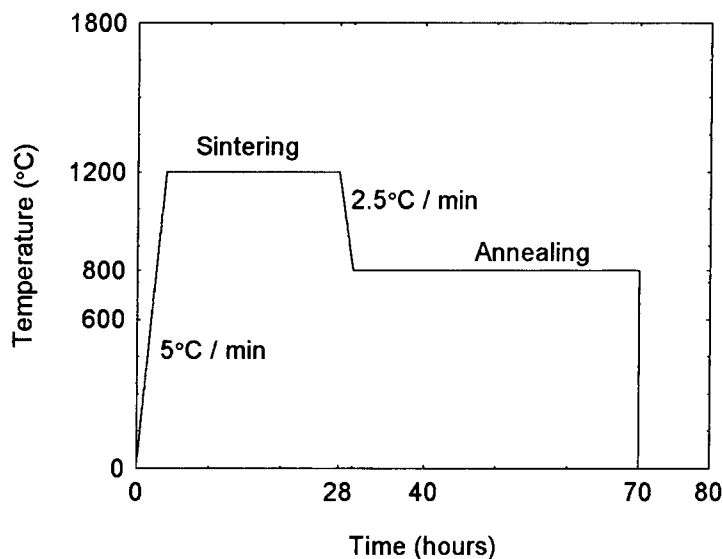


Figure 4.1 Heat treatments (sintering, annealing and cooling) used during ceramic preparation

were then quenched into liquid nitrogen for rapid cooling. The details of the heating cycle are shown in figure 4.1, including the heating and cooling rates used in processing the ceramics.

4.2.2 SCANNING ELECTRON MICROSCOPY

The microstructure of the materials was examined using a Jeol JSMIC848 scanning electron microscope. The samples were put on carbon pads on SEM stem holders and coated with gold using a sputtering system to avoid any charge accumulation on the surface. Elemental analysis was performed using a Link Systems energy dispersive x-ray analyser.

4.2.3 X-RAY DIFFRACTION

Diffraction of x-rays by matter makes it an useful tool for studying various properties of scientifically important materials. The general principles of the x-ray diffraction (XRD) theory can be found in literature [5] and are not discussed here. In the present study the measurements were carried out using the Bragg-Brentano configuration where the source, detector and the normal to the sample surface all lie in the same plane. The instrument used was a commercial Siemens D500 diffractometer with a copper anode, which gives $Cu_{k\alpha}$ radiation with a wavelength of 1.54056 Å. Pellets were finely ground using a pestle and mortar and put in standard sample holders. The measurements were carried out in the range of 10 to 90 degrees (2θ). All the scans were done with a step size of 0.02 degrees per step and the data was collected for 5 seconds per step to obtain a good signal to noise ratio.

4.2.4 WEIGHT AND DIMENSION MEASUREMENT

The weight and dimensions of the pellets after sintering were accurately measured using a digital balance and vernier callipers, which were used to calculate the density and shrinkage. The diameter was measured at three different positions and the width was measured at four different positions and average values were taken.

4.3 CRYSTAL STRUCTURE

In this section the results of structural and compositional measurements of $Ni_xMn_{3-x}O_{4+\delta}$ will be presented and discussed. The first part is devoted to the results obtained from x-ray diffraction measurements, which have been analysed in some detail by

performing Rietveld refinement. In the second part the microstructure and other macroscopic structural results are discussed.

4.3.1 PHASE ANALYSIS

X-ray powder diffraction was carried out for all five compositions in both the annealed and unannealed state after sintering at five different temperatures. The results were then analysed by Rietveld refinement using TOPAS software [6] to determine the lattice parameter and to identify and quantify the phases present in the material sintered at different temperatures. The parameters, which were refined, are listed in table 4.1. Information about the crystal structure of the different phases was obtained from the Inorganic crystal structure database [7].

Parameter	Values
Background	Chebychev polynomial (Refined)
Sample displacement	Refined
Lorentz Polarisation	Set at 26.6
Lattice parameter	Refined
Peak shape	Pseudo-Voigt (Refined)

Table 4.1 The parameters that were considered while carrying out the Rietveld refinement of the materials

The estimation of the errors can be calculated in a number of ways to assess the quality of the fit of the model to the experimental data, as suggested by Young [8]

$$R_{wp} = \left\{ \frac{\sum w_i (y_i(obs) - y_i(calc))^2}{\sum w_i (y_i(obs))^2} \right\}^{\frac{1}{2}} \quad (4.1)$$

$$R_e = \left[\frac{(N - P)}{\sum w_i y_{oi}^2} \right]^{\frac{1}{2}} \quad (4.2)$$

where *obs* and *calc* refer to observed and calculated quantities, N is the number of observations and P is the number of parameters refined, y_i is the count at the i^{th} angle and w_i the weighting factor. The quality of the fit can be assessed by S , the ratio of the R_{wp} (R -weighted pattern) and R_e (R -expected), which is also known as ‘goodness of fit’ and can be expressed as

$$S = \frac{R_{wp}}{R_e} \quad (4.3)$$

Young [8] suggested that the value of S should lie in between 1 and 1.5 for a good fit of the model to the experimental data. A higher value is a strong indication of inadequacy of the model and a value lower than 1 is an indicator of a model that contains more parameters than can be justified.

The x-ray diffraction patterns and the fits obtained from performing the Rietveld refinement of N2/0.71 sintered at 800°C, 900°C, 1000°C, 1100°C and 1200°C are shown in figures 4.2 (a), (b), (c), (d) and (e) respectively. The difference plot is shown below the scan and the indexes of the various phases are shown at the bottom. Samples sintered above 900°C have a single phase with spinel structure. Material sintered at 800°C contained residual amounts of NiO and Mn_2O_3 along with the spinel phase suggesting that the reaction had not gone to completion. The Rietveld refinement of N2/0.66 and N2/0.71 showed that the single spinel phase emerged at 1100°C and

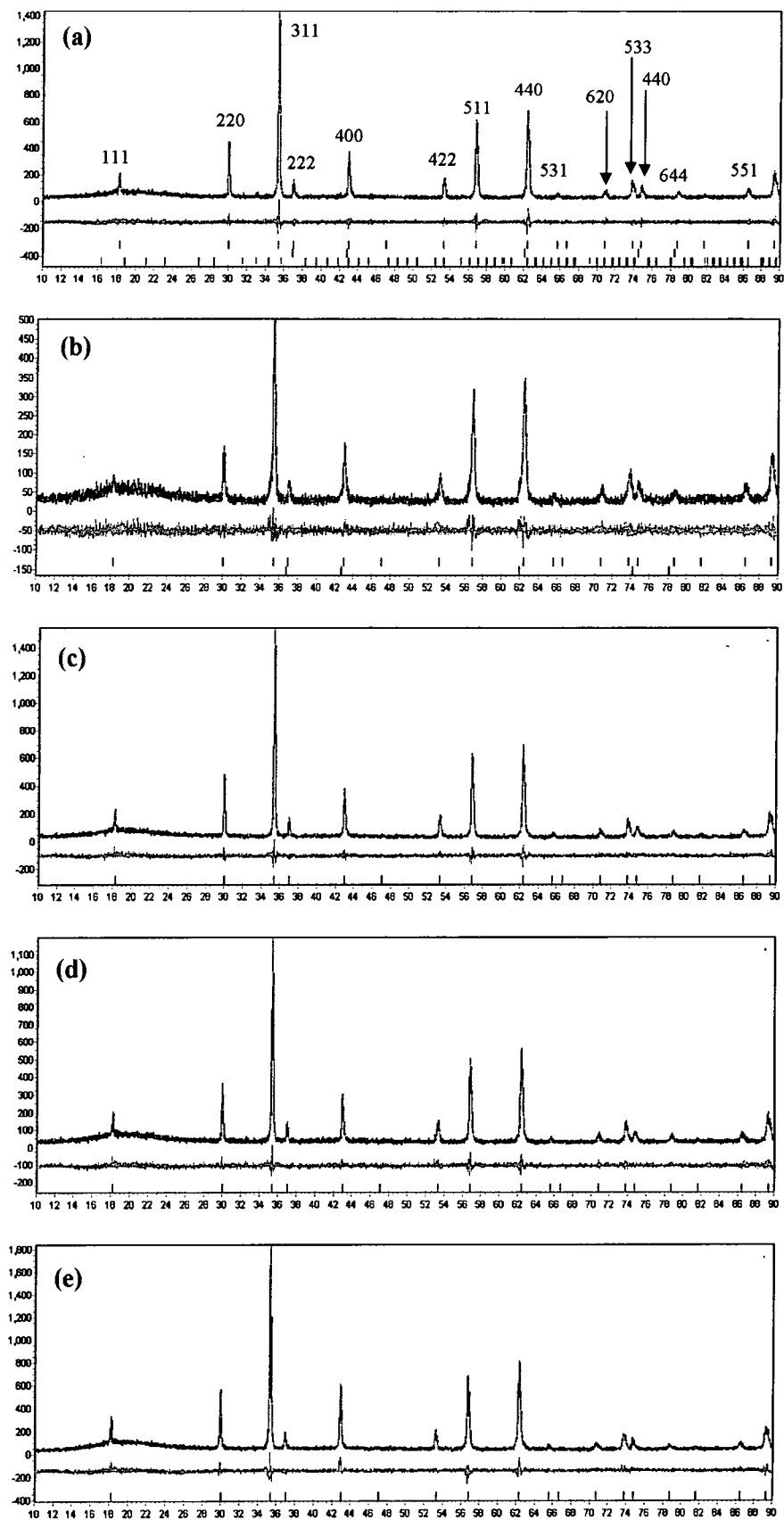


Figure 4.2 X-ray diffraction patterns and Rietveld refinement of the N2/0.71 material sintered at (a) 800°C, (b) 900°C, (c) 1000°C, (d) 1100°C and (e) 1200°C

1000°C respectively. However, for the other three compositions, with lower nickel content, monophasic material was obtained after sintering at temperatures of 900°C and above. Figures 4.3 (a) and (b) show the presence of the various phases as a function of sintering temperature for N2/0.71 and N2/0.75. The error estimates and the goodness of fit from the Rietveld refinement are shown in table 4.2.

The only second phase in N2/0.66 was NiO and no evidence of Mn_2O_3 was found, whereas in the case of N2/0.71 and N2/0.73 both NiO and Mn_2O_3 were present as additional phases. Interestingly, for N2/0.74 and N2/0.75 only Mn_2O_3 was found as a

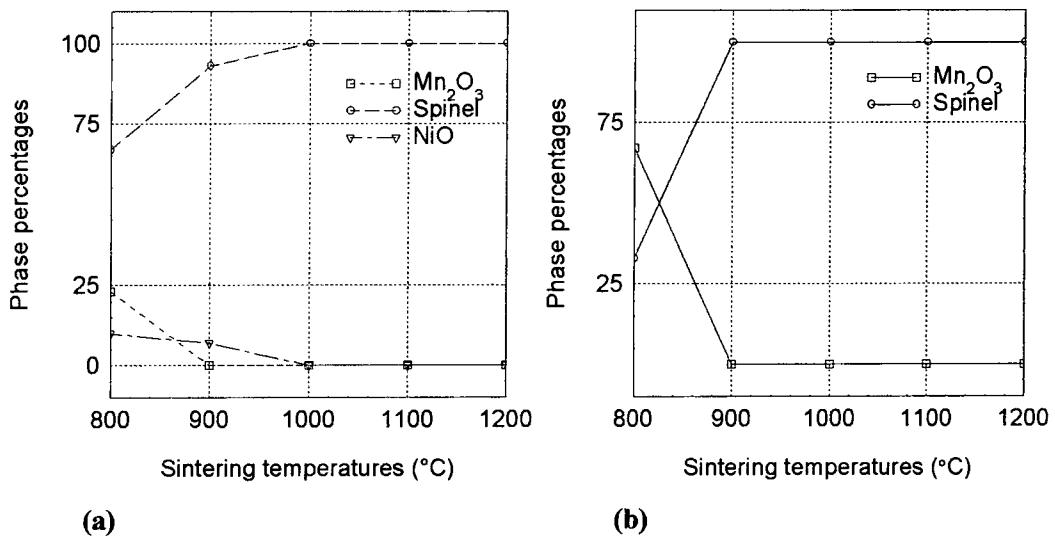


Figure 4.3 Existence of various phases as a function of sintering temperature for (a) N2/0.71 and (b) N2/0.75

Sintering temperature (°C)	N2/0.71 material system			N2/0.75 material system		
	R_e	R_{wp}	S	R_e	R_{wp}	S
800	13.55	15.34	1.13	12.04	13.97	1.16
900	15.55	17.87	1.15	12.74	14.08	1.10
1000	13.41	15.18	1.13	13.00	14.19	1.09
1100	13.77	15.52	1.13	13.26	14.57	1.10
1200	11.98	14.93	1.25	13.16	14.63	1.11

Table 4.2 Values of R_{wp} , R_e and goodness of fit S for the N2/0.71 and N2/0.75 material system

second phase. These results clearly showed that in the temperature regime investigated, the ratio of nickel to manganese in the system determined the composition of secondary phases. For materials sintered at 800°C, a transition from excess NiO to excess Mn_2O_3 (secondary phase) was observed with decreasing nickel content.

Single phase material could not be obtained for any of the compositions, which were directly quenched from the sintering temperature. There were always secondary phases present irrespective of the composition and the sintering temperature. When sintered at 800°C the materials, irrespective of the composition, had three phases: a spinel phase,

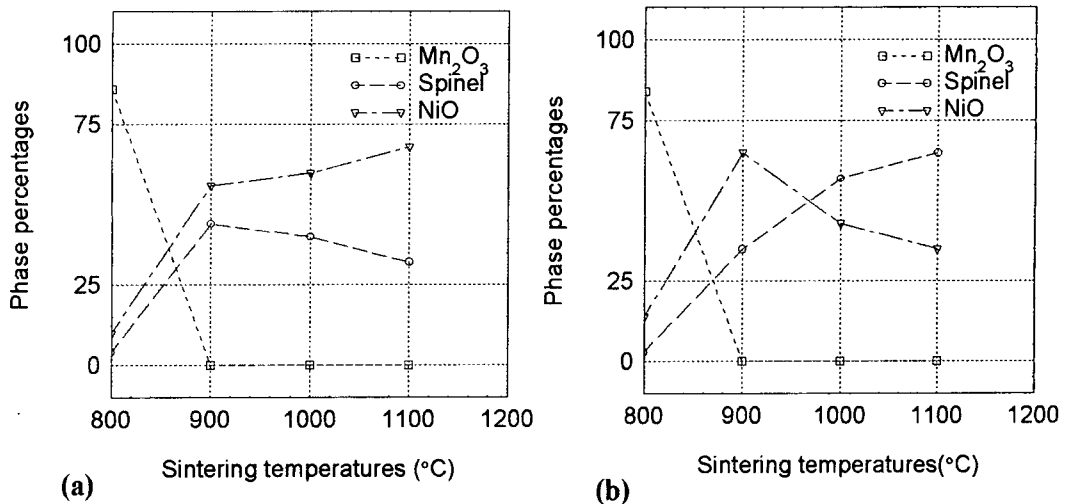


Figure 4.4 Different phases detected after sintering at various temperatures for the material systems (a) NQ/0.71 and (b) NQ/0.75

NiO and Mn_2O_3 . When the materials were sintered above 800°C, NiO was the only secondary phase present along with a spinel phase. There was no evidence of Mn_3O_4 in any of the materials, even in NQ/0.75, which was highly nickel deficient. There was no tetragonal distortion of the spinel phase, known to occur at lower nickel contents ($R > 0.807$) [9]. The presence of secondary phases after sintering at the different temperatures is shown in figures 4.4 (a) and (b) for the NQ/0.71 and NQ/0.75 material systems. Table

4.3 shows the error estimates and goodness of fit from the refinement of the structure. The Rietveld refinement could not be carried out for any of the NQ materials sintered at 1200°C.

Sintering temperature (°C)	NQ/0.71 material system			NQ/0.75 material system		
	R_e	R_{wp}	S	R_e	R_{wp}	S
800	17.92	19.85	1.11	14.43	15.89	1.10
900	20.37	24.27	1.19	15.67	20.74	1.32
1000	18.43	21.79	1.18	16.43	20.04	1.22
1100	18.98	23.45	1.24	16.85	18.38	1.09

Table 4.3 Values of R_{wp} , R_e and goodness of fit S for the NQ/0.71 and NQ/0.75 material system

The lattice parameters obtained from the Rietveld refinement of the x-ray data, showed a systematic increase with decreasing nickel content as shown in figure 4.5 (a). A similar increase of lattice parameter with increasing value of R was reported by Wickham [10]. The increase in lattice parameter was probably because the Mn^{2+} ions, which resulted in order to maintain charge neutrality, are bigger than the Ni^{2+} ions [11]. The variations of the lattice parameter with sintering temperatures, of all the different annealed materials, are shown in figure 4.5 (a). The lattice parameter increased approximately linearly with increasing value of R when sintering was carried out above 900°C although for composition N2/0.66 the lattice parameter was relatively high. When N2/0.66 was sintered at 1000°C, NiO was found as a secondary phase implying that the spinel phase was manganese rich and as a result the lattice was larger than expected.

The lattice parameters of the spinel phase of the materials quenched without annealing also showed an increase with increasing temperature, suggesting that the spinel phase became manganese rich. This implied that increasing amounts of NiO were precipitating

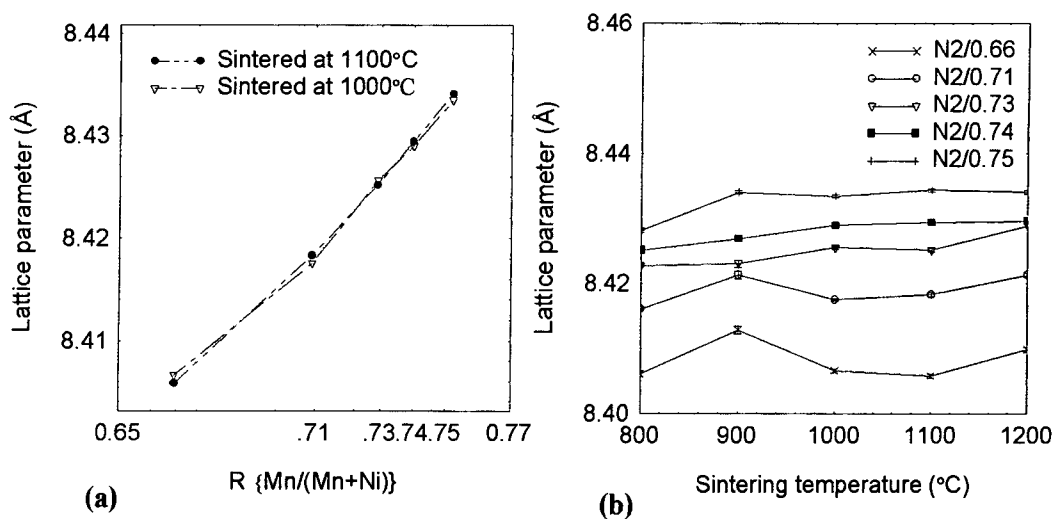


Figure 4.5 Variation of lattice parameter found from the Rietveld refinement of the x-ray diffraction data with (a) composition and (b) sintering temperature

out of the system as the sintering temperature was raised. This was true for the NQ/0.66, NQ/0.71 and NQ/0.73 systems, however for the other two material systems the percentage of the NiO (as indicated by the XRD) phase dropped when sintered at 1100°C. The lattice parameters of the spinel phase in these materials also dropped implying an increase in nickel in the system. However, it should be noted that when NQ/0.74 and NQ/0.75 were sintered at 800°C the lattice parameters were lower than the ones of the corresponding materials annealed before quenching. At 900°C the lattice parameters were very similar to those of the corresponding annealed materials. This could not be explained satisfactorily as, when sintered at 900°C, some amount of Mn_2O_3 should have been present to account for this.

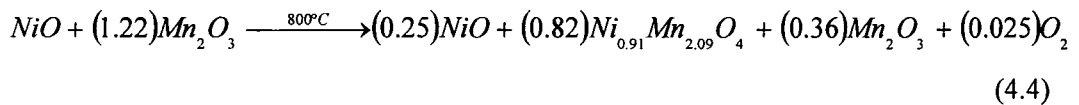
The lattice parameters of the NQ/0.71 system, which was also the composition used for preparing the sputtering target, are listed in table 4.4. The composition of the spinel phase was calculated based on the linear dependence of the lattice parameter on the composition, as shown in figure 4.5 (a).

Sintering temperature (°C)	Lattice parameter (Å)	Composition of the spinel phase
800	8.4217 ± 0.00054	$Ni_{0.91}Mn_{2.09}O_{4+\delta}$
900	8.42943 ± 0.00059	$Ni_{0.77}Mn_{2.23}O_{4+\delta}$
1000	8.43385 ± 0.00031	$Ni_{0.74}Mn_{2.26}O_{4+\delta}$
1100	8.43915 ± 0.00024	$Ni_{0.71}Mn_{2.29}O_{4+\delta}$

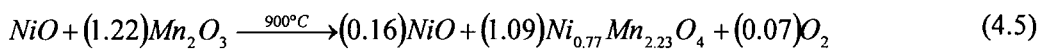
Table 4.4 Lattice parameters of NQ/0.71 after sintering at different temperatures and the calculated phase compositions of the spinel phase at those temperatures

For this material system, based on the compositions of the spinel phase shown in table 4.4, the following chemical reactions are believed to be taking place when sintered at different temperatures

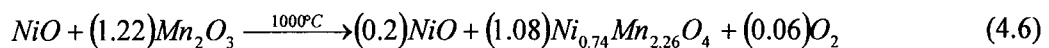
At 800°C



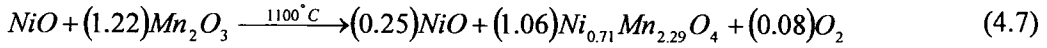
At 900°C



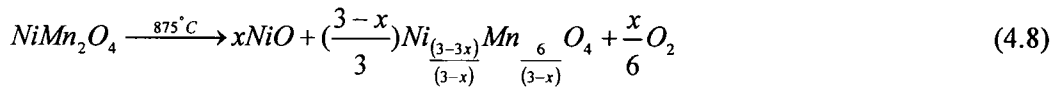
At 1000°C



At 1100°C



For simplicity, all the above equations assumed that the oxygen stoichiometry of the spinel phase was constant, although in reality this could not be true. But they showed that with increasing sintering temperature, the amount of NiO increased. Feltz et. al. [12] proposed that for stoichiometric nickel manganate ($NiMn_2O_4$) the precipitation of NiO can be represented by the following reaction



This is consistent with the findings in this study in as far as that with increasing amount of NiO the ratio of nickel to manganese decreased linearly. Figure 4.6 shows the

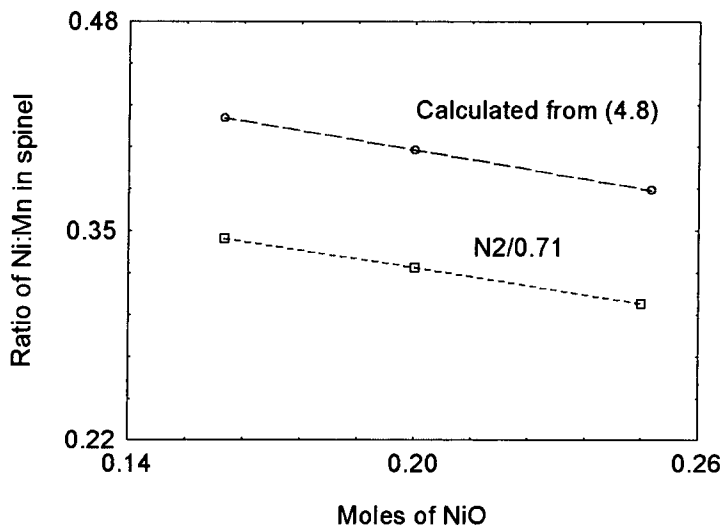


Figure 4.6 A plot of the amount of nickel oxide present as a second phase in the N2/0.71 material system against the ratio of nickel to manganese in the spinel phase

relationship between the number of moles of NiO precipitating out and the ratio of nickel to manganese in the spinel phase both for the N2/0.71 system and that calculated from equation (4.8). The ratio calculated from the equation (4.8), using different values

of x was higher than that found for the N2/0.71 system, which was to be expected as N2/0.71 was nickel deficient compared to the $NiMn_2O_4$ used by Feltz et. al.

The phase diagram proposed by Wickham [10] predicted that in air, N2/0.66 exists as a single phase at temperatures between 730°C and 875°C. However, in this study, single phase material of this composition could only be obtained when sintered at 1100°C followed by annealing at 800°C. This was possibly influenced by the larger particle size of the precursors. A longer sintering time at lower temperatures followed by prolonged annealing would probably be necessary to obtain monophasic material of this composition.

According to the phase diagram, the nickel deficient compositions exists in a single phase up to the following temperatures:

- (a) $R = 0.71$ single phase up to $\sim 950^\circ\text{C}$
- (b) $R = 0.73$ single phase up to $\sim 1000^\circ\text{C}$
- (c) $R = 0.74$ single phase up to $\sim 1050^\circ\text{C}$
- (d) $R = 0.75$ single phase up to $\sim 1125^\circ\text{C}$

The results of this work showed that in all these materials there was evidence of NiO precipitation accompanied by the formation of a manganese rich spinel phase when sintered at temperatures of 900°C up to 1200°C. When sintered at 800°C for 24 hours unreacted precursors were detected in all materials. On the other hand, monophasic material was obtained for all compositions (apart from N2/0.66), when sintered at temperatures in the range of 900°C to 1200°C, if sintering was followed by annealing at 800°C. This strongly suggested that all these materials only existed as a single phase in air within a narrow temperature window between 750°C (possibly lower) and $\sim 800^\circ\text{C}$,

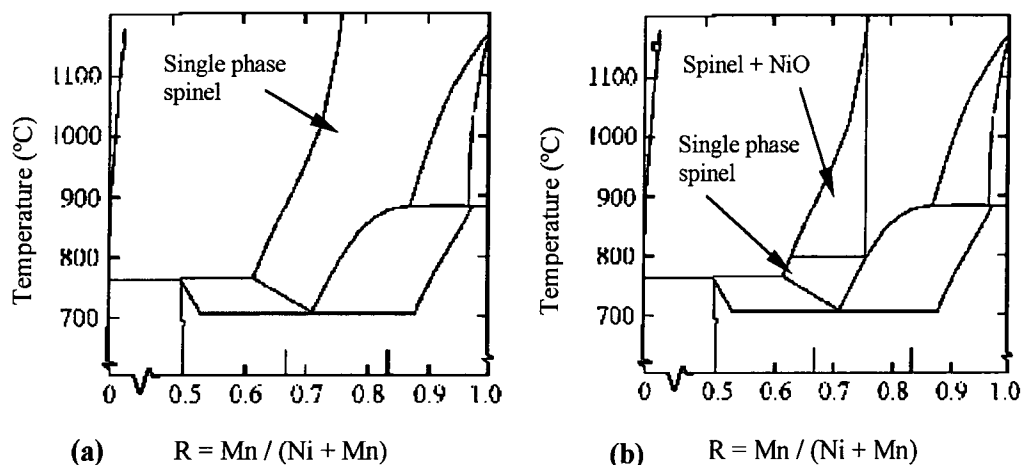


Figure 4.7 Phase diagram of $Ni_xMn_{3-x}O_{4+\delta}$ (a) as proposed by Wickham and (b) as found from experiments in this study

and not in the wider temperature range suggested in the literature. A modified phase diagram applicable to $Ni_xMn_{3-x}O_{4+\delta}$ ($x = 1, 0.87, 0.81, 0.77$ and 0.74) for the region investigated in this work is shown in figure 4.7 (b). The lower limit of temperature in the phase diagram for the single phase spinel region has not been altered. The phase diagram suggested by Wickham is shown in figure 4.7 (a).

4.3.2 ELEMENTAL ANALYSIS

The EDAX analysis was carried out on samples that had been sintered at 1200°C and annealed at 800°C for all five material systems. The results of the EDAX for N2/0.71 and N2/0.75 are shown in figures 4.8 (a) and (b), which show the nickel and manganese K -lines (both K_α and K_β). Apart from oxygen at very low energies, no other peaks were present in the spectra, which confirmed that there were no other significant contaminants (>1%) in the materials.

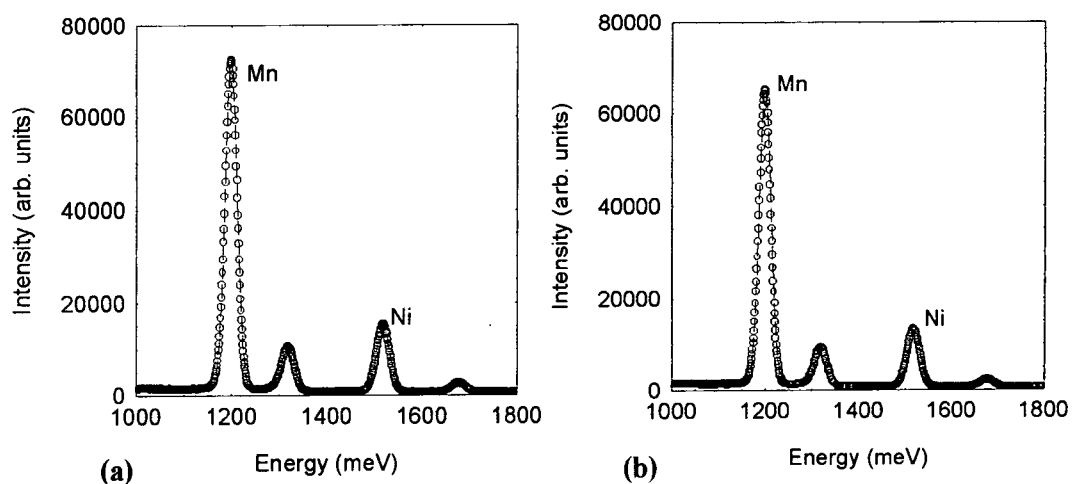


Figure 4.8 EDAX spectra showing the characteristic K peaks of nickel and manganese of (a) N2/0.71 and (b) N2/0.75

Quantitative analysis was undertaken to find the nickel to manganese ratio using Avalon (PGT Ltd, UK) software, which carried out ZAF corrections. The results are shown in table 4.5 and were in good agreement with the precursor ratios used for the different compositions.

	Value of R calculated from the precursor composition and from EDAX analysis				
	N2/0.66	N2/0.71	N2/0.73	N2/0.74	N2/0.75
EDAX	0.67	0.71	0.72	0.73	0.74
Precursor	0.667	0.709	0.729	0.740	0.752

Table 4.5 Comparison of the value of R found from EDAX to that calculated from the precursor ratios

Elemental mapping was carried out on cross sections from several samples sintered at different temperatures. The elemental maps of N2/0.71 sintered at 800°C are shown in

figure 4.9. It was evident that after sintering at 800°C there were second phases present visible as bright contrast regions in the manganese map and corresponding dark

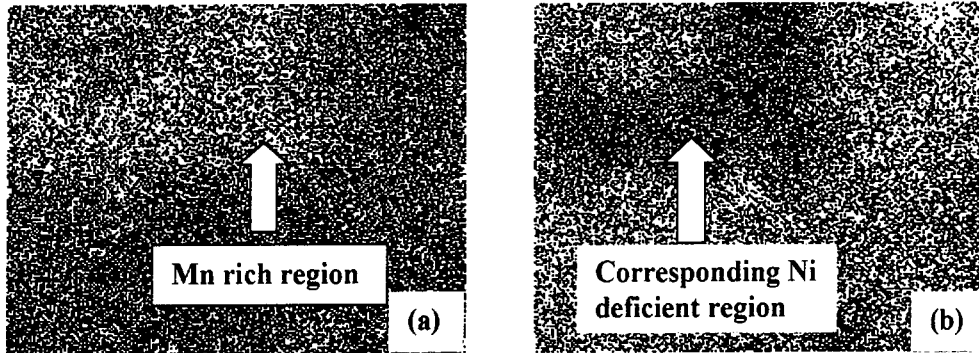


Figure 4.9 Elemental mapping of a cross section from a pellet of N2/0.71 sintered at 800°C (245 μm x 185 μm) (a) manganese distribution and (b) nickel distribution

regions in the nickel map. This was the unreacted manganese oxide phase, which was also detected in the x-ray diffraction experiments. Figure 4.10 shows the elemental mapping of a cross section of N2/0.71 after sintering at 1200°C. The maps were homogeneous suggesting completion of the reaction and formation of material without any detectable segregation of second phase.

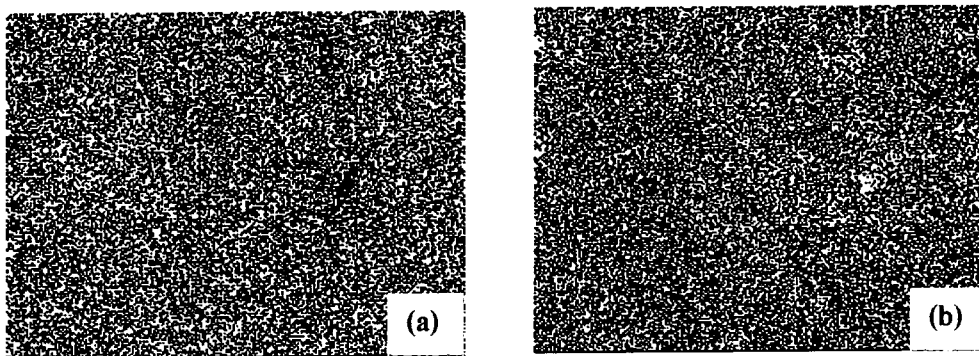


Figure 4.10 Elemental mapping of a cross section from a pellet of N2/0.71 sintered at 1200°C (245 μm x 185 μm) (a) manganese distribution and (b) nickel distribution

4.4 MICROSTRUCTURE

The microstructures of all the materials were studied using SEM and showed very similar trends. The micrographs of the N2/0.71 material system sintered at 800°C, 900°C, 1000°C, 1100°C and 1200°C are shown in figures 4.11 (a), (b), (c), (d) and (e)

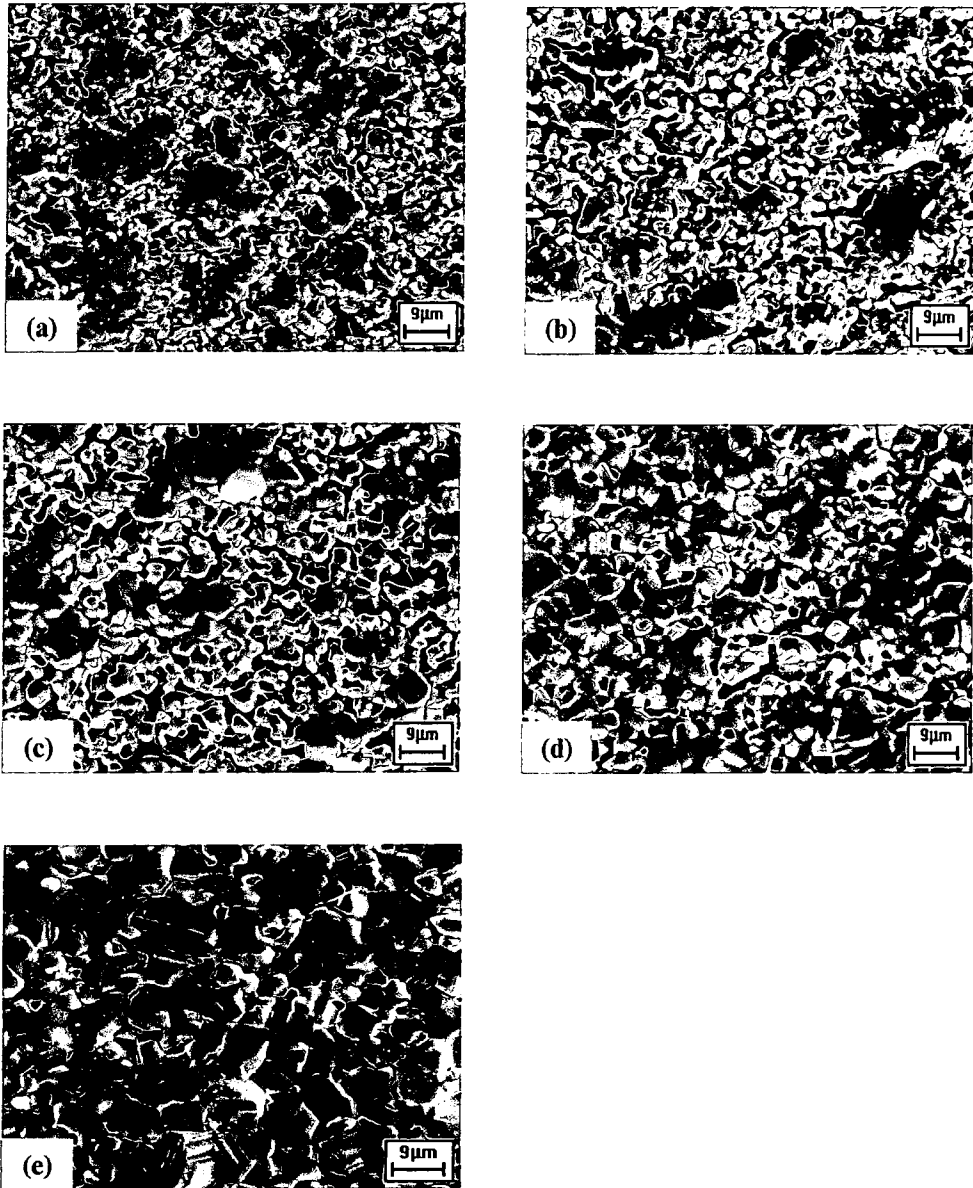


Figure 4.11 SEM micrographs (x 1k magnification) of N2/0.71 material system sintered at (a) 800°C, (b) 900°C, (c) 1000°C, (d) 1100°C and (e) 1200°C

respectively. Uniform microstructure with a significant decrease in porosity and a systematic increase in grain size could be observed in the micrographs of materials sintered above 900°C. A marked difference in porosity was noticed for materials sintered at 1100°C and 1200°C, although these are images of the surface and bulk porosity may be different. This will be discussed in more detail in section 4.5.2. Most of the larger grains in the microstructure had more faces than the smaller grains (which had on average 5-6 sides). This was consistent with the theory, which predicts that grains with a greater number of faces grow more rapidly than the ones with fewer sides. In the materials sintered at 1100°C and 1200°C some terracing can also be seen suggesting increased ordering of the structure.

Although micrographs of only the N2/0.71 system are presented here, the trends of formation of the microstructure were very similar for all the other material systems. The surface porosity in all the systems showed a marked decrease after sintering at 1100°C.

4.4.1 GRAIN SIZE DISTRIBUTION

An important aspect of the microstructure of ceramics is the distribution of grain sizes and its dependency on various process parameters. In this work the effect of sintering temperature has been analysed in some detail. The distribution of grain sizes has been fitted to a Rayleigh distribution function (equation 4.9), which has been used to describe grain size distribution by other researchers [13].

$$N(r) = ar \exp(-br^2) \quad (4.9)$$

where a and b are constants and r is the radius of the grains. An estimation of the mode size (r_0) can be determined from the above expression and will be used to represent the grain sizes.

$$r_0 = \sqrt{\frac{1}{2b}} \quad (4.10)$$

The analysis was done using CGS2 software [14]. The grain boundaries were marked from the SEM micrograph on acetates, which produced a skeleton image of the micrograph showing only the boundaries. This was then scanned into a bitmap image and analysed by the software, which identified the grain boundaries and then located the centroid of each completely closed section (grain). Once this was done it fitted the largest possible circle in each section. The radius of this circle gave an estimate for the grain size. The whole procedure is illustrated in figures 4.12 (a), (b) and (c), which show a SEM micrograph, the corresponding skeletal image and the distribution of the grain

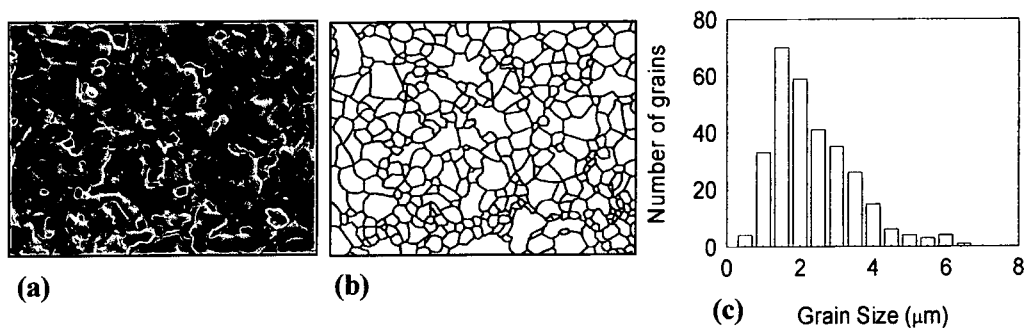


Figure 4.12 Steps of the procedure to obtain the grain size distribution using CGS2 software (a) SEM micrograph, (b) skeleton image depicting only the grain boundaries and (c) the grain size distribution

sizes obtained. The ideal shape of the grains, which could be analysed, using this software would clearly be hexagonal as circular grains do not exist in reality. Hence the analysis does have a degree of error but the large number of grains that can be analysed using this software outweighs this disadvantage. As the size of the grains varied quite significantly, different magnifications were used for analysing materials sintered at different temperatures, to allow analysis of a similar numbers of grains. This was also done to avoid including too many pores in the grain size data, as the software does not

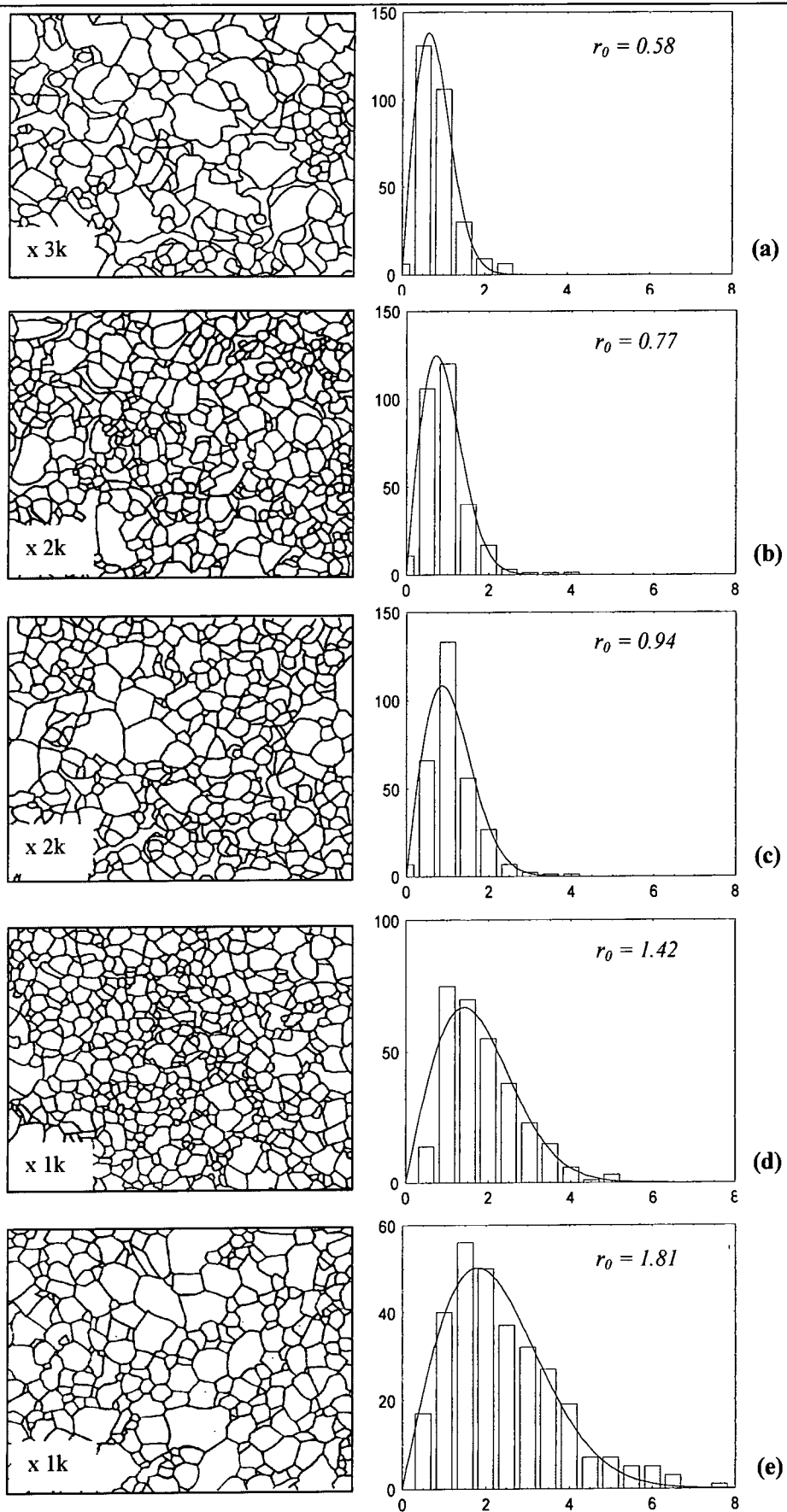


Figure 4.13 The skeleton image of the microstructure and the grain size distribution of $N2/0.71$ sintered at (a) 800°C, (b) 900°C, (c) 1000°C, (d) 1100°C and (e) 1200°C

discriminate between pores and grains. Much effort was expended into locating regions in the material sintered at lower temperatures (800°C and 900°C), where the number of pores was significantly lower than the number of grains. In most cases the size of the pores was comparable to that of the grains.

The results of the analysis for N2/0.71 material system sintered at 800°C, 900°C, 1000°C, 1100°C and 1200°C are shown in figures 4.13 (a), (b), (c), (d) and (e) respectively. The mode size for the distribution function for each material is shown in the figure as well. Figure 4.14 shows a plot of $\ln(r_0)$ as a function of inverse of

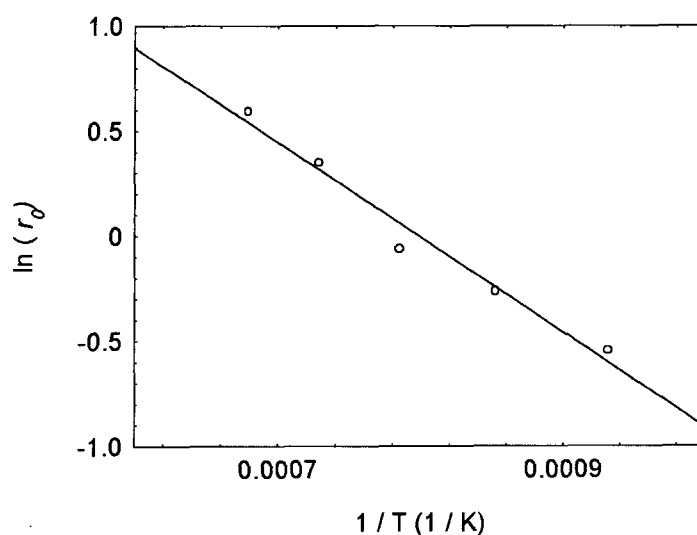


Figure 4.14 Plot showing dependence of the mode size on sintering temperature for the material system N2/0.71

temperature (Arrhenius type plot), which exhibits a reasonably good linear relationship. The rate of grain growth is known to be exponentially dependent on temperature, which will be discussed later in this section. Similar behaviour was seen for all the other material systems as well. The values of the mode sizes for all the different material systems are given in table 4.6.

Sintering temperature (°C)	Value of mode size (r_0) of the grain size distribution function for the different material systems			
	N2/0.66	N2/0.73	N2/0.74	N2/0.75
800	0.56	0.60	0.67	0.59
900	0.79	0.75	0.79	0.76
1000	0.99	0.98	1.07	1.16
1100	1.41	1.30	1.47	1.51
1200	1.74	1.62	1.83	1.83

Table 4.6 Value of the mode sizes obtained from fitting the Rayleigh distribution function to the grain size distribution of different materials

Grain growth in ceramics can be described in terms of an aggregate of fine-grained crystals, which increase in size when heated at high temperatures. The process is driven by the fact that the total grain boundary area decreases as the number of grains decreases. This in turn reduces the total surface energy associated with the grain boundaries. There is also an energy difference ΔG across a grain boundary and it depends on the boundary energy γ , the radii of curvature of the two grains r_1 and r_2 and the molar volume V' , which drives the movement of the grain boundaries. This energy difference can be expressed as [15]

$$\Delta G = \gamma V' \left(\frac{1}{r_1} + \frac{1}{r_2} \right) \quad (4.11)$$

The rate at which the boundary moves depends on the radius of curvature of the boundary and the rate at which the atoms can jump across the boundary. Figure 4.15 shows the energies involved when an atom jumps from one grain to the other. The net rate at which the grain boundary moves is determined by the difference in the frequency of forward and reverse jumps.

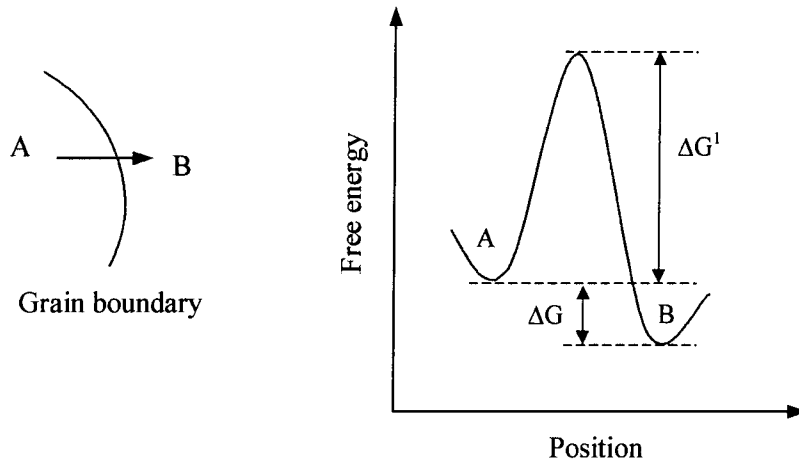


Figure 4.15 Energy changes that takes place when an atom jumps from one grain to the next over a grain boundary (reproduced from [15])

The frequency of the forward and reverse jumps can be expressed as [15]

$$f_{AB} = \frac{RT}{Nh} \exp\left(-\frac{\Delta G^1}{RT}\right) \quad (4.12)$$

$$f_{BA} = \frac{RT}{Nh} \exp\left(-\frac{\Delta G^1 + \Delta G}{RT}\right) \quad (4.13)$$

where N is the Avagadro's number of atoms, h is the Planck's constant and ΔG^1 is the energy difference between the atom and the grain boundary. So the net frequency of forward jumps would be the difference between equation (4.12) and (4.13), which can be expressed as

$$f_{net} = \frac{RT}{Nh} \exp\left(-\frac{\Delta G^1}{RT}\right) \left(1 - \exp\frac{\Delta G}{RT}\right) \quad (4.14)$$

Using equation (4.11), replacing ΔG^1 by $\Delta H^1 - T\Delta S^1$ and expanding the term between the second bracket, the net rate of forward movement of the grain boundary U can be expressed as

$$U = \left(\frac{RT}{Nh}\right) (\lambda) \left[\frac{\gamma V'}{RT} \left(\frac{1}{r_1} + \frac{1}{r_2} \right) \right] \exp \frac{\Delta S^1}{R} \exp \left(-\frac{\Delta H^1}{RT} \right) \quad (4.15)$$

where λ is the distance of each jump and hence $U = \lambda x f_{net}$. It can be seen from equation (4.15) that the rate of grain growth is exponentially dependent on the reciprocal temperature and this was found to be consistent with the experimental results illustrated in figure 4.14.

4.5 MACROSCOPIC ASPECTS OF THE MATERIAL

4.5.1 SHRINKAGE

The shrinkage of the material was calculated by measuring the diameter of the pellet in the green body state and then comparing it with the diameter of the sintered pellet.

Figure 4.16 shows the shrinkage of the N2/0.71 material system as a function of

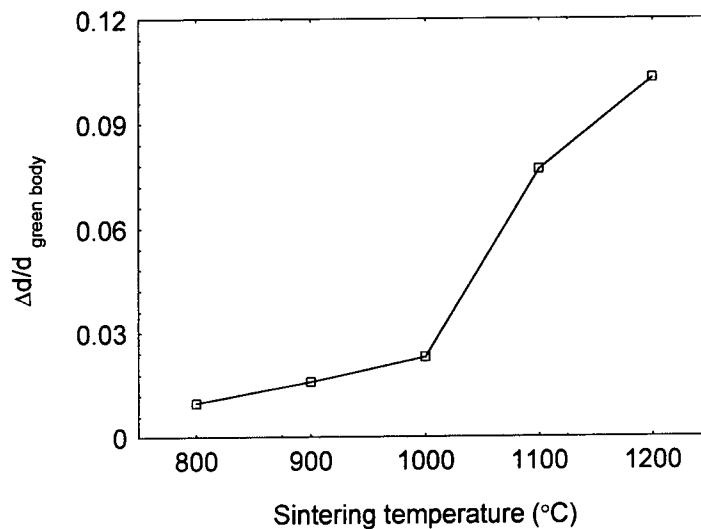


Figure 4.16 Diametric shrinkage of N2/0.71 material system with increasing sintering temperature (each data point represents average value of two measurements)

sintering temperature. The shrinkage increased quite linearly with increasing sintering temperature up to 1000°C and then the gradient changed significantly. At this

temperature, the microstructure also showed quite big changes with substantial grain growth. The values of shrinkage of all the other material systems were very similar and are given in table 4.7.

Sintering temperature (°C)	Values of diametric shrinkage ($\Delta d/d$) for the different material systems			
	N2/0.66	N2/0.73	N2/0.74	N2/0.75
800	0.005	0.005	0.007	0.002
900	0.015	0.012	0.008	0.008
1000	0.023	0.030	0.031	0.019
1100	0.076	0.073	0.072	0.070
1200	0.103	0.110	0.110	0.120

Table 4.7 Values of shrinkage of the various material systems at different sintering temperatures

4.5.2 POROSITY

The porosity of the material was measured indirectly by calculating the density of the pellets after sintering and then comparing that with the density values obtained by Rietveld refinement of the x-ray data. The porosity of the pellets was deduced using the following expression :

$$Porosity(\%) = \frac{Density_{XRD} - Density_{Pellet}}{Density_{XRD}} \times 100 \quad (4.16)$$

The results for the N2/0.66 material system are shown in figure 4.17, where a decrease in porosity with increasing temperature can be seen. Similar to the shrinkage of the pellets, the porosity dropped significantly after sintering at 1000°C and above.

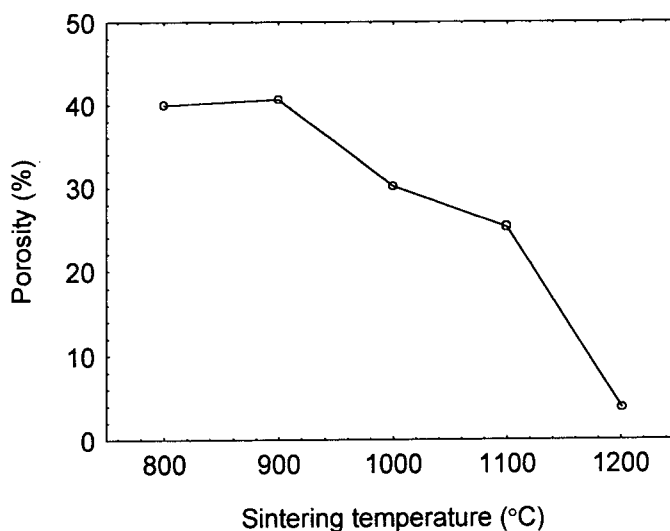


Figure 4.17 Porosity of the pellets of the N2/0.66 material system as a function of sintering temperature (each data point represents average value of two measurements)

4.6 CONCLUSIONS

The structural characteristics of the $Ni_xMn_{3-x}O_{4+\delta}$ ($x = 1, 0.87, 0.81, 0.77$ and 0.74) material system were studied in this chapter. The material was prepared using conventional powder processing with oxide precursors, which were mixed and sintered at different temperatures. Phase purity was assessed by Rietveld refinement of XRD patterns of all the samples. Monophasic material could not be obtained for any of the material systems without an extended annealing process at 800°C . For the materials annealed at 800°C before quenching single-phase spinel material was found for all compositions. Monophasic material was obtained for N2/0.71 when sintered at 1000°C and above and for N2/0.73, N2/0.74 and N2/0.75 when sintered at 900°C or above. However phase pure material was detected for N2/0.66 only when sintered at 1100°C . When sintered at 800°C the only secondary phase present in N2/0.66 was NiO and in the nickel deficient composition (N2/0.75) it was Mn_2O_3 . Intermediate compositions had both NiO and Mn_2O_3 present as secondary phases. The lattice constant of the material

systems showed a linear dependence on the nickel content, with the lattice constant increasing with decreasing nickel content.

In all the materials directly quenched from the sintering temperature, the secondary phase detected for sintering temperatures higher than 1000°C was NiO . When sintered at 800°C, Mn_2O_3 was present along with NiO and a spinel phase. For the compositions NQ/0.66, NQ/0.71 and NQ/0.73, the spinel phase, which was present in the materials sintered at 900°C and above was manganese rich and had a higher lattice constant than the single phase spinel of that composition. For NQ/0.71, the composition of the spinel phase at all the sintering temperatures was calculated from the lattice parameter of the phase. Possible chemical reactions occurring at those temperatures were proposed, although the predicted oxygen loss did not show a monotonic increase with increasing temperature. This may have been due to oxygen non-stoichiometry in the precursors and/or to the fact that the assumption that the spinel phase was always stoichiometric was not valid. The other two nickel deficient spinels exhibited a different behaviour, where the lattice parameter of the manganese rich spinel phase at 1100°C reduced compared to the spinel phase in the material sintered at 1000°C. However the amount of nickel oxide that precipitated reduced as well. This indicated that perhaps with longer sintering time, single phases of these compositions could be obtained at 1100°C. No clear evidence of any tetragonal distortion of the spinel phase was found, although the nickel content of the compositions used in this study was well above the limit where tetragonal distortion has been observed. The results did not completely agree with the previously published phase diagram of this material system, which indicated that nickel deficient materials exist as single phase at temperatures higher than 800°C. That result could not be replicated in this study (e.g for $x = 0.74$ the temperature is predicted to be 1050°C) and hence a modified scheme was proposed. However it must be noted that this

modification was based on the material processing followed in this study and no claims were made that this could be applicable for other synthesis routes.

Both the micro and macroscopic aspects of the structure were studied in some detail. The microstructure of all material systems showed the evolution to a dense ceramic body with well formed grains when sintered at 1000°C and above. The grain size distribution of the N2/0.71 system was extensively discussed and showed a linear relationship when a natural log of the mode size was plotted as a function of inverse temperature. The grain size distribution could be fitted satisfactorily to a Rayleigh distribution function, which has been used to describe the grain size distribution by other researchers. The porosity of the ceramic pellets decreased quite significantly after sintering at 1100°C to about ~23% from ~40% when sintered at 800°C. However the largest decrease was observed for materials sintered at 1200°C, where the porosity of the pellets dropped to ~7%. The density followed a similar trend where the material became denser with increasing sintering temperature. Both the microscopic and macroscopic properties of all the material systems showed very similar trends and hence those were not discussed separately in any great detail.

The following chapter will discuss the electrical characteristics of all the five material systems.

4.7 REFERENCES

- [1]. Brieu, M., Couderc, J.J., Rousset, A., Legros, R. *TEM Characterization of nickel and nickel-cobalt manganite ceramics*, (1993) Journal of the European Ceramic Society, **11**, 171-177.
- [2]. Sarrion, M.L.M., Marales, M. *Preparation and characterisation of NTC thermistors : nickel manganite doped with lithium*, (1995) Journal of the American Ceramic Society, **78**, 915-921.
- [3]. Bhandage, G.T., Keer, H.V. *A correlation of the physical properties of the $Ni_xCu_{1-x}Mn_2O_4$ system*, (1976) Journal of Physics C: Solid State Physics, **9**, 1325-1330.
- [4]. de Vidales, J.L.M., Garcia-Chain, P., Rojas, R.M., Vila, E., Garcia-Martinez, O. *Preparation and characterization of spinel-type Mn-Ni-Co-O negative temperature coefficient ceramic thermistors*, (1998) Journal of Materials Science, **33**, 1491-1496.
- [5]. Cullity, B.D. (1956) *Elements of X-ray diffraction*. Addison-Wesley Publishing Company, Inc., Reading, Massachusetts.
- [6]. Bruker (2000) Topas, General profile and structure analysis software for powder diffraction, Bruker AXS, Karlsruhe.
- [7]. Crystallography <http://cds3.dl.ac.uk/dif/icsd/icsd.html>.
- [8]. Young, R.A. (1996) *The Rietveld Analysis*. Oxford University Press, Oxford.
- [9]. Laberty, C., Alphonse, P., Demai, J.J., Sarda, C., Rousset, A. *Synthesis and characterization of nonstoichiometric nickel manganite spinels $Ni_xMn_{3-x}O_{3.84}O_{4+\delta}$* , (1997) Materials Research Bulletin, **32**, 249-261.
- [10]. Wickham, D.G. *Solid-phase equilibria in the system $NiO-Mn_2O_3-O_2$* , (1964) Journal of Inorganic Nuclear Chemistry, **26**, 1369-1377.
- [11]. O'Neill, H.S.C., Navrotsky, A. *Simple spinels: crystallographic parameters, cation radii, lattice energies, and cation distribution*, (1983) American Mineralogist, **68**, 181-194.
- [12]. Feltz, A., Topfer, J., Schirmer, F. *Conductivity data and preparation routes for $NiMn_2O_4$ thermistor ceramics*, (1992) Journal of the European Ceramic Society, **9**, 187-191.
- [13]. Louat, N.P. *On the theory of normal grain growth*, (1965) Acta Metallurgica, **13**, 227-238.
- [14]. Cousins, M.A. (2001) Microstructure of absorber layers in CdTe/CdS solar Cells. PhD thesis in *Department of Physics* University of Durham, Durham.

- [15]. Kingery, W.D., Bowen, H.K., Uhlmann, D.R. (1960) *Introduction to ceramics*. John Wiley & Sons, New York.

Electrical Properties of Bulk $Ni_xMn_{3-x}O_{4+\delta}$ Material System

5.1 INTRODUCTION

This chapter is devoted to the electrical characterisation of the materials, the structure of which was presented and discussed in the previous chapter. As mentioned there the material compositions were chosen with the intention of varying the ratio of the tetravalent and trivalent manganese ions on the octahedral sites in the crystal structure. Single phase material of all the compositions was prepared to eliminate any effect from secondary phases on the conduction process of the material. Hence the results from the NQ material systems will not be discussed in detail here as these materials all had additional secondary phases. The conductivity of the materials as a function of temperature (100K up to 350K) has been analysed in terms of the various electron hopping models and the suitability of these models is discussed.

5.2 EXPERIMENTAL

5.2.1 CONTACT FABRICATION

Electrical (R - T) measurements were made using evaporated aluminium contacts, which proved to be ohmic. A piece of 99.99% pure aluminium wire was cleaned using acetone to degrease the surface and placed inside the filament of the evaporator. The evaporation was carried out at a pressure of $\sim 5 \times 10^{-4}$ mbar for 2 minutes and the system was allowed to cool down for 15 minutes. The pellet was then taken out and the aluminium was immediately covered with conductive silver paste to prevent oxidation. The silver paste was allowed to dry overnight in a drying cabinet at $\sim 80^\circ\text{C}$. The whole procedure was repeated for putting the contacts on the other face of the pellet. Finally, the edges of the pellets were polished using polishing cloth to remove any silver paste, which could have created a conduction path between the two contacts and enamelled copper wires were soldered on to both faces of the pellets using no-clean flux cored solder wire.

5.2.2 R - T MEASUREMENT SYSTEM

The R - T measurements were carried out in a liquid nitrogen cooled Oxford Instruments DN1704 cryostat system. A schematic representation of the system is shown in figure 5.1. The isolation core of the cryostat was continuously pumped using a water cooled diffusion pump to maintain a constant pressure of $\sim 7 \times 10^{-5}$ mbar. A sample was placed on the cold finger of the cryostat and the sample leads were connected to the appropriate contacts B and D on the cold finger and the cold finger was then loaded into the sample core. This was pumped for 30 minutes and backfilled with helium and then pumped out again. The cycle was repeated 5 times to remove any moisture inside the core. Finally the core was refilled with helium, which acted as the heat exchanging gas and isolated before the liquid nitrogen chamber was filled. The temperature was controlled using an

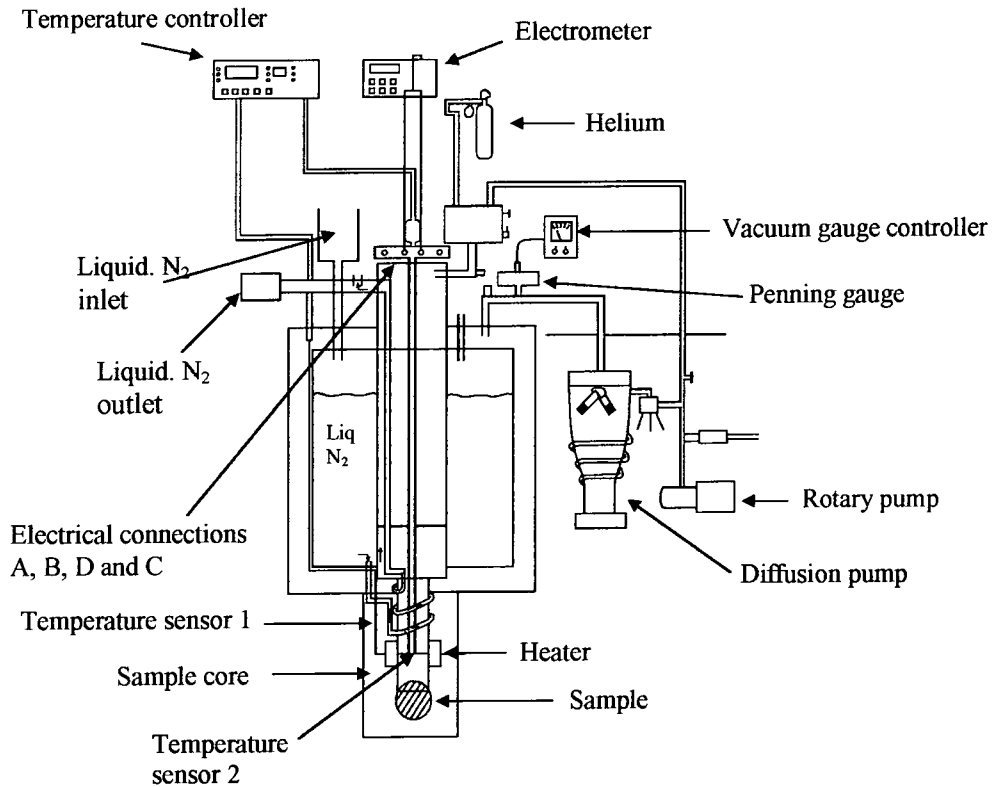


Figure 5.1 A schematic representation of the resistance vs temperature ($R-T$) measurement system

Oxford Instrument ITC 4 temperature controller and the resistance was measured using a Keithley 617 electrometer. The $R-T$ characteristics were recorded under computer control using a purpose written computer software [1].

5.3 ELECTRICAL CHARACTERISATION

Electrical characterisation of all the material systems was carried out by measuring the resistance as a function of temperature. All the materials measured exhibited NTCR characteristics, where the resistance decreased exponentially with increasing temperature. Various conduction models, as discussed in chapter 2, were fitted to the data in an attempt to determine the charge transport mechanism of these materials.

Figures 5.2 (a), (b), (c) and (d) show the data fitted to the Mott variable range hopping model, the Shklovskii and Efros variable range hopping model, the nearest neighbour hopping model and the same model but with temperature dependent pre-exponential

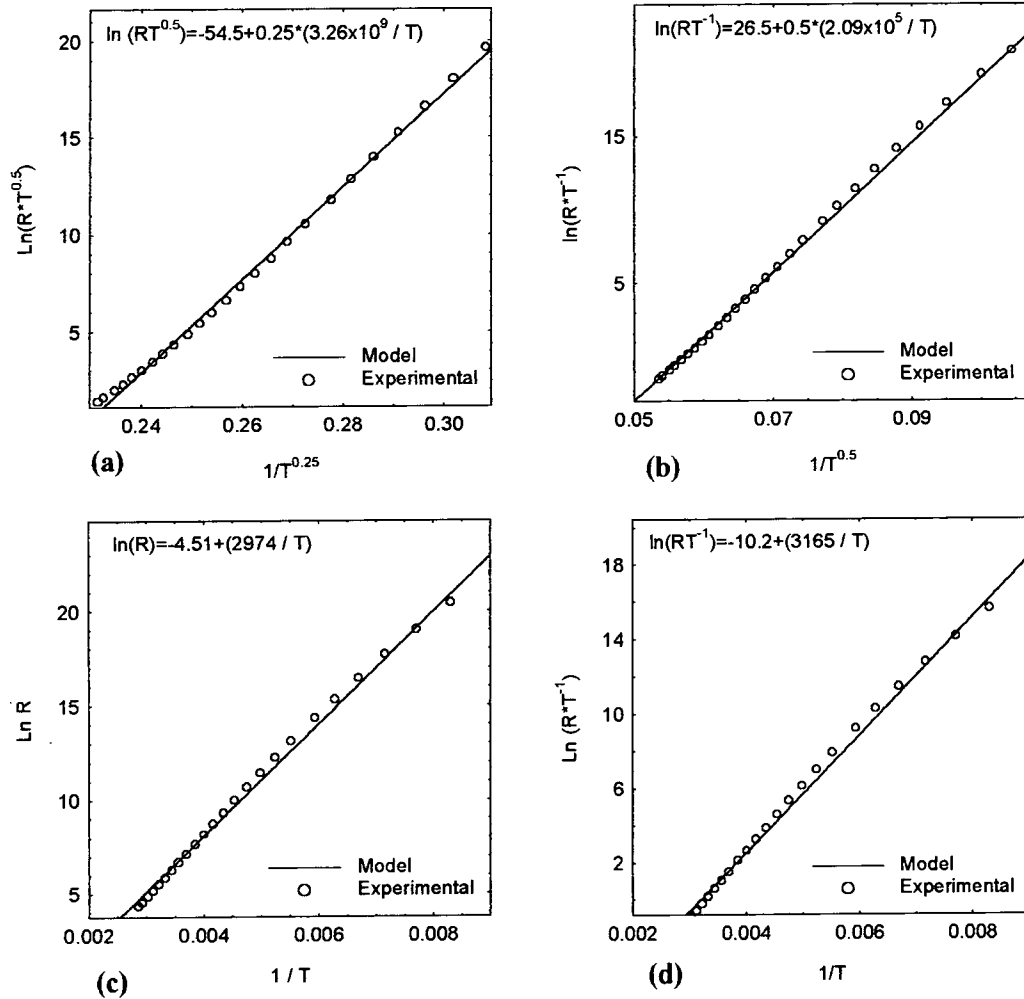


Figure 5.2 R - T data of $N2/0.71$ sintered at 1200°C fitted to (a) Mott VRH model, (b) Shklovskii and Efros VRH model, (c) NNH model and (d) NNH model with temperature dependent pre-exponential term

term respectively. The data used in figure 5.2 was measured for a sample of $N2/0.71$ material system sintered at 1200°C . It is clear from figures 5.2 (c) and (d) that the charge transport was not well described by the nearest neighbour hopping model, especially at lower temperatures. The B -value, which is the characteristic temperature for these models was lower than found by Brabers et. al. [2]. Agreement with the Mott variable range model was better than for the NNH models with a characteristic



temperature T_0 of 3.26×10^9 K. The best fit for the entire range of data was found for the Shklovskii and Efros VRH model, which gave a characteristic temperature T_0 of 2.09×10^5 K. It was evident that both the variable range models needed to be analysed more rigorously before any comments could be made on the applicability of these models to the data. It is important to mention at this point, that though the data presented above was for N2/0.71 sintered at 1200°C, data from all other materials followed similar trends.

5.3.1 MOTT VRH MODEL

The model was described in more detail in chapter 2 where it was shown that the resistivity of the material can be expressed as

$$\rho = C_0 T^{0.5} \exp\left(\frac{T_0}{T}\right)^{0.25} \quad (5.1)$$

where T_0 is the characteristic temperature, which can be described by the following expression

$$T_0 = \frac{\beta}{k_b g(\mu) a^3} \quad (5.2)$$

where β is a numerical constant with a value of 21.2 ± 1.2 . An estimation of the density of states value can be made from the equation 5.2, assuming a to be equal to the Bohr radius. This would represent an upper limit on $g(\mu)$ since a will be larger than that of a hydrogen atom. The calculated values of the density of states of N2/0.71 are shown in table 5.1. The values of T_0 for the other material systems were very similar, in the order

$\sim 10^9$ K. The corresponding values of $g(\mu)$ were unrealistically low implying that this model did not adequately explain the charge transport in these materials. Values of $g(\mu)$

Sintering temperature (°C)	Value of T_0 of N2/0.71 from Mott model (K)	Value of density of states ($eV^{-1} cm^{-3}$)
800	3.48×10^9	4.75×10^{20}
900	3.72×10^9	4.44×10^{20}
1000	3.60×10^9	4.59×10^{20}
1100	3.78×10^9	4.37×10^{20}
1200	3.26×10^9	5.07×10^{20}

Table 5.1 Values of T_0 and the corresponding values of the density of states of the N2/0.71 material system

are not available in the literature for this material, but for lanthanum manganite the estimation was found to be in the order of $10^{23} eV^{-1} cm^{-3}$ [3]. To have a similar value of density of states the characteristic temperature would have had to be 3 orders of magnitude lower. Values of T_0 obtained for the NQ material series were in the same order of magnitude and hence will not be discussed in any detail here.

5.3.2 SHKLOVSKII AND EFROS VRH MODEL

This model was also discussed in chapter 2, where it was shown that the resistivity can be described using the following expression

$$\rho = C_0 T \exp\left(\frac{T_0}{T}\right)^{0.5} \quad (5.3)$$

where T_0 is the characteristic temperature of the material, which can be expressed as

$$T_0 = \frac{\beta_1 e^2}{k_b a \kappa} \quad (5.4)$$

where β_1 is a numerical constant with a value of 2.8. Here, $\kappa = \epsilon_0 \epsilon_r 4\pi$, where ϵ_0 is the permittivity of free space and ϵ_r the relative permittivity of the material. Therefore, using this expression of κ , the equation 5.4 can be rewritten as

$$T_0 k_b = \beta_1 \left(\frac{e^2}{4\pi \epsilon_0 \epsilon_r a} \right) \quad (5.5)$$

This equation then becomes very similar to the expression that describes the energy involved during the interaction between two electrons i.e. [4]

$$\epsilon_D = \frac{e^2}{4\pi \epsilon_0 \epsilon_r r_D} \quad (5.6)$$

with the effective radius equal to the product of $\epsilon_r a_0$. Hence in equation 5.5 the effective radius of the atom can be described as the product of $\epsilon_r a$ (assuming $a = a_0$)

The values of T_0 found by fitting the R - T data for the N2/0.71 system to this model and the corresponding values of the effective radius are shown in table 5.2. The values were

Sintering temperature (°C)	Value of T_0 of N2/0.71 from Sklovskii and Efros model (K)	Value of effective radius (Å)
800	1.98×10^5	2.51
900	2.19×10^5	2.26
1000	2.08×10^5	2.38
1100	1.92×10^5	2.58
1200	1.93×10^5	2.57

Table 5.2 Values of the characteristic temperature T_0 found from the Shklovskii and Efros VRH model and the corresponding value of the effective radius for the N2/0.71 material system

very similar to each other and all were in the order of $\sim 2 \times 10^5$ K. Using these T_0 values, the magnitudes of effective radius were calculated to be in the region of ~ 2.5 Å, which

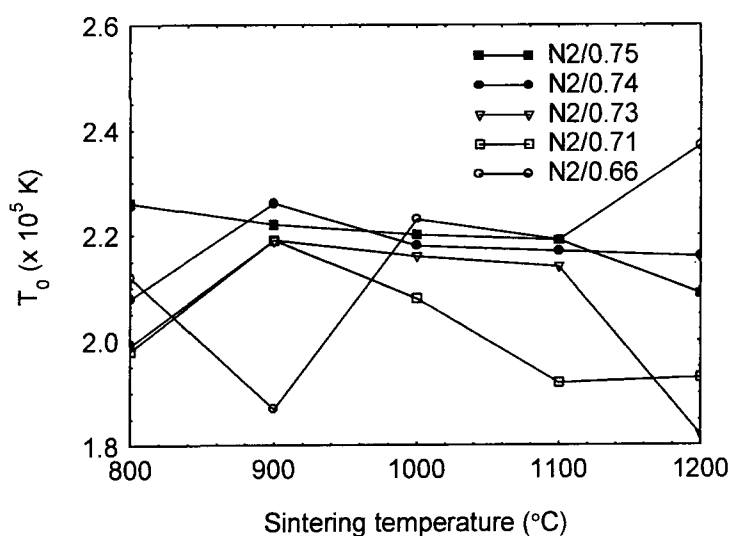


Figure 5.3 Values of T_0 from Shklovskii and Efros VRH model for all the material systems as a function of sintering temperature

is about five times larger than the radius of the hydrogen atom. These values were not unrealistic and warranted further investigation of the applicability of this model. The distribution of T_0 for all the material systems is shown in figure 5.3. No definite trends were seen in the distribution of T_0 values, apart from some indication that the value decreased with increasing sintering temperature. However the changes were not very significant and very little could be concluded from them.

It was quite clear from the above that for all the material systems, the model proposed by Shklovskii and Efros fitted the data best and gave reasonable values of the effective radius calculated using the characteristic temperature. But it is well known for semiconductors that the charge transport mechanism changes as a function of temperature [5]. Therefore it is possible that the models discussed above may well be applicable for a certain temperature range but not necessarily for the whole range over which $R-T$ measurements were carried out. One of the ways to verify this, would be to

analyse the R - T data as proposed by Zabrodskii [6]. In the following section this method of analysis would be discussed and results presented.

5.3.3 ANALYSIS OF 'p'

As discussed earlier (equations (2.24) and (2.25)), the resistivity (or resistance) of this type of materials can be described by the following expression

$$R = R_0 T^{2p} \exp\left(\frac{T_0}{T}\right)^p \quad (5.7)$$

Taking natural log of both sides of the equation (5.7) gives

$$\ln R = \ln R_0 + 2p \ln T + \left(\frac{T_0}{T}\right)^p \quad (5.8)$$

Differentiating equation (5.8) with respect to T^{-1} results in

$$\frac{d(\ln R)}{dT^{-1}} = 0 + 2pT + T_0^p \left[p \left(\frac{1}{T}\right)^{p-1} \right] \quad (5.9)$$

Now multiplying the second term of the RHS of equation (5.9) with T/T and dividing both sides by $1/T$ gives

$$\frac{1}{T} \left[\frac{d(\ln R)}{d(T^{-1})} \right] = -2p + pT_0^p \left(\frac{1}{T}\right)^p \quad (5.10)$$

Taking natural log of both sides of equation (5.10) gives

$$\ln \left\{ \frac{1}{T} \left[\frac{d(\ln R)}{d(T^{-1})} \right] \right\} = \ln \left[-2p + p \left(\frac{T_0}{T}\right)^p \right] \quad (5.11)$$

Assuming that

$$\left(\frac{T_0}{T}\right)^p \gg |2p| \quad (5.12)$$

the following expression is obtained

$$\ln w = \ln p + p \ln T_0 - p \ln T \quad (5.13)$$

where w corresponds to the term inside the brackets on the LHS of the equation 5.11.

The first two terms on the RHS are constants so the expression 5.13 can be rewritten as

$$\ln w = C - p \ln T \quad (5.14)$$

Hence a plot of $\ln w$ vs $\ln T$ would yield a straight line and the slope of the line would be equal to p . This method has been used by other researchers to determine the transport mechanisms in semiconductors [7].

For all the materials analysed, the value of p ranged from 0.4 to 0.7 for temperatures in the range 120K to ~300K. This strongly suggested that the predominant charge transport mechanism in the materials was variable range hopping as proposed by Shklovskii and Efros where the value of p is taken to be 0.5. The values of p as a function of sintering temperatures of all the material systems are shown in figure 5.4. Interestingly, above ~300K a change in the slope in the plot of $\ln w$ vs $\ln T$ was observed for nearly all materials irrespective of the sintering temperature. The results for N2/0.71 sintered at 1200°C are shown in figure 5.5. The change in slope around 300K is quite obvious. However, when a straight line was fitted to the data above this temperature, the slope was much larger than 1, which does not correspond to any of the charge transport

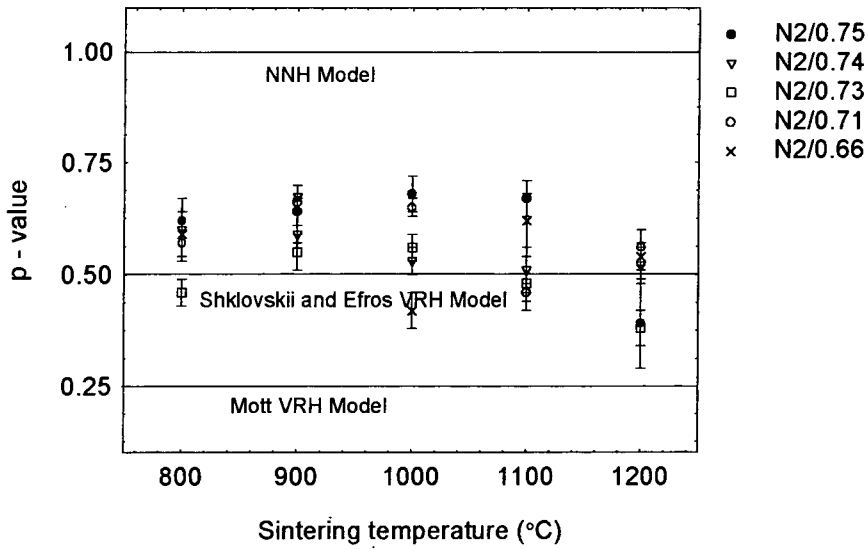


Figure 5.4 Comparison of the p values of different materials with the hopping conduction models (the error bars represents the statistical error of the curve fitting)

models. This did raise questions about the effect of the experimental set-up on the data.

The data was closely studied and irrespective of the material system or the sintering

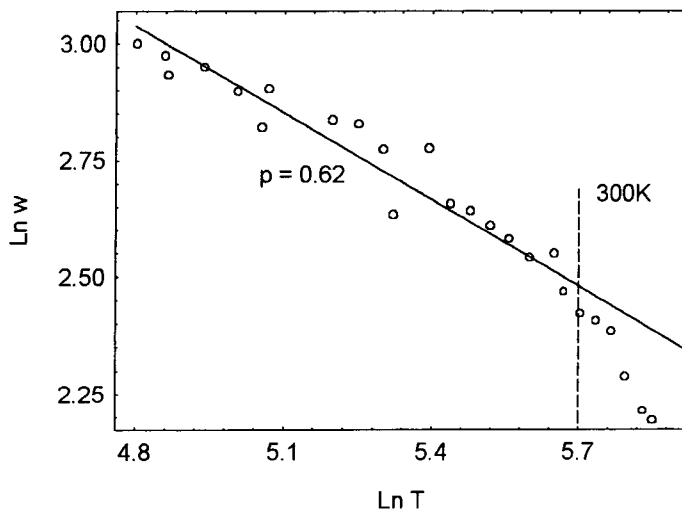


Figure 5.5 Plot of $\ln w$ vs $\ln T$ of N2/0.71 sintered at 1200°C showing the change in slope above $\sim 300K$

temperature this change was noticed in the temperature range of 280K to 310K. When this change of slope occurred, the resistance of the material was in the range of 0.4–2 Kohm. Generally this is not the range of resistance where problems are encountered

with the measuring instruments, which are prone to errors when measuring either very high ($\sim 10^{10}$ Ohms) or very low ($\sim 10^{-2}$ Ohms) resistances. This observation led to the conclusion that it may be a real effect. However, no evidence could be found in the literature about any possible phase change or change in conduction mechanism.

The R - T data of the region, which exhibited a different slope (above 300K) in the $\ln w$ vs $\ln T$ plot, was fitted to the NNH model, where the resistivity can be expressed as

$$\rho = C_0 T \exp\left(\frac{\Delta E}{k_b T}\right) \quad (5.15)$$

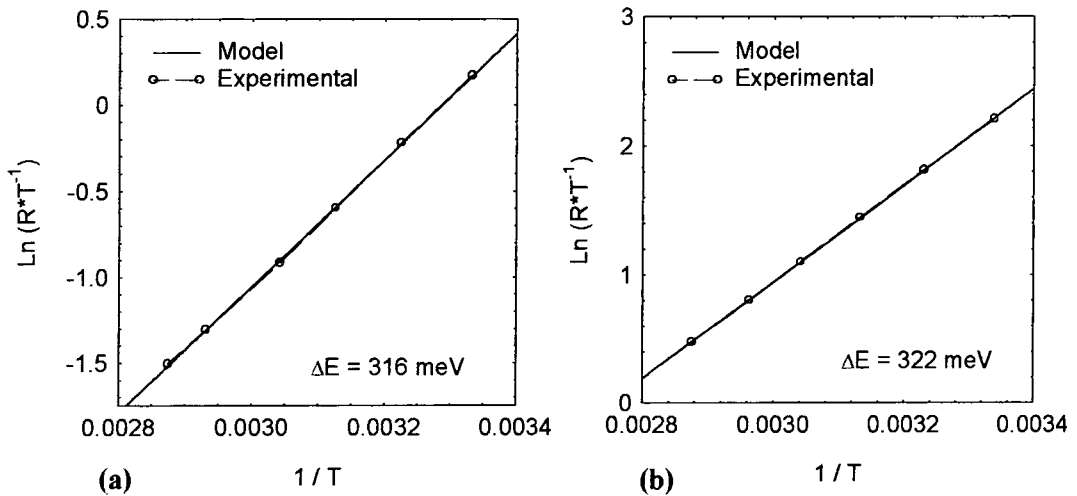


Figure 5.6 R - T data of (a) N2/0.71 and (b) N2/0.75 sintered at 1200°C fitted to the NNH model

The data showed excellent fits to this model and a higher activation energy than when the model was applied to the entire temperature range. The data of N2/0.71 and N2/0.75 sintered at 1200°C fitted to the NNH model are shown in figures 5.6 (a) and (b) respectively. The corresponding activation energy ΔE is shown as an inset in the figures. The values of the activation energy of the N2/0.71 and N2/0.75 material systems sintered at different temperatures are shown in table 5.3.

Sintering temperature (°C)	Value of ΔE of N2/0.71 (meV)	Value of ΔE of N2/0.75 (meV)
800	248	347
900	335	336
1000	331	341
1100	343	326
1200	316	322

Table 5.3 Value of activation energies of N2/0.71 and N2/0.75 material system sintered at different temperatures

The above values were in agreement with published values in the literature [8], with exception of the value for N2/0.71 sintered at 800°C, which was very low. This exceptionally low value may be due to the secondary phases present in the system, as detected in the XRD. These values suggested that the charge transport in this temperature regime would probably be best described by NNH / polaronic model.

5.3.4 RESISTIVITY

The resistivity of the material was determined by measuring the dimensions of the pellets and then using the following expression

$$\rho = R \frac{A}{l} \quad (5.16)$$

where A is the area of one face of the pellet, l is the width of the pellet and R is the resistance. The resistivity values quoted in this section were all measured at 50°C. The resistivities of all the N2 material systems sintered at different temperatures are shown in figure 5.7. Results indicated that for materials with different compositions the resistivity varied differently with the sintering temperature.

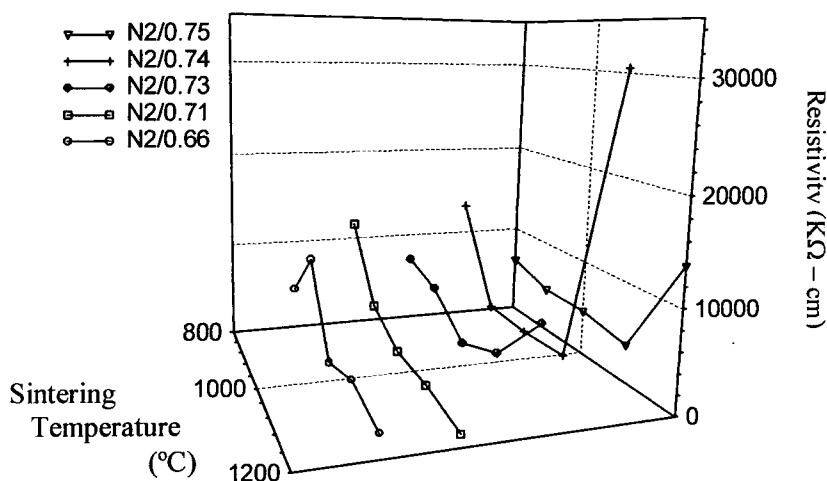


Figure 5.7 The resistivity of all the different material systems sintered at different temperatures (all data points represents the average value of two measurements except the N2/0.74 and N2/0.75 sintered at 1200°C, which represents the average of three measurements)

With the exception of N2/0.66 and N2/0.71 all the materials showed a minimum in the resistivity for a sintering temperature of 1000°C – 1100°C. The two exceptions N2/0.66 and N2/0.71 showed a continuous decrease in resistivity with increasing sintering temperature. The largest resistivity was exhibited by the N2/0.74 material sintered at 1200°C. As discussed in chapter 2, the resistivity depends on the ratio of the Mn^{3+} to Mn^{4+} ions on the *B*-sites of the crystal structure. The ratio of these cations can be altered either by changing the Ni^{2+} concentration in the *B*-sites or by altering the oxygen stoichiometry of the compound. In both cases the manganese ions would change their charge states to maintain charge neutrality.

In this study the Ni^{2+} concentration of the material was altered by a systematic reduction of the nickel content in the composition. This should have altered the charge states in the *B*-sites resulting in a different Mn^{3+} to Mn^{4+} ratio. However, the different sintering temperatures affected the oxygen stoichiometry. Annealing at 800°C for 40 hours reduced the effect of the change in oxygen stoichiometry due to the sintering

temperatures but as the annealing time was kept constant for materials sintered at different temperatures, some differences could be expected.

The pre-exponential term in the resistivity equation of the polaronic model can be described as follows [9]

$$\rho_0 = \frac{k_b T}{e^2 a^2 Nc(1-c)\nu} \quad (5.17)$$

where Nc is the concentration of carriers (Mn^{3+}), $N(1-c)$ is the concentration of vacant sites on which carriers might hop (Mn^{4+}), a is the lattice parameter and ν is the lattice vibrational frequency associated with conduction.

Since the density of charge carriers $Nc(1-c)$ is related to the number of Mn^{3+} and Mn^{4+} cations located in the octahedral sites, it can be expressed as [10]

$$Nc(1-c) = \frac{[Mn^{3+}][Mn^{4+}]}{[Mn^{3+}] + [Mn^{4+}]} \quad (5.18)$$

So an increase in resistivity in the material would be indicated by a decrease of the value of $Nc(1-c)$ which would in turn imply an increase in the value of ρ_0 in the resistivity expression. At any fixed temperature the resistivity is directly proportional to the pre-exponential term and any change in its value (resistivity) would indicate a change in the manganese ion ratio. This was indeed noticed when the C_0 (which is ρ_0 / T) term of the different material systems sintered at the same temperature, was plotted as a function of the composition and compared with the change of resistivity. Figures 5.8 (a) and (b) show the variation of resistivity with composition for materials at 323K, sintered at 1100°C and 1200°C respectively. This difference in the resistivity was due

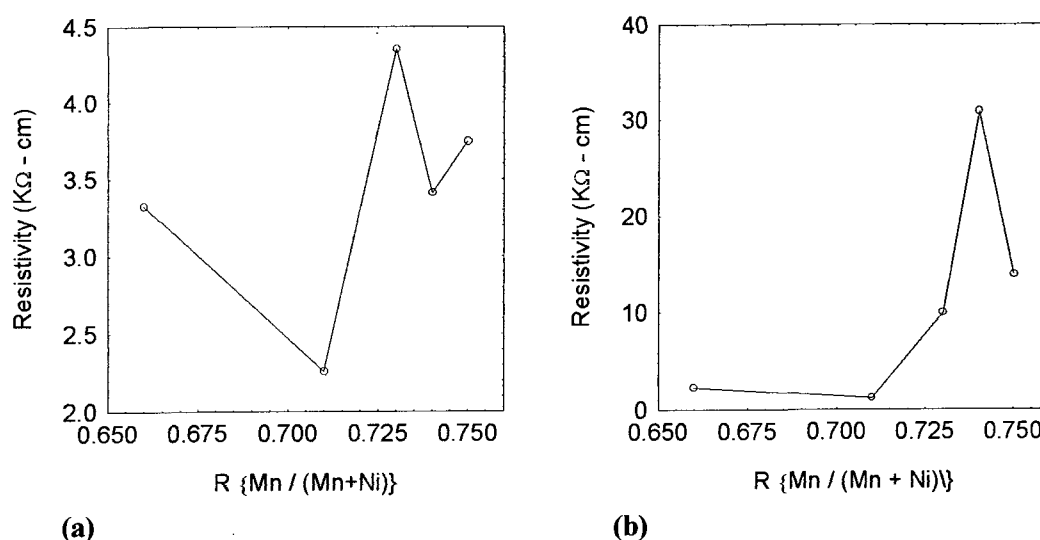


Figure 5.8 Plots of resistivity against composition of materials (each data point represents the average value of two measured values) sintered at (a) 1100°C and (b) 1200°C

to the change in the ratio of Mn^{3+} to Mn^{2+} in the octahedral site. The variation in the distribution of resistivity measured at 323K between materials sintered at 1100°C and 1200°C was a strong indication that the difference in nickel content was not the only factor affecting the resistivity. The sintering temperature, which possibly influenced the oxygen stoichiometry, was equally important in determining the resistivity of the material.

The effect of the second phases, in the materials (NQ) quenched directly from the sintering temperatures, was also investigated. Figure 5.9 compares the resistivity of N2/0.71 and NQ/0.71 sintered at the different temperatures. Materials that were sintered and annealed had a lower resistivity than the corresponding materials that were directly quenched from the sintering temperature, with the exception of the ones that were sintered at 800°C. However, when sintered at 800°C, N2/0.71 was not single phase and small amounts of both NiO and Mn_2O_3 were present as secondary phases. The presence of these secondary phases meant that the charge distribution in the octahedral sites

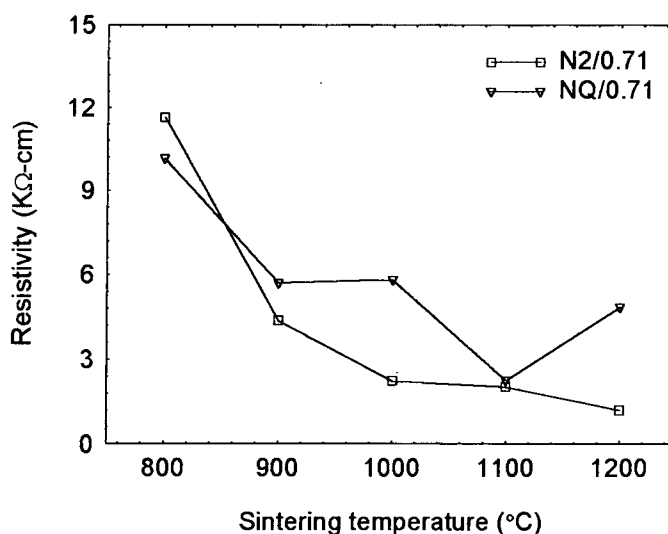


Figure 5.9 The comparison of resistivity between N2/0.71 and NQ/0.71 sintered at different temperatures (each data point represents the average of two measured values)

would have been altered resulting in a change in the ratio of manganese ions. N2/0.71 was single phase when sintered above 900°C and a steady decrease of resistivity was observed, whereas for NQ/0.71 sintered at the same temperatures the data showed different behaviour. This was possibly due to the fact that in the NQ/0.71 material system both the nickel content in the spinel phase and the oxygen stoichiometry were different, whereas in the N2/0.71 materials, sintered from 1000°C onwards, only the oxygen stoichiometry was different. It was evident that the annealing process was successful in producing single phase material however it could not help in restoring the oxygen stoichiometry.

The charge distribution in non-stoichiometric nickel manganate can be expressed as [11]



where ν is the inversion parameter and x is the nickel content. It was mentioned in chapter 2 that the material would be most conductive when the value of the inversion

parameter was 0.67. The different compositions of materials used in this study had decreasing amounts of nickel with N2/0.66 being the most nickel rich and N2/0.75 the least. For simplicity we assumed that the octahedral sites became nickel deficient with decreasing amounts of nickel in the composition. The following mechanisms are thought to take place :

- (a) For fixed compositions, the nickel content remained the same and hence the resistivity should be the same. This was not true as seen from above because with increasing sintering temperature nickel oxide precipitated out along with a loss of oxygen and this caused the manganese ion ratio to change. When these were then annealed at 800°C for 40 hours, the nickel oxide was re-incorporated in the system. However as the oxygen loss was probably different for different sintering temperatures, a similar oxygen stoichiometry could not be achieved and hence differences in resistivity were observed for materials sintered at different temperatures.

- (b) When comparing the resistivity of different compositions sintered at the same temperatures, it was found that the variation of resistivity changed as a function of sintering temperature. Different compositions had varying amounts of nickel and hence a different manganese ion ratio in the octahedral sites. When these were sintered at the same temperatures, different amounts of nickel oxide and oxygen were lost. After annealing at 800°C for a fixed amount of time, most of the nickel oxide was re-incorporated but the oxygen stoichiometry remained different. Furthermore the precipitation of nickel oxide and oxygen was different for different sintering temperatures and hence when the resistivities were compared, different compositions showed maximum resistivity when

sintered at different temperatures. This again emphasised the importance of the oxygen stoichiometry in the system.

In the absence of experimental techniques such as neutron diffraction or TG neither the oxygen content (value of δ in equation 2.5 and 2.6) nor the charge distribution of the materials could be quantified, but the trends obtained from the resistivity data support the above argument quite well. Dependence of the lattice parameter on the resistivity was not observed in this study.

5.4 CONCLUSIONS

All the pellets that were electrically characterised exhibited good NTCR properties with the resistance of the material decreasing exponentially with increasing temperature in the range of 120K to 350K. The conduction mechanism responsible for the charge transport in the materials was investigated by fitting the $R-T$ characteristics to various hopping conduction models. The data apparently fitted the variable range hopping model proposed by Shklovskii and Efros and to a lesser extent the Mott variable range hopping model. The data was less well described by the nearest neighbour hopping models particularly at low temperatures. On closer examination it was found that the value of density of states calculated from the experimental values of T_0 in the Mott model ($\sim 10^{20} \text{ eV}^{-1} \text{ cm}^{-3}$) were unrealistically low for this type of material. On the other hand T_0 values obtained from the Shklovskii and Efros model gave realistic estimates of the effective radius ($\sim 2.4 \times 10^{-10} \text{ m}$). This suggested that the Shklovskii and Efros model was more applicable for these materials.

Further analysis was carried out to obtain the value of the exponent p in the resistivity expression (equation 5.7) as proposed by Zabrodskii. This analysis showed that the Shklovskii and Efros variable range hopping model could be applied satisfactorily up to a temperature of $\sim 300\text{K}$ (value of $p \sim 0.4 - 0.7$) but then a change in the conduction mechanism was observed. Above $\sim 300\text{K}$ the value p was much higher around 1.5 to 2 which did not correspond to any known conduction mechanism. Nevertheless, $R-T$ data above 300K were fitted to the nearest neighbour hopping model and this resulted in an excellent fit. Furthermore, the corresponding activation energies ($\sim 320\text{ meV}$) were in good agreement with those published by other researchers. It was concluded that a change in conduction mechanism occurred around 300K , although possible causes remained largely unexplained.

When a polaronic model for high temperatures ($T > 300\text{K}$) was considered the pre-exponential term C_0 in the resistivity expression varied in the same way as the resistivity with both compositions and sintering temperatures. This was probably linked to the ratio of Mn^{3+} to Mn^{4+} in the octahedral sites of the crystal structure. The results also implied that the oxygen stoichiometry influenced the Mn^{3+} to Mn^{4+} ratio and hence the resistivity of the material. This work demonstrated that the resistivity of the nickel manganate system could be controlled and manipulated by changing either the nickel to manganese ratio or the sintering temperature. Resistivities as low as $\sim 1.2\text{ Kohm} - \text{cm}$ and as high as $\sim 30\text{ Kohm} - \text{cm}$ were obtained by varying the parameters. However, in all cases the B values were in the range of that needed to produce commercial devices ($2800 - 4820\text{ K}$).

In the next chapter, electrical and structural characterisation results of sputtered thin films produced from target made with N2/0.71 material will be presented and discussed.

5.5 REFERENCES

- [1]. Schmidt, R. (2001), Diploma Thesis, *Screen printing of co-precipitated $NiMn_2O_4$ for production of NTC thermistors*. In Institut für Technische Physik, Friedrich-Alexander Universität, Nürnberg.
- [2]. Brabers, V.A.M., Terhell, J.C.J.M. *Electrical conductivity and cation valencies in nickel manganite*, (1982) *Physica Status Solidii (A)*, **69**, 325-332.
- [3]. Sun, Y., Xu, X., Zhang, Y. *Variable-range hopping of small polarons in mixed-valence manganites*, (2000) *Journal of physics: Condensed matters*, **12**, 10475-10480.
- [4]. McKelvey, J.P. (1966) *Solid State and Semiconductor Physics*. Harper&Row, New York.
- [5]. Mansfield, R. (1991) *Hopping Transport in Solids*. Elsevier Science Publishers.
- [6]. Zabrodskii, A.G. *Electrical conductivity of heavily doped compensated n-type germanium produced by neutron doping*, (1980) *Soviet Physics Semiconductors*, **14**, 670-676.
- [7]. Bera, S.K., Chaudhuri, S., Pal, A.K. *Electron transport properties of CdTe nanocrystals in $SiO_2/CdTe/SiO_2$ thin film structures*, (2002) *Thin Solid Films*, **415**, 68-77.
- [8]. Rousset, A., Legros, R., Lagrange, A. *Recent progress in the fabrication of ceramic negative temperature coefficient thermistors*, (1994) *Journal of European Ceramic Society*, **13**, 185-195.
- [9]. Macklen, E.D. (1979) *Thermistors*. Electrochemical Publications, Glasgow.
- [10]. Fritsch, S., Sarrias, J., Brieu, M., Couderc, J.J., Baudour, J.L., Snoeck, E., Rousset, A. *Correlation between the structure, the microstructure and the electrical properties of nickel manganite negative temperature coefficient (NTC) thermistors*, (1998) *Solid State Ionics*, **109**, 229-237.
- [11]. Laberty, C., Pielaszek, J., Alphonse, P., Rousset, A. *Characterization of nonstoichiometric nickel manganite spinels $Ni_xMn_{3-x}O_{4+\delta}$ by temperature programmed reduction*, (1998) *Solid State Ionics*, **110**, 293-302.

Structural and Electrical Properties of $Ni_xMn_{3-x}O_{4+\delta}$ Thin Films

6.1 INTRODUCTION

The previous chapter investigated the properties of the nickel manganese oxide system in bulk form. In the present chapter, the properties of $Ni_xMn_{3-x}O_{4+\delta}$ thin films sputtered from a target with a nickel to manganese ratio of 1:1.22 (N2/0.71 material system as referred to in chapter 4) are discussed. The first part of the chapter deals with the microstructure and phase purity of the as-deposited films and the effect of post deposition annealing on the structural properties. The effect of the substrate temperature during sputtering on the structure of the films has also been investigated and discussed. In the second part the electrical properties of the films deposited in different oxygen partial pressures and the effect of annealing in different ambients are presented. Finally, the electrical data were fitted to various electron hopping conduction models. In the literature, there is still uncertainty as to the exact charge transport mechanism for this type of material and hence an attempt has been made to evaluate these models and to select the one most consistent with the data obtained from experiments.

6.2 EXPERIMENTAL

6.2.1 FILM DEPOSITION AND HEAT TREATMENT

Films were produced using a custom built on-axis rf magnetron sputtering system which has been described in considerable detail in chapter 3. They were deposited in pure argon on <100> silicon substrates (20 x 20 mm) which were cleaned by immersing in commercial grade hydrofluoric acid for 10 minutes followed by washing in de-ionised water. The substrates were hydrophobic and did not need drying before loading in the sputtering chamber. Films were deposited using different substrate temperatures (35°C, 100°C, 200°C and 250°C) to allow study of the microstructure and the phase purity. These films were then annealed in air at temperatures ranging from 450°C upto 900°C in a Carbolite air oven fitted with an Eurotherm 810 programmable temperature controller. Subsequently the films were quench cooled from the annealing temperature to room temperature.

Films used for resistance versus temperature measurements were deposited on a thermally grown oxide layer on <100> silicon. The silicon substrates were first cleaned using de-ionised water and then dried using nitrogen gas. They were then placed on sheets of zirconia and heated at 1150°C for 15 hours in a Lenton air oven fitted with an Eurotherm 810 programmable temperature controller. The ramp rate during heating up was 4°C min⁻¹ and while cooling down it was ~ 5°C min⁻¹. After this process, the substrates were again cleaned in de-ionised water and dried using nitrogen gas, prior to loading in the sputtering chamber. The films were deposited in different argon/oxygen containing ambients (oxygen percentage = 0.3, 1, 2.5, 5, 7.5, 10, 12.5, 15) at a substrate temperature of 35°C.

One set of films, deposited on silicon with a thermally grown oxide layer for studying the electrical properties, was annealed at 800°C for 1 hour in a Lenton air oven, before being quench cooled to room temperature. Another set was annealed at 800°C in

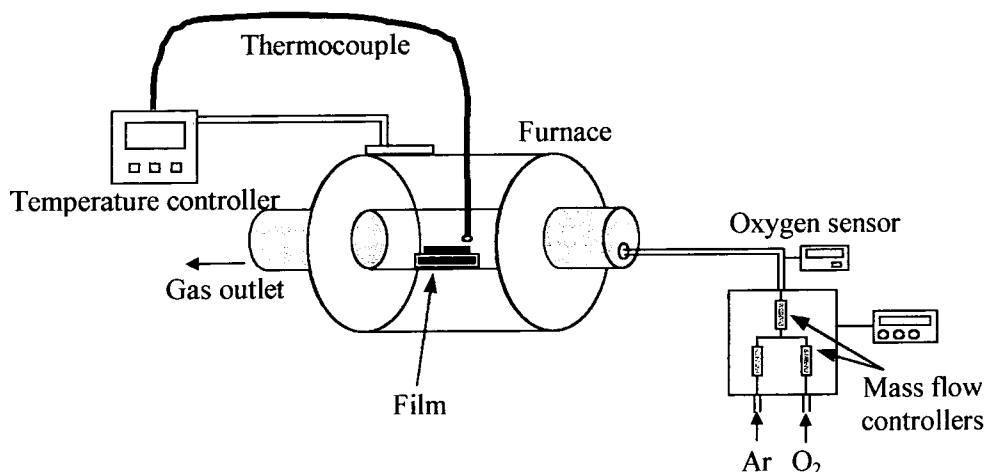


Figure 6.1 Schematic representation of the arrangement used for annealing films in an ambient similar to that during sputtering

ambients with an argon/oxygen ratio similar to the one used during sputtering. The experimental setup of this process is shown in figure 6.1. Films were placed in a quartz tube which had one end connected to the gas mixing system of the sputtering set-up, which was described in chapter 3. The other end of the tube was open to allow a continuous flow of gas. A thermocouple was placed very close to the film so that an accurate annealing temperature could be maintained. After 1 hour, the tube was taken out of the furnace for quench cooling while the gas flow was continued. The oxygen content in the gas was checked using an in-line Anacon gas sensor.

6.2.2 ATOMIC FORCE MICROSCOPY

Atomic force microscopes (AFM) have been widely used in various fields to study surfaces of thick and thin films, semiconductors, biological membranes, plastics, ceramics, etc. AFM produces atomic resolution images by scanning a tip, placed on the end of a cantilever, over a surface. The position of the tip changes according to the topograph of the surface and this change in vertical position results in a variation of force, which is recorded by a detecting system. The first AFM for investigating surfaces was made by Gerd Binnig and Christoph Gerber [1] in 1986, using a diamond glued to a strip of gold foil. AFM can be operated in two modes, namely the contact mode where the tip touches the surface under investigation and the non-contact mode where the tip is separated from the surface by a very small distance ($\sim 10 - 50$ nm). In the contact mode the resolution is low due to the large forces and the relatively large area of contact [2] and Ohnesorge et. al. [3] realised that as a consequence atomic resolution cannot be achieved using this mode.

Martin et. al. [4] invented the non-contact AFM with a highly sensitive detecting system which was able to record the very small attractive forces between the tip and the sample. The small changes in force build up the topographic image of the surface. Atomic resolution images of *InP* were achieved by carrying out the microscopy in ultra high vacuum. In the present study an ultra high vacuum Omicron needle sensor type non-contact AFM was used to investigate the topograph of the films. A detailed review of the working principles of such microscope has been given by Nishi et. al. [5] and hence will not be discussed here.

6.2.3 X-RAY DIFFRACTION

Diffraction of x-rays by matter makes it an useful tool for studying various properties of scientifically important materials. The general principles of the x-ray diffraction theory can be found in the literature [6] and are not discussed here. In the present study the measurements were carried out using the Bragg-Brentano configuration where the source, detector and the normal to the sample surface all lie in the same plane. The instrument used was a commercial Siemens D5000 diffractometer with a copper anode, which gives $Cu_{k\alpha}$ radiation with a wavelength of 1.54056 Å. The films were attached to the sample holders with blue tac. The measurements were carried out in a range of 25 to 60 degrees (2θ). All the scans were done with a step size of 0.02 degrees per step and the data was recorded for 11 seconds per step to obtain good signal to noise ratio.

6.2.4 THICKNESS MEASUREMENT

Film thickness was measured using an Alpha step profilometer. A stylus moved across the sample surface and the instrument recorded changes in vertical displacement caused by the roughness of the surface. The films were scratched with a scalpel blade down to the substrate and the height of the step which resulted was measured using the profilometer. Measurements were taken at three different positions and the average was used as the thickness of the film.

6.2.5 CONTACT FABRICATION

Aluminium contacts for $R-T$ measurements were deposited by vacuum evaporation. Films were covered with a copper mask with a pair of 1 mm diameter holes located 9 mm apart. Aluminium wire cleaned using isopropyl alcohol to remove any surface

contamination, was placed in a tungsten filament. The assembly was loaded into the evaporation chamber which was then pumped down to $\sim 10^{-4}$ mbar using a diffusion pump. The current to the filament was ramped up slowly to 35 amps and the evaporation was carried out for 2 minutes. The system was allowed to cool down for 30 minutes while pumping continued. Immediately after taking the film out of the evaporation chamber the contacts were covered with conductive silver paint to prevent any oxidation. The silver paint was dried overnight in a drying oven at $\sim 70^\circ\text{C}$.

6.2.6 R-T MEASUREMENT SYSTEM

Resistance versus temperature ($R-T$) measurements were undertaken in air over a temperature range of 20°C to 200°C . The experimental set up is shown in figure 6.2.

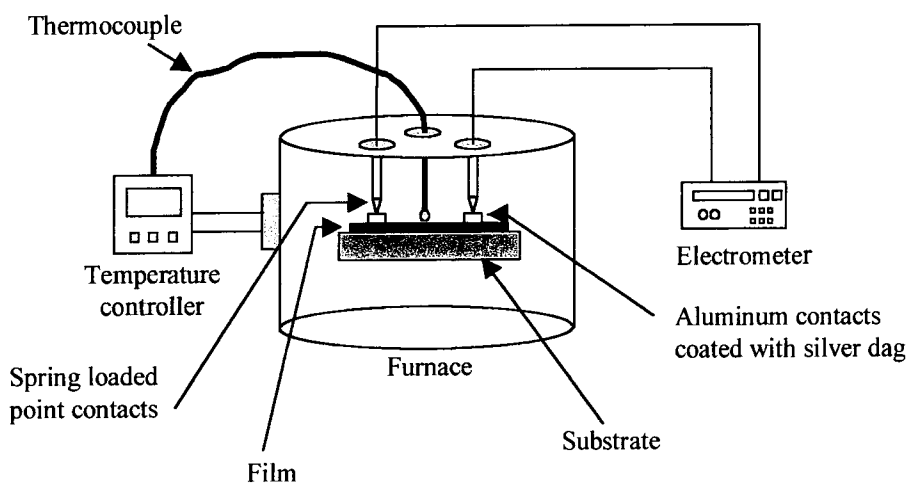


Figure 6.2 Schematic representation of the experimental setup for resistance versus temperature measurements of thin films

Films were placed in a special jig and spring loaded pins were dropped onto the evaporated aluminium contacts. The assembly was then loaded into a small furnace with the controlling thermocouple positioned next to the film. The temperature of the furnace

was regulated using a Microcal temperature controller. Enamelled copper wires were crimped onto the point contacts and attached to a Keithley 617 electrometer to enable measurement of resistance. The temperature was ramped up to the chosen value and allowed to stabilise for 30 minutes before the resistance was measured.

6.3 STRUCTURAL CHARACTERISATION

6.3.1 CRYSTAL STRUCTURE

As discussed in chapter 4, the target had a monophasic cubic spinel structure. The aim was to produce thin films with a similar structure so as to investigate the electrical properties of comparable materials. Films produced at 35°C substrate temperature in an argon ambient showed poor crystallinity with only one broad peak in the x-ray diffraction results. This led to the investigation of the effect of different substrate temperatures on the crystal structure of the films. X-ray diffraction results of as-deposited films produced at different substrate temperatures in a pure argon ambient are shown in figure 6.3. The other peak observed around 35°C was from the substrate, as

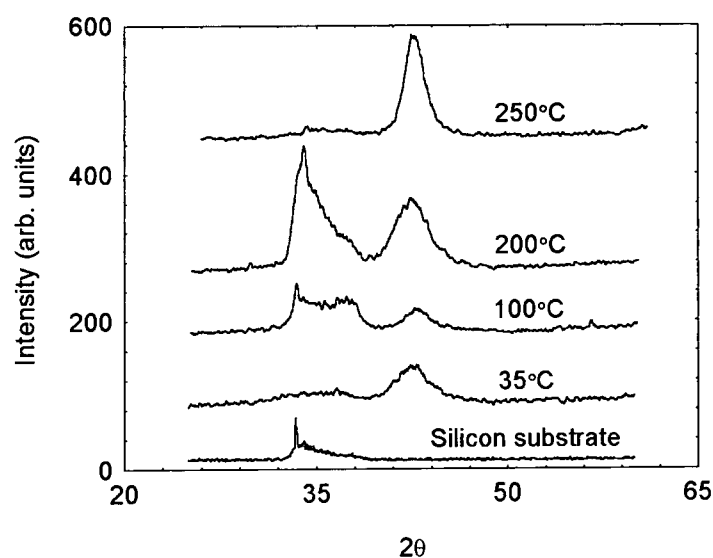


Figure 6.3 XRD traces of as-deposited films deposited at four different substrate temperatures and of a bare silicon substrate

confirmed by x-ray diffraction of a bare substrate which is also shown in figure 6.3. It could be seen that films deposited at all the different substrate temperatures showed a peak in a similar position to that of the (400) reflection ($2\theta \sim 43^\circ$) of nickel manganate, but the shape of the peak was broad and ill defined. This peak became marginally sharper with increasing substrate temperature but it remained much broader than the one observed for polycrystalline powders. The line broadening observed was possibly due to the small grain sizes, as illustrated in section 6.3.2. Such behaviour was also reported by Fau et. al. [7] who deposited similar films using rf magnetron sputtering and found that films deposited in pure argon or high oxygen ($>0.17\%$) containing environments showed poor crystallinity.

The above results prompted a study into the effect of post deposition annealing on the crystallinity of the films. The films were annealed in air from 400°C upto 900°C at intervals of 50°C , followed by quenching to room temperature. The XRD pattern of films deposited at all four different substrate temperatures and annealed at 800°C are

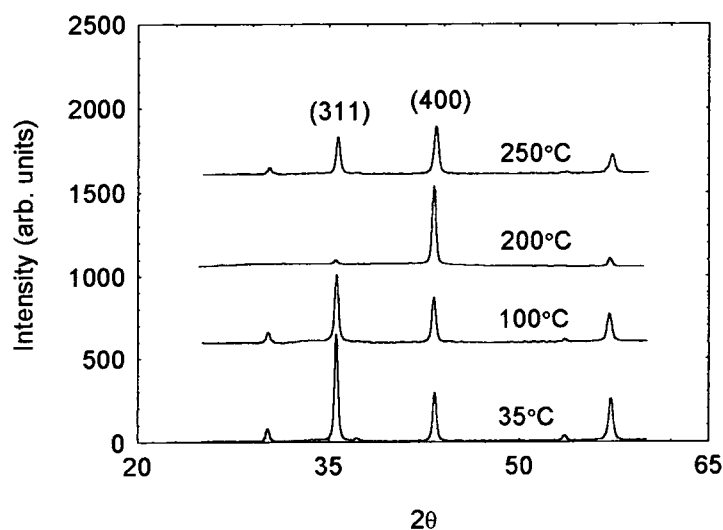


Figure 6.4 XRD traces of films deposited at four different substrate temperatures and annealed at 800°C

shown in figure 6.4. The emergence of a XRD pattern with sharper peaks, which could be attributed to the spinel phase, was observed for films deposited at substrate temperatures up to 200°C and annealed at 750°C. This transition for films deposited with substrate temperature at 250°C was not observed until an annealing temperature of 800°C.

The peak widths of these films reduced noticeably and became much better defined after annealing at 750°C. This was checked by fitting a pseudo-Voigt [8] function to the peaks and measuring the full width at half maximum (FWHM). The peaks show some degree of broadening for films annealed at 900°C. This corresponds well with the temperature (~880°C) at which nickel oxide segregates out of monophasic nickel manganate as discussed in chapter 2 [9]. Figure 6.5 compares the (400) peak shapes as

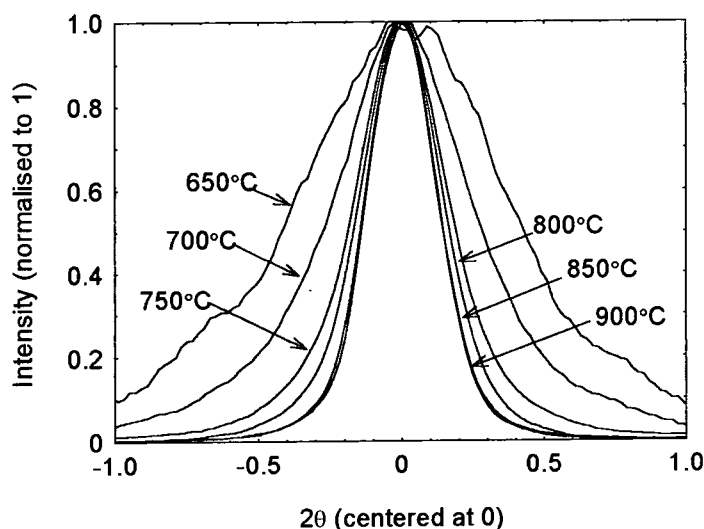


Figure 6.5 Comparison of the normalised (400) peak profile of films deposited at 200°C and annealed at temperatures from 650°C up to 900°C

a function of annealing temperature for the films deposited with a substrate temperature of 200°C. The peaks were centred at zero and the intensity was normalised to one. This

reduced the effects on the peak positions caused by any small change in lattice parameter.

The width of diffraction peaks can be affected by the grain sizes of the material. This effect can be quantified by the Scherrer equation [10]

$$\Delta_{size}(2\theta) = \frac{\kappa\lambda}{D \cos(\theta_B)} \quad (6.1)$$

where Δ_{size} is the width of the peak, λ is the wavelength, D is the grain size perpendicular to the surface, θ_B is the Bragg angle and κ a constant depending on the line shape profile and its value is very close to unity. Broadening of the peak can also be caused by micro strain ε within the crystal from Δd . The effect of strain on the diffraction peaks can be expressed as

$$\Delta_{strain}(2\theta) = 2\varepsilon \tan(\theta_B) \quad (6.2)$$

Williamson-Hall analysis [10,11], which allows calculation of the lattice strain dispersion and the grain size separately was carried out on all the films. The effect of strain and the grain size on the diffraction peaks can be expressed as a sum of equation (6.1) and (6.2)

$$\Delta_{total}(2\theta) = \frac{\lambda}{D \cos(\theta_B)} + 2\varepsilon \tan(\theta_B) \quad (6.3)$$

Equation (6.3) assuming $\kappa = 1$ can be rearranged and written as

$$\Delta(2\theta) \cos(\theta_B) = \frac{\lambda}{D} + 2\varepsilon \sin(\theta_B) \quad (6.4)$$

A plot of $2\sin\theta_B$ against the product of width of the peak (FWHM)* $\cos\theta_B$ yields a straight line, with the slope giving an estimate of strain and the intercept indicating the grain size. The analysis showed that the net contribution from the lattice strain dispersion ($\varepsilon=\Delta d/d$) was negligible as shown in figure 6.6 and that the dominant factor in determining the peak shape was the size of the grains. In the absence of significant

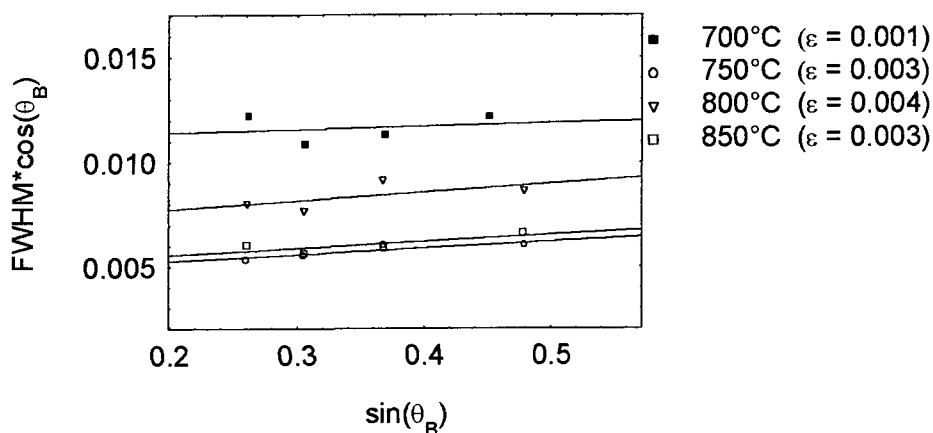


Figure 6.6 Williamson – Hall plot of films deposited at 100°C annealed at different temperatures. The strain values obtained are shown inside brackets

strain, grain size may be estimated using the Scherrer equation (equation. 6.1). The analysis was carried out on the (400) reflection in the XRD profile and the results are shown in table 6.1. These confirmed the transition from a small grain size for films annealed at 700°C to a larger grain size for films annealed at 750°C. After annealing at 850°C the peak widths were similar for most of the films, with the exception of the

Substrate temperature	Grain Size from Scherrer Analysis on (400) reflection (nm)			
	Annealed at 700°C	Annealed at 750°C	Annealed at 800°C	Annealed at 850°C
35°C	34.2	47.1	55.0	57.4
100°C	28.1	50.7	46.7	52.0
200°C	36.5	59.3	67.0	86.5
250°C	26.0	28.7	45.2	55.2

Table 6.1 Effect of substrate and annealing temperature on grain size obtained from Scherrer analysis of (400) XRD peak

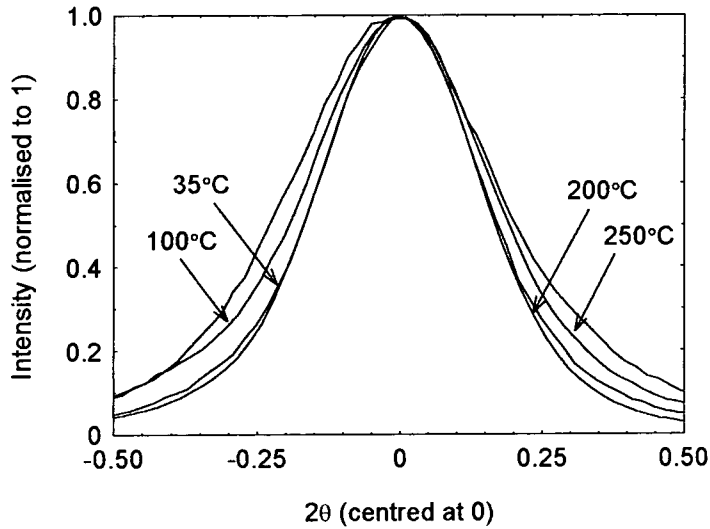


Figure 6.7 Comparison of the normalised (400) XRD peak of films deposited at four different substrate temperatures and annealed at 850°C

film deposited at 200°C which had a narrower shape, implying a larger grain size (figure 6.7). The grain sizes found from Scherrer analysis of the films deposited at higher temperatures (200°C and 250°C) was very similar to those found using AFM (see later in section 6.3.2).

A pseudo-Voigt function was fitted to all the diffraction peaks to determine the angle and hence the interplanar spacing d_{hkl} . Lattice parameters were then calculated using the following equation, which is valid for cubic structured materials

$$d_{(hkl)} = \frac{a}{\sqrt{h^2 + k^2 + l^2}} \quad (6.5)$$

where a is the lattice parameter, h , k and l are the Miller indices and $d = \lambda/2\sin\theta$. In all cases the lattice parameters of the films were lower than that of the bulk target material ($a_{target} = 8.42135 \pm 0.00027 \text{ \AA}$). Films deposited at substrate temperatures of 35°C, 200°C and 250°C all had similar value of a ($a_{average} = 8.364089 \pm 0.008054 \text{ \AA}$) but

films grown at a substrate temperature of 100°C had a higher value of a ($a_{100^\circ\text{C}} = 8.3876 \pm 0.00249 \text{ \AA}$). For a given substrate temperature, the lattice parameter was largely independent of the annealing temperature in the range 750°C to 850°C, where nickel manganate exists as a single phase. The results of section 4.3.1 suggested that the films were nickel rich compared to the target, as the lattice parameter of the spinel phase was seen to be dependent on the nickel content. However EDAX analysis of the films did not show any significant difference in the elemental ratios between the target and the films. Therefore this discrepancy may be attributed to the lack of oxygen in the films. The ionic radius of O^{2-} (1.32 Å) is larger than that of Mn^{3+} (0.66 Å) [12], which would be produced to maintain charge neutrality according to equation (2.5), resulting in smaller lattice parameter. Similar relationship was also observed by Boucher et. al. [13] who proposed a similar relationship between the lattice parameter and the inversion parameter (equation (2.7)), which has been discussed in chapter 2. However the relationship was derived for stoichiometric nickel manganate ($NiMn_2O_4$) and hence cannot be used here to determine the inversion parameter.

This study also investigates the degree of the preferred orientation, which in here is quantified as the ratio of the I_{311} to I_{400} reflection in the diffraction pattern. In a powder diffraction pattern of randomly orientated nickel manganate, the (311) reflection is the most intense and the intensity ratio I_{311}/I_{400} is 4.8. In the case of thin films, irrespective of the substrate temperature, there was a preferred orientation towards the $\langle 100 \rangle$ direction. This was expected as the films were deposited on $\langle 100 \rangle$ silicon substrates. The degree of preferred orientation increased with increasing substrate temperature as shown in figure 6.8 reaching a maximum for a substrate temperature of 200°C and

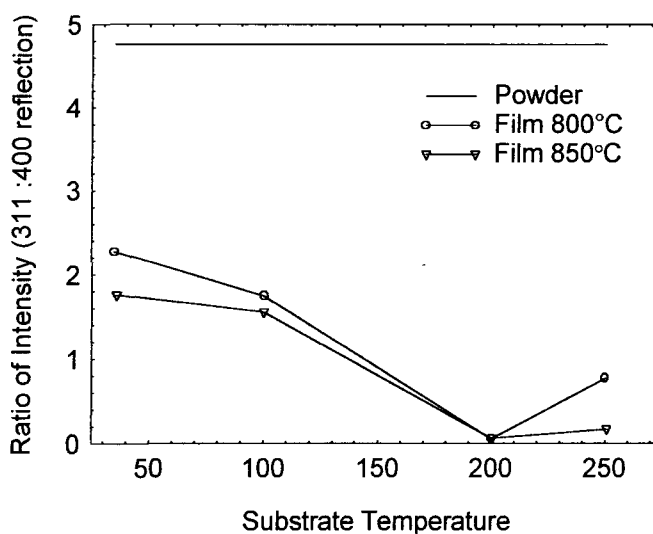


Figure 6.8 Variation in preferred orientation ((311):(400) peak intensity ratio) with substrate temperature for films annealed at 800°C and 850°C

relaxing again slightly at 250°C. This general trend of the films deposited at 200°C exhibiting the greatest degree of preferential orientation was observed for all annealing temperatures, although after annealing at 850°C the films deposited at 250°C showed a similar value of preferred orientation to the ones deposited at 200°C.

6.3.2 MICROSTRUCTURE

The microstructure of the target material was discussed in the chapter 4. A description of the target preparation process was also outlined in chapter 4. The microstructure of the films both in the as-deposited state and after annealing at 800°C were characterised using AFM and the results were used to study the effect of the post deposition annealing process.

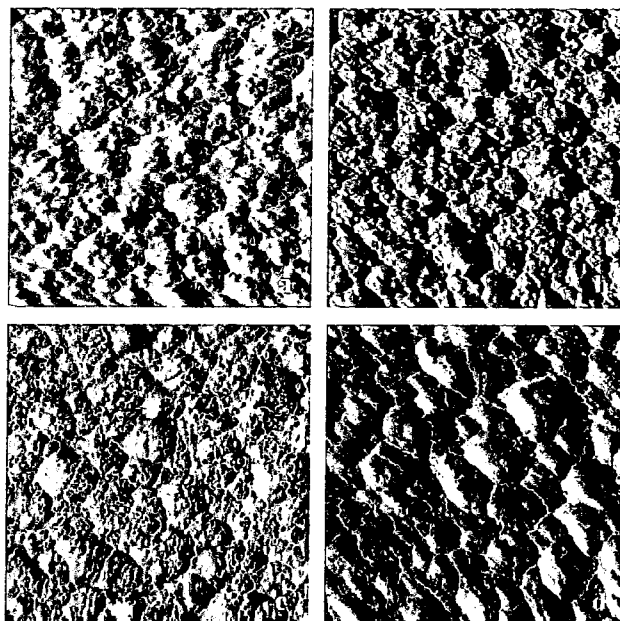


Figure 6.9 AFM images (1200 x 1200 nm) of as-deposited films, grown at substrate temperatures of (a) 35°C, (b) 100°C, (c) 200°C and (d) 250°C

The AFM images of as-deposited layers grown at all four substrate temperatures are shown in figure 6.9. The microstructure of these films was significantly different from the target material and could be described as an agglomeration of very small grains forming clusters. The clusters in the films deposited at 35°C and 100°C look similar but there was a noticeable change in their appearance for the layer deposited at 200°C, where the clusters looked different and inhomogeneous. In figure 6.9 (d) (substrate temperature 250°C) the appearance of the surface was again different and the clusters were marginally bigger than those of the film deposited at 200°C.

Figure 6.10 shows the AFM images of films annealed at 800°C and subsequently quench cooled to room temperature. The most significant changes were observed in the

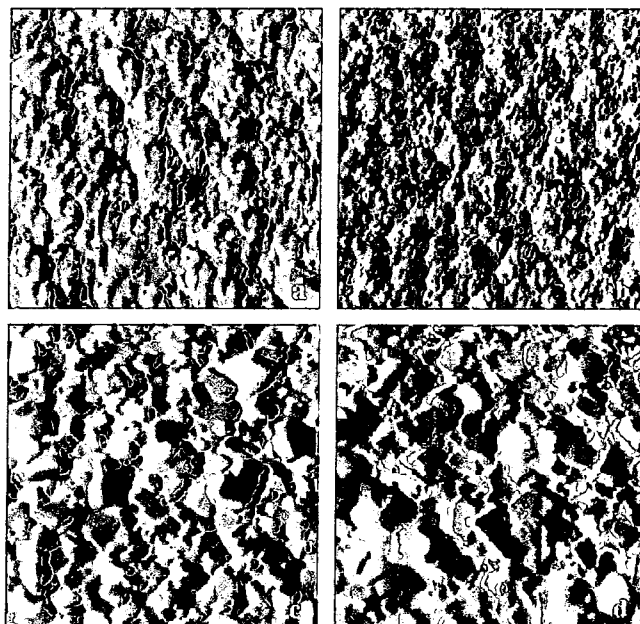


Figure 6.10 AFM images (1200 x 1200 nm) of films deposited at substrate temperatures of (a) 35°C, (b) 100°C, (c) 200°C and (d) 250°C, after annealing at 800°C for 1 hour in air

films deposited at substrate temperatures of 200°C and 250°C (figures 6.10 (c) and 6.10 (d)), which showed a comparatively ordered and well defined grain structure. The grain sizes of the films deposited at substrate temperatures of 200°C and 250°C, were in the order of ~35 nm, still much smaller than the target grain sizes but larger than in films grown at lower substrate temperatures. All films showed some ordering after annealing. The surface roughness of the films in the as-deposited state was about 5-10 nm (Rms). After annealing the roughness of the films deposited at a substrate temperature of 250°C had increased to about 15 nm (Rms), but the others did not show much change. The grain size distributions of the annealed films deposited at 200°C and 250°C are shown in figure 6.11. Figures 6.11 (a) and (c) show skeletal images of the

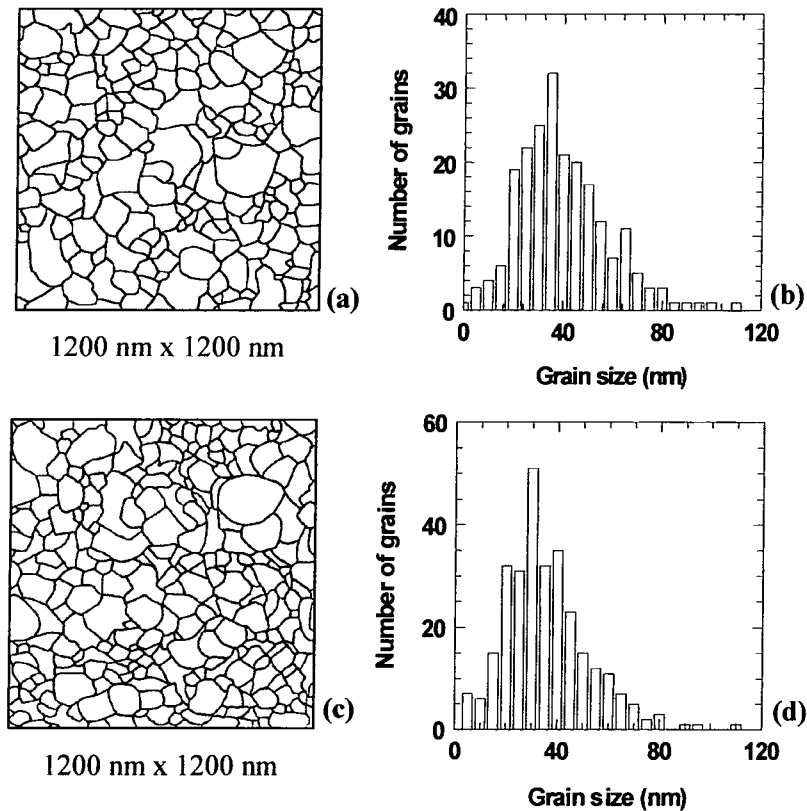


Figure 6.11 Grain sizes of annealed films (a) skeletal image of the microstructure of a film deposited at 200°C, (b) corresponding grain size distribution, (c) skeletal image of the microstructure of a film deposited at 250°C and (d) corresponding grain size distribution

microstructure, which depict the grain boundaries. The grain sizes were determined using CGS2 software [14]. It was difficult to distinguish grains for the films deposited at the lower substrate temperatures as the grain structure was not very well defined and hence no attempt was made to determine the grain size distribution. Figures 6.11 (b) and (d) show that the grain sizes of the films grown at 200 and 250°C did not vary significantly from each other.

Compared to the films deposited in pure argon, films deposited in oxygen containing ambients showed a structure with grains that differed slightly in shape. The dependence of the grain growth on temperature was still observed. Annealed films exhibited more

ordering irrespective of the substrate temperature. No significant changes were observed in the microstructure for films deposited in different oxygen percentages

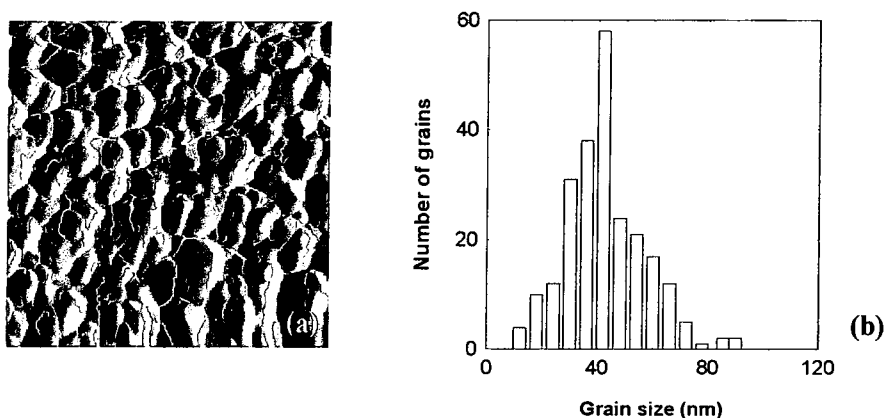


Figure 6.12 Annealed film, deposited at 200°C substrate temperature and in an argon/oxygen (12.5% oxygen) ambient (a) AFM micrograph (1200 x 1200 nm) and (b) grain size distribution

during sputtering. Figure 6.12 (a) shows the structure of a film deposited with the substrate at 200°C, in a sputtering ambient containing 12.5% oxygen. The grain size distribution is shown in figure 6.12 (b), which indicated that the grain sizes were in the order of ~30–90 nm, similar to those of the films deposited at the same substrate temperature in a pure argon environment. The microstructure of as-deposited films produced at 35°C in oxygen/argon environments was again found to be similar to those deposited in argon at the same substrate temperature. Baliga et. al. [15] reported difficulties in producing films with an ordered microstructure in high oxygen containing environments (oxygen > 0.1%), which were not encountered in this work. The microstructures of the films produced by Baliga et. al. in high oxygen containing environments were described as ‘cauliflower type’ and also exhibited poor crystallinity. However, they did not use post deposition annealing at 800°C, as in this study. The structure presented by Baliga et. al. was quite different from the ones produced in this study.

6.4 ELECTRICAL CHARACTERISATION

The electrical characteristics of the thin films were measured to investigate the NTCR characteristics and the charge transport of the material. Films were sputtered in various ambients to study the effect of the sputtering environment and the influence of the post deposition annealing process on the electrical properties was also investigated.

6.4.1 RESISTIVITY

The resistivity of the films at 50°C ($\rho_{(50)}$) was calculated by measuring the film thickness and using the following equation

$$\rho = \frac{RA}{l} \quad (6.6)$$

where ρ is the resistivity, R is the resistance at 50°C, A is the product of the diameter of the contact and the thickness of the film and l is the distance between the contacts. The resistivities of the films are shown in figure 6.13. Following annealing in either air or in argon/oxygen mixed ambients, $\rho_{(50)}$ was nearly an order of magnitude lower than that of the target material ($\rho_{(50)Target} \sim 1.3$ Kohm-cm). The as-deposited films grown in lower oxygen percentages had higher resistivities ($\rho_{(2.5\% \text{ Oxygen})} = 2.9$ Kohm-cm), although the as-deposited resistivity decreased with increasing oxygen percentage and for films grown in 12.5% and 15% oxygen, resistivity had become comparable to that of the annealed films. Films annealed at 800°C in the same ambient as that used during sputtering, showed relatively little variation in resistivity with changing deposition and

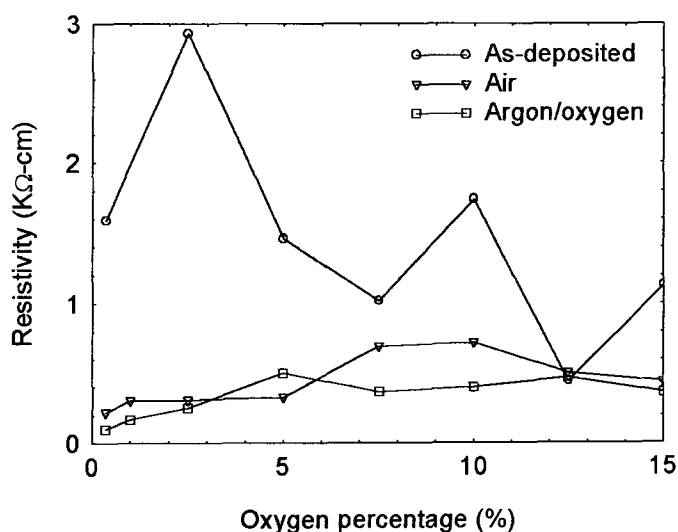


Figure 6.13 Resistivity of films at 50°C in as-deposited state and after annealing in air and oxygen/argon ambients

annealing environments, only increasing by a factor of ~ 2 as the oxygen fraction was increased from 0 to 15%. Dannenberg et. al. [16] reported similar dependence of resistivity on the oxygen content (oxygen 0 to 10%) in the environment during sputtering of nickel manganate doped with cobalt for as-deposited films. Their results showed that the resistivity of the films sputtered at 10% oxygen was about 0.075 Kohm-cm while the resistivity of films deposited at 0% oxygen was around 2 Kohm-cm, not dissimilar to the values found in the present study (for ambients containing oxygen), despite the fact that their films were doped with cobalt.

Fau et. al. [7] also deposited stoichiometric nickel manganate using rf magnetron sputtering, although the oxygen levels (0 – 0.24%) used in the deposition ambients were lower than those used in this study. The resistivity of the films deposited in those oxygen containing environments was quite high (resistivity at $\sim 50^\circ\text{C}$ was 1.8 Kohm-cm for films deposited at 0.17% oxygen), in fact higher than their target material. This value of resistivity was similar to that found for films deposited at 0.3% oxygen ambient in this study. They, like Baliga et. al. did not use any post deposition annealing.

6.4.2 CHARGE TRANSPORT PROPERTIES

The R - T data for the temperature range of 20°C upto 200°C were fitted to the nearest neighbour hopping model (both with and without temperature dependent pre-exponential term) and the two variable range hopping models proposed by Mott and by Shklovskii and Efros, which were discussed in chapter 2. The experimental data of films deposited in 5% oxygen and subsequently annealed in air at 800°C, were fitted to all three models, results of which are shown in figure 6.14. It can be seen that the data statistically fit all the models quite well and hence it was difficult to decide which model was most applicable to explain the charge transport mechanism of these films. The T_0 for the Mott model was found to be 1.98×10^9 K whereas the T_0 for the Shklovskii and Efros model was 2.47×10^5 K. The activation energy from the nearest neighbouring

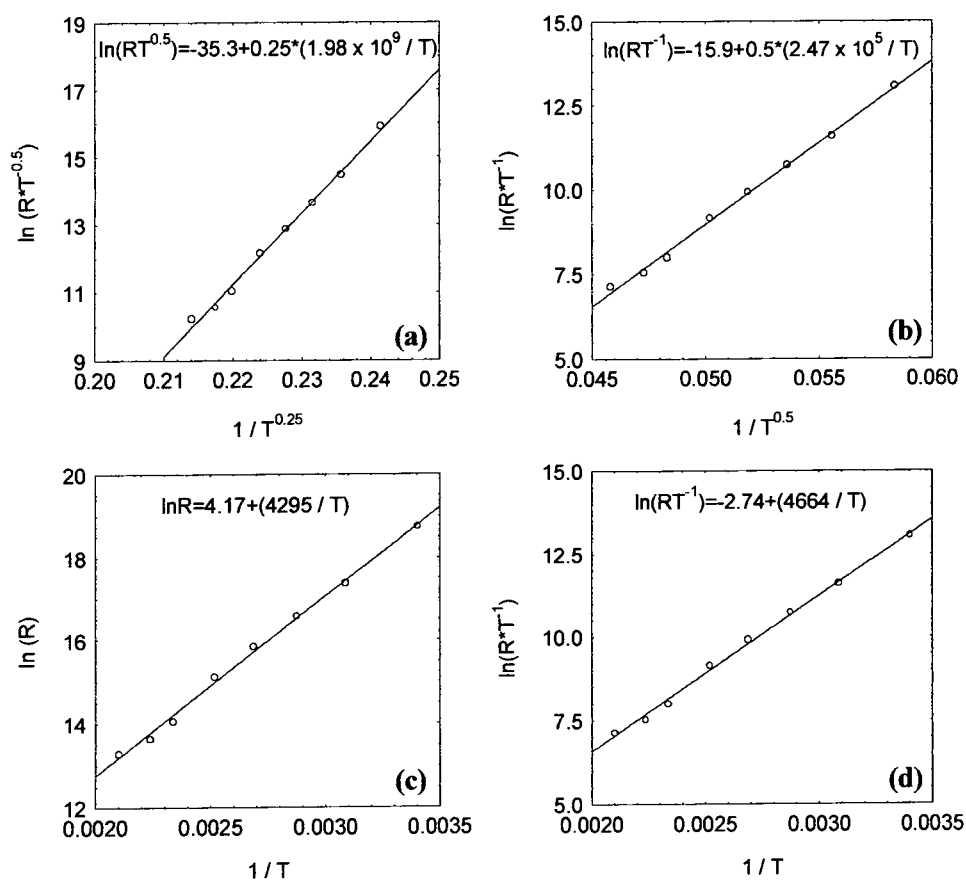


Figure 6.14 R - T data of a film deposited in 5% oxygen and annealed in air at 800°C fitted to (a) Mott model, (b) Shklovskii and Efros model, (c) nearest neighbour hopping (NNH) model and (d) NNH model with T dependent pre-exponential factor

hopping models was found to be ~ 315 meV for the NNH model without the T dependent pre-exponential factor and ~ 402 meV for the NNH model with a temperature dependent pre-exponential factor.

6.4.2.1 MOTT VRH MODEL

In the Mott model the characteristic temperature T_0 is given by

$$T_0 = \frac{\beta}{k_b g(\mu) a^3} \quad (6.7)$$

where β is a constant with a value of 21.2 ± 1.2 . Using the value of T_0 and assuming a

	Value of $g(\mu)$ ($\times 10^{20} \text{ eV}^{-1} \text{ cm}^{-3}$) of films deposited in different oxygen (%) containing ambients							
	0.3	1	2.5	5	7.5	10	12.5	15
As-deposited	4.2	9.2	12.2	8.7	7.5	12.7	9.7	7.7
Annealed in air	8	9.4	5.7	8.3	7.7	4.6	5.5	9.0
Annealed in oxygen /argon	5.5	8.2	13.0	11.7	8.7	6.7	11.7	8.5

Table 6.2 Value of density of states of films estimated from the characteristic temperature T_0 obtained by fitting the R - T data to the Mott model of variable range hopping

to be the Bohr radius of a hydrogen atom, which represents a lower limit on a , the density of states value was found to be in the order of $10^{20} - 10^{21} \text{ eV}^{-1} \text{ cm}^{-3}$, which is very low for this type of material. The values of $g(\mu)$ of all the films in the as-deposited and annealed state are given in table 6.2, which showed that the density of states values are very low irrespective of the deposition and post deposition annealing conditions.

Estimates of the value of density of states could not be found in literature for nickel manganate but manganites with similar resistivities were reported to have density of states of $\sim 10^{23} \text{ eV}^{-1} \text{ cm}^{-3}$ [17]. These results implied that this model did not adequately describe the charge transport of these films and should therefore be discounted.

6.4.2.2 SHKLOVSKII AND EFROS VRH MODEL

The characteristic temperature in the Shklovskii and Efros model is expressed as

$$T_0 = \frac{\beta_1 e^2}{k_b \kappa a} \quad (6.8)$$

where β_1 is a numerical constant equal to 2.8, κ describes the Coulomb interaction between electrons. As discussed in chapter 5 the effective radius can be calculated using T_0 and they are shown in table 6.3.

	Value of $\epsilon_r * a$ ($\times 10^{-10}$ m) of films deposited in different oxygen (%) containing ambients							
	0.3	1	2.5	5	7.5	10	12.5	15
As-deposited	1.58	2.47	2.58	2.18	2.05	2.61	2.88	2.42
Annealed in air	2.13	2.53	1.80	2.00	2.10	1.62	2.11	2.88
Annealed in oxygen /argon	1.78	2.12	2.60	2.45	2.41	2.54	2.51	2.62

Table 6.3 Value of effective radius of films estimated from the characteristic temperature T_0 obtained by fitting the R - T data to the Shklovskii and Efros model of variable range hopping

The T_0 of the film shown in figure 6.13 (b) was $2.47 \times 10^3 \text{ K}$ and the effective radius was found to be $2 \times 10^{-10} \text{ m}$. This value was quite realistic, suggesting that this model was

more consistent with the data than the Mott model. The values of the effective radius of films in the as-deposited state and after annealing in both air and in an oxygen/argon atmosphere are given in table 6.3. All values of the effective radius (range $\sim 1.58 \times 10^{-10}$ to 2.88×10^{-10} m) found for thin films could be considered reasonable and most were similar or marginally lower than that of the target material (2.57×10^{-10} m). Hence the Shklovskii and Efros model can be applied to explain the charge transport properties of the films produced in the different deposition conditions and annealing ambients. Furthermore in the next chapter it will be shown, using scanning tunneling spectroscopy, that the distribution of the density of states of the films was parabolic, which is consistent with the assumptions made in this model.

Figure 6.15 shows the R - T data of films deposited in a 5% oxygen ambient in the as-deposited state, after annealing at 800°C in air and in an oxygen/argon (5% oxygen) mixed ambient. Compared to that of the target, the films annealed in air showed higher values of T_0 whereas the films annealed in argon/oxygen ambient showed very similar

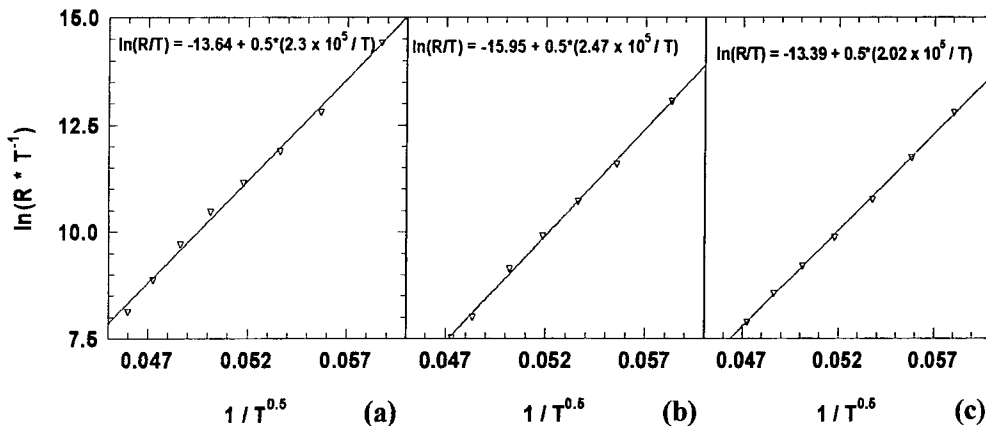


Figure 6.15 R - T data fitted to Shklovskii and Efros model of films deposited at 5% oxygen (a) in as-deposited state, (b) annealed in air at 800°C and (c) annealed in argon/oxygen (5% oxygen) at 800°C

values of T_0 . The variations of the T_0 values for all the different films are shown in figure 6.16 and indicated that the films annealed in ambients similar to those during

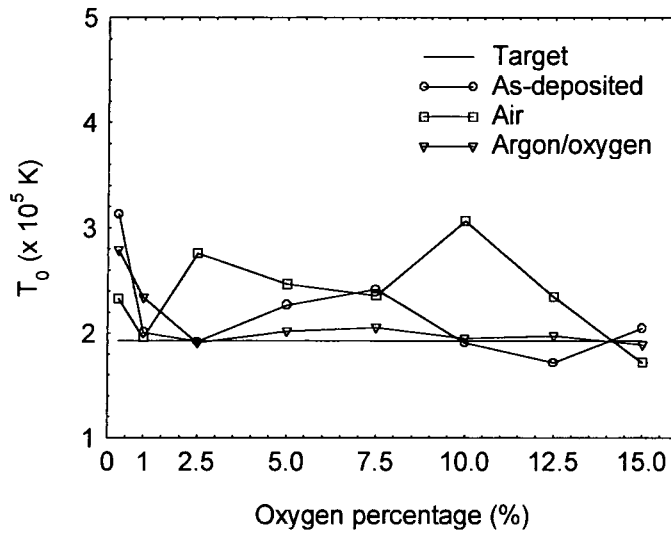


Figure 6.16 Variation of T_0 of films deposited in different oxygen/argon mixed ambients in as-deposited and annealed state

deposition (i.e. oxygen percentage in the ambient) showed least variation and had values of T_0 most similar to that of the target. Interestingly the films deposited in lower oxygen environments (0.3% oxygen) showed higher values of T_0 .

6.4.2.3 NNH MODEL

The R - T data of all the films were also fitted to the nearest neighbour hopping (NNH) model. The characteristic temperature (B -value) was found from the slope of the line fitted to a plot of $\ln R$ vs $1/T$. The values of activation energy, as shown in table 6.4, were then calculated from the B -values and they were similar to those found by other researchers using this model to describe the charge transport in this type of material. Again, the activation energy of the films deposited in a 0.3% oxygen ambient in the as-

deposited state and after annealing in an argon/oxygen (0.3% oxygen) ambient was higher than most of the films.

	Value of ΔE (meV) of films deposited in different oxygen (%) containing ambients							
	0.3	1	2.5	5	7.5	10	12.5	15
As-deposited	422	408	327	362	370	329	312	340
Annealed in air	363	336	399	370	363	422	361	312
Annealed in oxygen /argon	402	368	331	338	341	332	337	327

Table 6.4 Activation energies of films obtained by fitting R - T data to nearest neighbour hopping model

The analysis of the R - T data using the various hopping models showed that the data could apparently be fitted to more than one model, which made it difficult to determine the actual mechanism of charge transport in these thin films. Hence a Zhabrodskii [18] type analysis similar to that carried out for bulk material in the previous chapter was carried out to determine the value of the exponent p in the generalised resistivity expression.

6.4.3 ANALYSIS OF ' p '

As discussed in the chapter 5, this analysis is very sensitive to noise in the data set. In general the R - T characteristics for thin films were more noisy than those for the bulk material and hence in some cases it was difficult to fit a straight line to the plot of $\ln T$ vs $\ln w$, ($w = \{(1/T) * (d \ln R / d T^{-1})\}$). Figure 6.17 shows the results of the analysis carried out for films deposited with 10% oxygen in the sputtering ambient, both in the as-deposited state and after annealing in different conditions. The value of p was 0.52 for

the as-deposited films, 0.74 after annealing in air and 0.64 after annealing in argon/oxygen (10% oxygen). The spread in the values reflected the greater noise level. These values indicated that the conduction mechanism for these films could be described more satisfactorily by the variable range hopping model proposed by

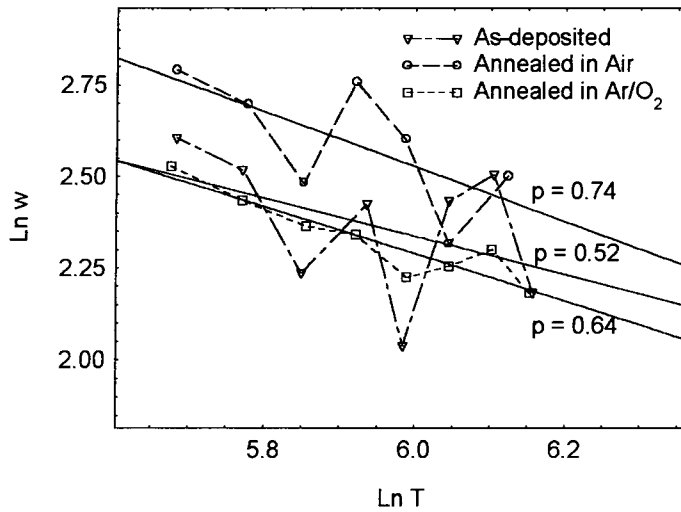


Figure 6.17 Plot of $\ln T$ vs $\ln w$ ($w=(1/T) \cdot (d \ln R / d T^1)$), for films deposited in 10% oxygen ambient, in the as-deposited and annealed states

Shklovskii and Efros ($p = 0.5$). However for films deposited in lower oxygen containing ambients (less than 1% oxygen), the p value was ~ 1 , which suggested that the

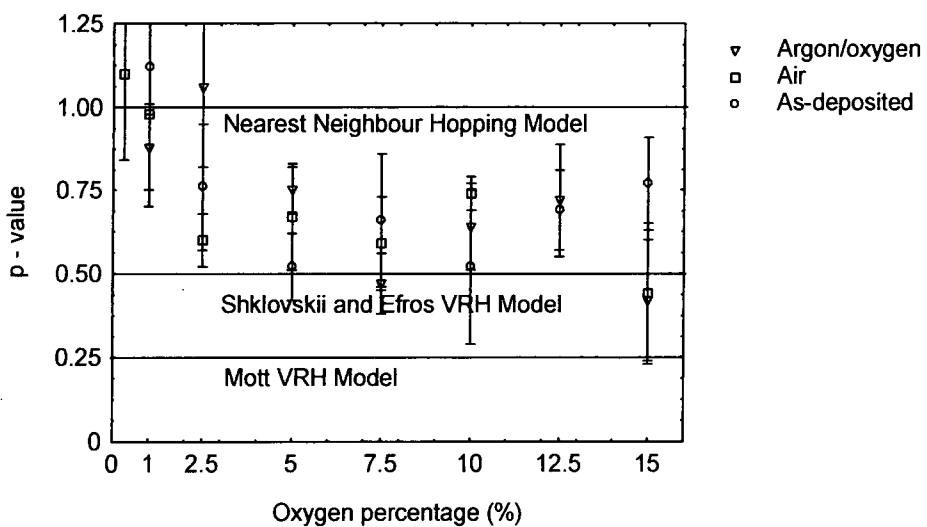


Figure 6.18 Comparison of p values of films, deposited in different conditions, both in as-deposited and annealed states, for the hopping conduction models (the error bars represents the statistical error of the curve fitting)

conduction mechanism could be better described by the nearest neighbour hopping model. The variation of the exponent p for all the films is shown in figure 6.18.

Most of the films deposited in higher oxygen ambients (oxygen >1%) showed values between 0.4 and 0.75. Some films in figure 6.18 possessed values significantly higher than 1, which probably could be attributed to noise in the R - T data, as these values do not correspond to any of the hopping models. Interestingly, the films which had p values higher than 1 in most cases also showed high values of T_0 in the VRH model and higher activation energy values in the NNH model.

For the target material, the value of p was found to be around 0.62 as mentioned in section 5.3.3 and it was assumed therefore that the charge transport was best described by the Shklovskii and Efros variable range hopping model. As previously discussed a change in the p value was noticeable for the target ~ 300 K and for most of the bulk material analysed. However, the slope found for the thin films in similar temperature regimes was very different. Figure 6.19 shows the plot of $\ln T$ vs $\ln w$ of the target and

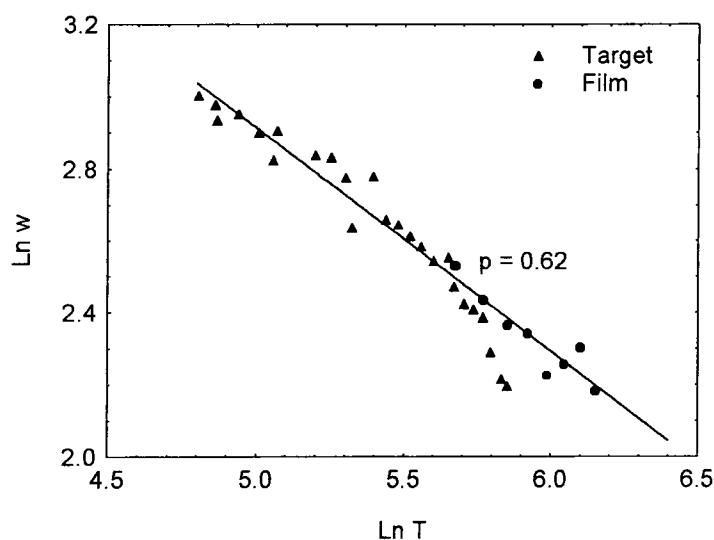


Figure 6.19 Plot of $\ln T$ vs $\ln w$ comparing the target material with an annealed thin film deposited in 10% oxygen

an annealed film deposited at 10% oxygen. It appears that the thin films had a similar slope to that of the target material for temperatures $< 300K$, but they did not show any change of the p value as seen for the bulk at least in the temperature range that was investigated. The characteristic temperature T_0 of the films was similar to that of the target material hence it is proposed that the same charge transport model as for the target material would be applicable to thin films. However it is possible that the transport in these films may well be in the regime where it was a mixture of both mechanisms, with the variable range hopping dominant over the nearest neighbour hopping. However, for films deposited in lower oxygen containing environments the nearest neighbour hopping model can be used to describe the charge transport, as the value of p was closer to 1 than 0.5.

Baliga et. al. [19] deposited films of nickel manganate with cobalt doping using rf magnetron sputtering and suggested that in the temperature range of 100K to 250K, the charge transport mechanism for the films in the as-deposited state could be described by the Mott VRH ($T^{0.25}$ dependence) and not by the Shklovskii and Efros VRH model. However, below 160K, the films annealed at 270°C for 24 hours, could not be fitted to any of the hopping models. Dannenberg et. al. [16] found in their work that the same material followed the nearest neighbour hopping (polarons) behaviour for a wide range of temperatures. Their data did not fit very well to any of the variable range hopping models. They also suggested from thermopower measurement that when the proportion of oxygen in the sputtering environment was increased the conduction mode changed from p to n -type conductivity. This was concluded from a change in the sign of thermopower, which was positive for the p -type conductivity and negative for n -type conductivity. This transition from p -type to n -type was found in films deposited above 1% oxygen. The range of temperature in which the measurements were carried out was

quite large (77K to 525K). Although it was not possible to confirm their findings in the present study, a change in the value of the exponent p was observed for films produced in ambients containing similar levels of oxygen. Various other empirical relations have been used by other authors, as discussed in chapter 2, but they were not verified in this work.

6.5 CONCLUSIONS

Thin films of $Ni_xMn_{3-x}O_{4+\delta}$ were produced using rf magnetron sputtering from ceramic targets. The films showed poor crystallinity in the as-deposited condition independent of the substrate temperature used during deposition. However a post deposition annealing procedure was found to improve significantly the crystallinity of the films.

Films were annealed at various temperatures and it was found by analysing the XRD data that the peaks became narrower after annealing at 750°C. Williamson-Hall analysis of the peak widths showed that broadening was predominantly determined by the grain sizes and that the contribution from lattice strains was quite low. The grain sizes obtained by using the Scherrer equation clearly showed that the grain size increased significantly after annealing at 750°C, independent of the substrate temperature used during the deposition process. A slight broadening of the XRD peaks was noticeable in films annealed at 900°C. This was found to be consistent with the phase diagram of nickel manganate which suggests that nickel manganate exists in a single phase in the temperature range of 730°C upto 880°C. The lattice parameter of the films was lower than the target material but was independent of both the annealing temperatures in the range of 750°C to 850°C and the substrate temperature. The difference in lattice parameter between the target and the films was probably due to the lower oxygen content in the films.

All the films also exhibited some degree of preferred orientation towards the $\langle 100 \rangle$ direction, the degree of preferred orientation being dependent on the substrate temperature. The films deposited at 200°C exhibited the highest degree of preferred orientation.

The microstructure of the films deposited in pure argon was strongly dependent on the substrate temperature during deposition; however in the as-deposited state the films did not show any grain structure when studied using AFM. After annealing, the grain structure became more distinct and films deposited at 200°C and 250°C had a particularly well formed grain structure. The microstructure of the films deposited in argon/oxygen mixed environments showed similar temperature dependency but the structure in the as-deposited state reported by other authors could not be replicated. However problems experienced by Baliga et. al. in obtaining a good structure in films deposited in higher oxygen containing environments were not encountered in this study, but the composition used in their study was different from the one used here.

The $R-T$ measurements were undertaken on both as-deposited and annealed films and both exhibited NTCR characteristics. Statistically, the data fitted equally well to all three models (temperature dependencies) commonly used to describe the transport in this type of material. After analysing the variable range hopping models (of both Mott and Shklovskii and Efros), it was found that the Mott model could not be used for the films as it yielded a very low (probably unrealistic) value of the density of states of $\sim 10^{20} \text{ eV}^{-1} \text{ cm}^{-3}$. The Shklovskii and Efros model on the other hand showed values of the effective radius calculated from the T_0 of this model that were reasonable.

However when the data was fitted to the nearest neighbour hopping model the values of activation energy for the films were also in the range of those reported by other authors. Clearly an additional method was necessary to resolve this problem. An alternative analysis was carried out in an attempt to determine the exponent p in the generalised resistivity equation (equation (5.7)). Although the data were collected for a range of temperatures that was rather small for this type of analysis, it did suggest that there was a change in the conduction for films deposited in different oxygen containing environments. Charge transport in films deposited in lower levels of oxygen was possibly better described by the simple nearest neighbour hopping model as the value of p was found to be more than 1. For films deposited at higher levels of oxygen, the exponent tended to a value nearer 0.5, indicative of variable range hopping as proposed by Shklovskii and Efros. However there was some indication that it was not purely variable range hopping, but probably a situation where the transport was mixed. It was clear from this study that it is difficult to evaluate the charge transport mechanism in this type of material purely from fitting data to the conduction models as that can often be misleading and fail to represent the real situation.

Although this study identified the temperature dependence of the resistivity, it could not be resolved whether the transport was by small polarons or purely electronic, in films with the value of exponent $p > 1$. This was due to the fact that both in the polaronic and electronic models of NNH, the resistivity has a T^{-1} dependence.

The following chapter will investigate the electronic properties and structure of nickel manganate thin films using scanning tunnelling microscopy and scanning tunneling spectroscopy.

6.6 REFERENCES

- [1]. Binning, G., Quate, C.F., Gerber, C. *Atomic force microscope*, (1986) *Physical Review Letter*, **56**, 930-933.
- [2]. Abraham, F.F., Batra, I.P. *Theoretical interpretation of atomic-force-microscope images of graphite*, (1989) *Surface Science*, **209**, L125-L132.
- [3]. Ohnesorge, F., Binning, G. *True atomic-resolution by atomic force microscopy through repulsive and attractive forces*, (1993) *Science*, **260**, 1451-1456.
- [4]. Martin, Y., Williams, C.C., Wickramasinghe, H.K. *Atomic force microscope-force mapping and profiling on sub 100-Å scale*, (1987) *Journal of Applied Physics*, **61**, 4723-4935.
- [5]. Nishi, R., Houda, I., Aramata, T., Sugawara, Y., Morita, S. *Phase change detection of attractive force gradient by using a quartz resonator in noncontact atomic force microscopy*, (2000) *Applied Surface Science*, **157**, 332.
- [6]. Cullity, B.D. (1956) *Elements of X-ray diffraction*. Addison-Wesley Publishing Company, Inc., Reading, Massachusetts.
- [7]. Fau, P., Bonino, J.P., Demai, J.J., Rousset, A. *Thin films of nickel manganese oxide for NTC thermistor applications*, (1993) *Applied Surface Science*, **65/66**, 319-324.
- [8]. Abramowitz, M., Stegun, I.A. (1965) *Handbook of mathematical functions*. Dover Publishers, New York.
- [9]. Wickham, D.G. *Solid-phase equilibria in the system NiO-Mn₂O₃-O₂*, (1964) *Journal of Inorganic Nuclear Chemistry*, **26**, 1369-1377.
- [10]. Guinier, A. (1994) *X-ray diffraction in crystals, imperfect crystals and amorphous bodies*. Dover Publications.
- [11]. Hase, T.P.A. (1999) *Condensed matter physics course: x-rays & neutrons*. University of Durham.
- [12]. West, R.C. (1977) *CRC Handbook of chemistry and physics*. CRC Press Inc, Ohio.
- [13]. Boucher, B.P., Buhl, R., Perrin, M. *Etude cristallographique du manganite spinelle cubique NiMn₂O₄ par diffraction de neutron*, (1969) *Acta Cryst*, **B25**, 2326-2333.
- [14]. Cousins, M.A. (2001) *Microstructure of absorber layers in CdTe/CdS solar Cells*. In *Department of Physics*, University of Durham, Durham.

- [15]. Baliga, S., Jain, A.L. *Deposition and properties of rf magnetron sputtered $Ni_{0.6}Mn_{2.4}O_4$* , (1989) *Materials Letters*, **8**, 175-178.
- [16]. Dannenberg, R., Baliga, S., Gambino, R.J., King, A.H., Doctor, A.P. *Resistivity thermopower and the correlation to infrared active vibrations of $Mn_{1.56}Co_{0.96}Ni_{0.48}O_4$ spinel films sputtered in an oxygen partial pressure series*, (1999) *Journal of Applied Physics*, **86**, 514-523.
- [17]. Sun, Y., Xu, X., Zhang, Y. *Variable-range hopping of small polarons in mixed-valence manganites*, (2000) *Journal of physics: Condensed matters*, **12**, 10475-10480.
- [18]. Zabrodskii, A.G. *Electrical conductivity of heavily doped compensated n-type germanium produced by neutron doping*, (1980) *Soviet Physics Semiconductors*, **14**, 670-676.
- [19]. Baliga, S., Jain, A.L. *Hopping conduction in sputtered Ni-Co-Mn-O spinel films*, (1991) *Materials Letters*, **11**, 226-228.

Electronic Properties of $Ni_xMn_{3-x}O_{4+\delta}$ Thin Films

7.1 INTRODUCTION

This chapter deals with the investigation of the electronic properties of nickel manganate thin films using scanning tunneling microscopy (STM) and scanning tunneling spectroscopy (STS). STM provides a real-space image of surfaces with very high resolution and STS gives information on the electronic structure of a sample by probing the sample density of states as a function of energy [1]. An investigation of the electronic structure was undertaken as a function of temperature in the range of 20°C to 200°C which is the range of application for devices made from such materials [2]. This also is the same temperature range in which the electrical measurements ($R-T$) were performed, the results of which were presented in chapter 6. Although much effort has been devoted to studying the structural, electrical and optical properties of this class of materials, their electronic structure has remained largely unresearched. No evidence was found of tunneling spectroscopy experiments carried out on spinel type material. Temperature dependent spectroscopy has been carried out on other materials [3] [4] [5] at low (cryogenic) temperatures but no published information on STS performed in the temperature range investigated in the present work has been found.

7.2 THEORETICAL BACKGROUND

7.2.1 SCANNING TUNNELING MICROSCOPY

Since the invention of the STM by Gerd Binnig and Heinrich Rohrer in 1981, it has been widely used in the fields of material science, physics, electrochemistry, tribology, biochemistry, organic chemistry and in other areas. Scanning tunneling microscopy is a technique capable of providing real-space images of surfaces with sub-nanometer spatial resolution. Shortly after the discovery of STM, Binnig et. al. [6] reported the first atomic resolution images [7]. A schematic representation of the imaging process of a STM is shown in figure 7.1. The tip, which is generally made of well characterised metals such as platinum, tungsten, platinum-iridium is brought close to the surface under investigation, so that the wave functions of the tip and sample

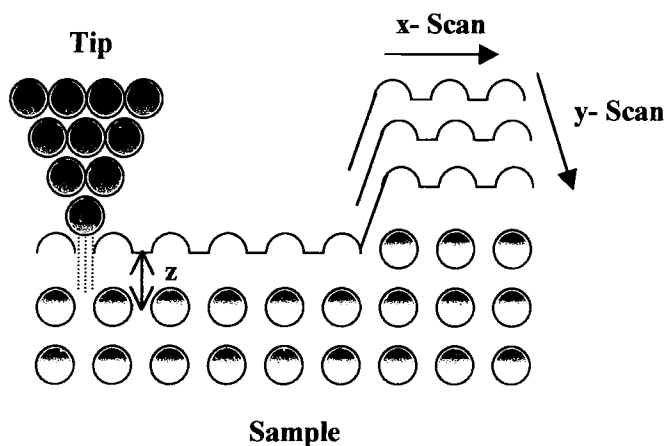


Figure 7.1 Schematic diagram showing the principles of the imaging process in a STM

surfaces overlap. In such a situation, a finite probability exists that electrons will cross the barrier between the two surfaces when a bias is applied across them. STM can be operated in two different modes namely, constant height mode and constant current

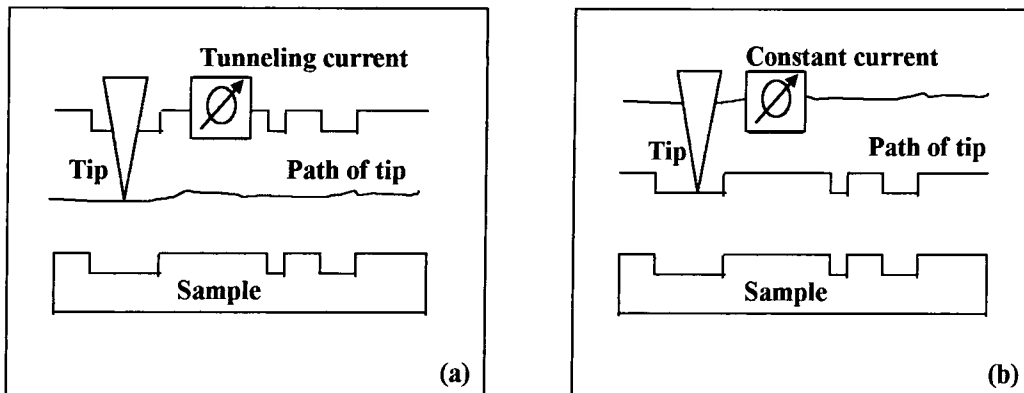


Figure 7.2 Imaging modes of STM (a) constant height mode and (b) constant current mode

mode. The terms are self explanatory; in the constant height mode, the vertical position of the tip is fixed and a constant bias is maintained. As the tip scans the surface, the current varies depending on the topography and the local surface electronic properties of the sample. The tunneling current measured at each point on the surface forms the data and constitutes the topographic image. A schematic representation of this mode of operation is shown in figure 7.2 (a). In the constant current mode (see figure 7.2 (b)), a feedback mechanism is used to maintain a constant current by altering the distance between the tip and the sample while applying a constant voltage. In this mode, the motion of the tip as it is scanned over the surface forms the data set. The image of the topography obtained from a STM can be interpreted as a contour of constant surface charge density.

Each mode of operation has both advantages and disadvantages. In the constant height mode, the process is faster but the surface must be relatively flat to obtain useful information. On the other hand, although scanning a sample using the constant current mode is comparatively slow, irregular surfaces can be investigated with greater precision. Contrast in a STM image arises from the convolution of the electronic

structures of the sample surface and tip and the transmission coefficient between the tip and the sample surface. In order to get information about electronic properties of the sample it is necessary to minimise the contribution of the transmission coefficient.

7.2.2 SCANNING TUNNELLING SPECTROSCOPY

One of the interesting aspects of STM is that in addition to topographic information, it inherently contains a large amount of data about the local electronic structure of the surface. In the early stages of their work with STM, Binnig et. al. found that the appearance of the image of graphite [8] changed with applied bias. It transpired that this was due to tunnelling of electrons through the electronic states of the sample. This led to the development of scanning tunnelling spectroscopy, which provides detailed local information on the electronic structure of surfaces.

The spectroscopy is carried out in the constant current mode of the STM. The tip is brought into position over the sample and the tip-sample distance adjusted to gain the required constant current. The feedback loop is disengaged and subsequently a range of voltages is applied and the resulting currents recorded. The feedback loop is then switched back on and the tip is moved on to the next position and the whole process is repeated. The range of voltages applied depends on the energy range of interest, but typically this is $\sim \pm 3-4$ volts.

The energy level diagrams shown in figure 7.3 illustrate a system consisting of a metal tip with constant density of states, separated by vacuum from the sample, which has a distribution of density of states. In figure 7.3 (a) the sample and the tip are far apart and independent. Their Fermi levels (E_F) lie below the vacuum level by their respective

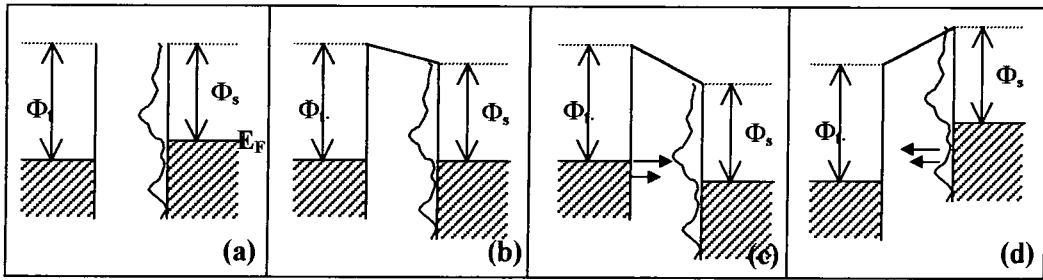


Figure 7.3 Energy band diagrams of the tip and the sample in a STM describing the STS mode of operation

work function Φ_s (sample) and Φ_t (tip). When the tip and sample are brought in close proximity, the Fermi levels line up (equilibrate) as shown in figure 7.3 (b). When a positive bias is applied to the sample, the equilibrium is disturbed and the Fermi level of the sample is shifted down with respect to the tip and electrons flow from the occupied states of the tip to the unoccupied states of the sample, as illustrated in figure 7.3 (c). Figure 7.3 (d) shows the converse situation where the bias is reversed in which case the electron current flows from the sample to the tip. The resulting tunneling current can be expressed as

$$I = \int_{E_F}^{E_F+eV} \rho_s(E_\mu) \rho_t(E_\mu - eV) [f(E_\mu - eV) - f(E_\mu)] T(E_\mu, eV) dE_\mu \quad (7.1)$$

where ρ_s and ρ_t are the density of states of the sample and the tip respectively, T is the transmission coefficient between the tip and the sample and f is the Fermi function. It is clear from the above expression that the tunnelling current is dependent on the density of states of the tip and the sample and the transmission coefficient.

The first derivative of the equation (7.1) with respect to the applied bias, gives the conductance of the material and can be written as

$$\frac{dI}{dV} = e \int_{E_F}^{E_F + eV} \rho_s(E_\mu) \frac{d}{dV} \rho_\tau(E_\mu - eV) T(E_\mu, eV) dE_\mu + e \rho_s(E_F + eV) \rho_\tau(E_F) T(E_F + eV, eV) \quad (7.2)$$

In equation 7.2 the second term contains the voltage dependence of the transmission coefficient T . In 1987, Feenstra et. al. [9] proposed a normalisation method for the dI/dV expression which minimises the effect of the transmission coefficient. In this procedure both sides of the equation are divided by I/V followed by dividing both the numerator and the denominator by $T(E_F + eV, eV)$. The normalised dI/dV is then expressed as

$$\frac{dI/dV}{I/V} = \frac{\rho_s(E_F + eV) \rho_\tau(E_F) + \int_{E_F}^{E_F + eV} \rho_\tau \rho_s(E_\mu) \frac{d}{dV} \frac{(E_\mu - eV) T(E_\mu, eV)}{T(E_F + eV, eV)} dE_\mu}{\frac{1}{eV} \int_{E_F}^{E_F + eV} \rho_s(E_\mu) \rho_\tau(E_\mu - eV) \frac{T(E_\mu, eV)}{T(E_F + eV, eV)} dE_\mu} \quad (7.3)$$

In the above expression, the transmission coefficients $T(E_\mu, eV)$ and $T(E_F + eV, eV)$ appear as a ratio in the both the second part of the numerator and the denominator and hence their dependence on voltage tends to be cancelled. This method for normalisation of the STS data is widely accepted as providing a suitable way to reduce the effects of T .

7.2.3 CURRENT IMAGING TUNNELING SPECTROSCOPY

Tunnelling spectroscopy can either be done on a single point on the surface or over an area, where spectroscopic measurements are done at a number of positions in the area. The latter method, which is often known as current imaging tunnelling spectroscopy, was developed by Hammers et. al. [10] and helps in producing maps of density of states of the surface at particular energies. This is useful to study the electronic structure associated with particular features on the surfaces such as grain boundaries and

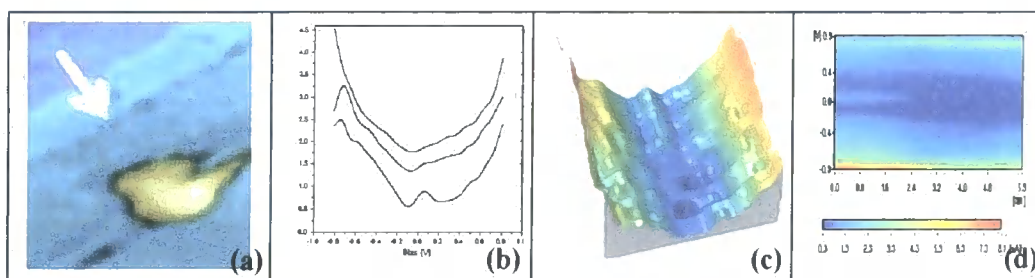


Figure 7.4 Contour map representation of CITS results (a) STM image of a surface, (b) normalised dI/dV curves of three points along the arrow in the STM image; (c) three dimensional representation of normalised spectra of all the points along the arrow grouped together and (d) two dimensional contour map of all the normalised spectra

to compare them with those associated with for example the grain. The results are presented in the form of either maps of normalised conductance at a particular energy or as contour maps of the normalised conductance spectra. An example of a contour map, which can be described as a two dimensional representation of normalised conductance spectra along a chosen line on the STM image, is shown in figure 7.4. This method of representation again provides a general view of the electronic structure of a surface.

7.3 EXPERIMENTAL

The experiments were done in an ultra high vacuum Omicron AFM/STM equipped with in-situ sample heating facilities. All the STM/STS measurements were performed using a tip made by mechanically sectioning thin platinum/iridium wire. The films were cut into 10 x 10 mm pieces and cleaned using acetone in an ultrasonic bath to remove any contamination from the surface and then placed into the microscope using a secondary load lock chamber. All the measurements were recorded under a pressure of $\sim 2 \times 10^{-10}$ mbar.

Experiments were carried out in the constant current mode of the STM with a bias of 1 volt and the tunnelling current was maintained at either 1 or 0.2 nA. The spectroscopy was carried out on every pixel of a 600 x 600 nm area of the surface, with a resolution of 256 x 256 pixels. During the spectroscopy, the I/V curves were recorded by interrupted-feed-back-loop technique. Based on these measurements the first derivative was calculated and then normalised using the technique described in section 7.2.2. The data were analysed using purpose written software [11], which performed all the numerical calculations and mappings.

7.4 EFFECT OF POST DEPOSITION ANNEALING

Current imaging tunnelling spectroscopy was carried out on films deposited in an ambient of argon/oxygen (2.5% oxygen) with the substrate at 35°C. The spectroscopy was carried out in both the as-deposited state and after annealing at 800°C in air. Figure 7.5 shows the topograph and the corresponding normalised conductance map near the Fermi level (~ 0 eV) of a film in the as-deposited state. It was evident that the electronic

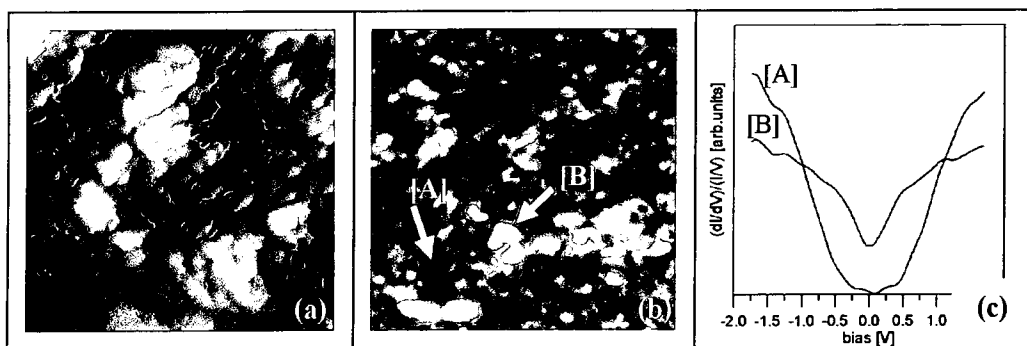


Figure 7.5 (a) Topology of as-deposited film (300 x 300 nm), (b) normalised conductance map at Fermi energy (~ 0 eV) and (c) the normalised conductance spectra of characteristic regions of the conductance map

structure of the film surface was not homogeneous and consisted of several bright regions [B] with a higher local density of states (LDOS) at the Fermi level, compared to the much darker background [A] with a lower value of LDOS. Comparison of the figures 7.5 (a) and (b) also indicated that the inhomogeneity could not be attributed to any topological feature of the surface and it had to be assumed that the bright contrast regions were present either due to surface defects or different stoichiometry of the material. Since the sputtering was carried out in an atmosphere containing oxygen it was possible that some areas were richer in oxygen than others, although this could not be verified due to the unavailability of any in-situ elemental characterisation techniques. The normalised spectra of bright and dark regions in the figure 7.5 (b) represented by [A] and [B] are shown in figure 7.5 (c). It can be seen that the representative spectrum of the bright regions [B] had a high value of LDOS at Fermi level, which is more characteristic of metals whereas the representative spectrum from the dark regions [A] showed more semiconducting behaviour.

The films were subsequently annealed in air at 800°C for 1 hour, followed by quenching to room temperature. The spectroscopic measurements were repeated using the same experimental conditions. Figure 7.6 shows the topology (a), the corresponding

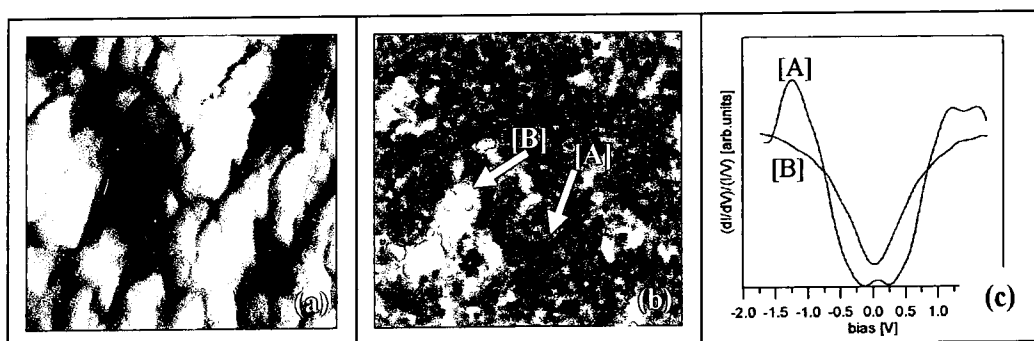


Figure 7.6 (a) Topology of annealed film (300 x 300 nm), (b) normalised conductance map at Fermi energy (~ 0 eV) and (c) the normalised conductance spectra of characteristic regions of the conductance map

normalised conductance map at the Fermi level (b) and the characteristic spectra of the annealed film (c). The normalised conductance map still showed regions with bright and dark contrast, but the areas with bright contrast were much less abundant than in the as-deposited films. Again, the conductance maps bore very little correlation with the topology of the film. The normalised conductance spectra, which are shown in figure 7.6 (c), are similar to those for the films in as-deposited state but the spectrum of the dark regions shows a small maximum very near the Fermi level. Although the results presented are for a very small area (300 x 300 nm), they were representative of the whole surface. Other parts of the films were also investigated and similar results were found.

The higher presence of bright (high LDOS) regions in the as-deposited layers would suggest that these films would be more conducting. The $R-T$ measurements presented in chapter 6 however indicated that this was not true, which implied that the bright regions were not contiguous (i.e. percolation paths) and/or that there were some potential barriers to the current flow between the two types of surfaces. Additionally the shape of the spectrum in the case of the annealed film was narrower than for the films in the as-deposited state. The vertical scale in the normalised conductance spectra is arbitrary, consequently this makes it difficult to carry out a quantitative comparison of values of LDOS obtained from different experiments. However, Yao et. al. [4], in their work with $Pr_{0.5}Sr_{0.5}MnO_3$ thin films, compared the values of LDOS from the normalised spectra collected at different temperatures and concluded that at 190K the material had a higher LDOS (beyond 0.2 eV) than at other temperatures and as a result concluded that the films were more conductive at 190K. Similarly, in the present study the shape of the normalised spectra was narrower for annealed films than for films in as-deposited state, suggesting that the LDOS at the same energies were higher in the annealed films. This

possibly implies, similar to that suggested by Yao et. al. that the films became more conducting after annealing, which was consistent with the $R-T$ measurements described in chapter 6.

7.5 TEMPERATURE DEPENDENT SPECTROSCOPY

Scanning tunneling spectroscopy was carried out on layers deposited in different oxygen/argon (2.5%, 10% and 15% oxygen) containing ambients and subsequently annealed in air at 800°C for 1 hour. The aim of the study was to investigate the effect of

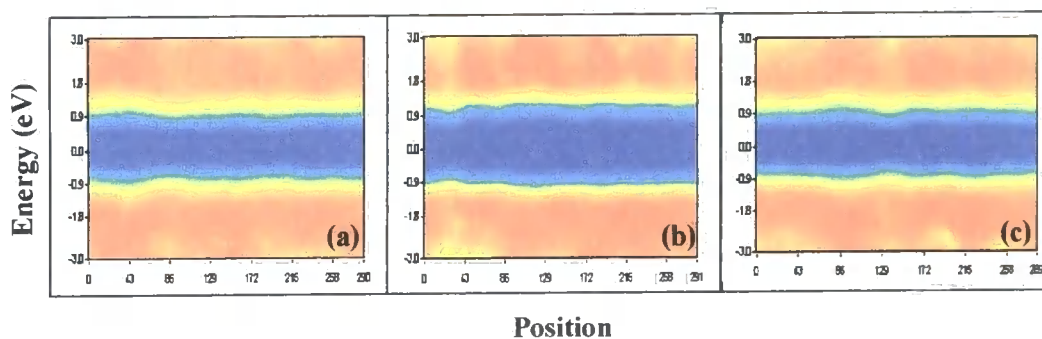


Figure 7.7 Room temperature contour maps of the normalised conductance spectra of films deposited in (a) 2.5% oxygen ambient, (b) 10% oxygen ambient and (c) 15% oxygen ambient

temperature on the electronic structure of films produced in different sputtering conditions. Initial experiments were undertaken at room temperature and at 200°C, the same range in which the $R-T$ measurements were carried out.

The contour maps of ~ 290 points on the surface, of the three types of films at room temperature are shown in figure 7.7. The characteristics of all the three films looked very similar and the shape of the LDOS suggested that the films behaved like

semiconductors as the value of LDOS around the Fermi level was very close to zero. The blue region in the middle corresponds to low values of LDOS. The width of the LDOS curve varied but did not show any trends.

The results of the spectroscopy carried out at 200°C are shown in figure 7.8 and show significant differences compared to the results at room temperature. Additional features

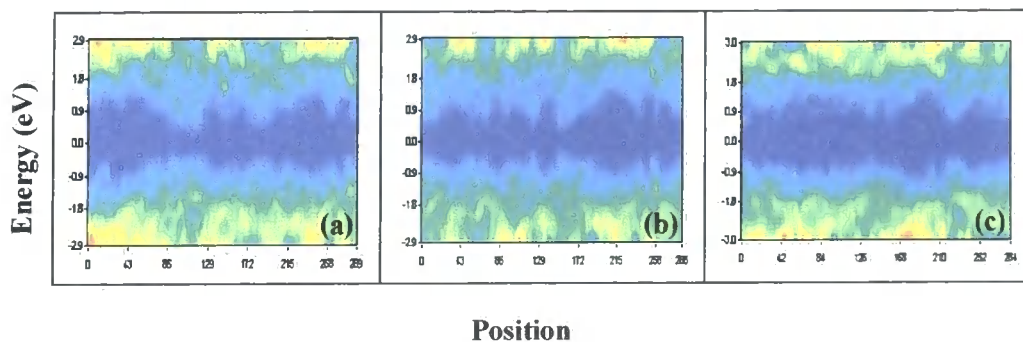


Figure 7.8 Contour maps of the normalised conductance spectra recorded at 200°C for films deposited in (a) 2.5% oxygen ambient, (b) 10% oxygen ambient and (c) 15% oxygen ambient

were present very near the Fermi level which were not observed when the spectroscopy was carried out at room temperature. The shape of the LDOS was parabolic but with additional maxima around ± 0.15 eV to ± 1.6 eV. The spectroscopic results of the films after being cooled to room temperature were similar to the ones shown in figure 7.7. The changes in the shape of the LDOS observed at 200°C were reversible with temperature implying that no permanent change to the electronic structure occurred. This ruled out the possible outward diffusion of oxygen from the material because of heating in vacuum, which would alter the stoichiometry and possibly influence the electronic structure.

The additional features observed close to the Fermi level were studied in greater detail by performing spectroscopy in both low (± 1 eV) and high energy (± 3 eV) ranges. The experimental parameters were kept the same for all the measurements. The results of the high energy spectroscopy at different temperatures are shown in figure 7.9 (a). The general shape of the LDOS was parabolic at all temperatures. On a more detailed study of the spectra, the presence of a maximum close to the Fermi level, as seen in section 7.4 for the annealed film was also observed, but it was not well resolved in the wide energy range over which the spectroscopy was carried out. This feature is denoted in

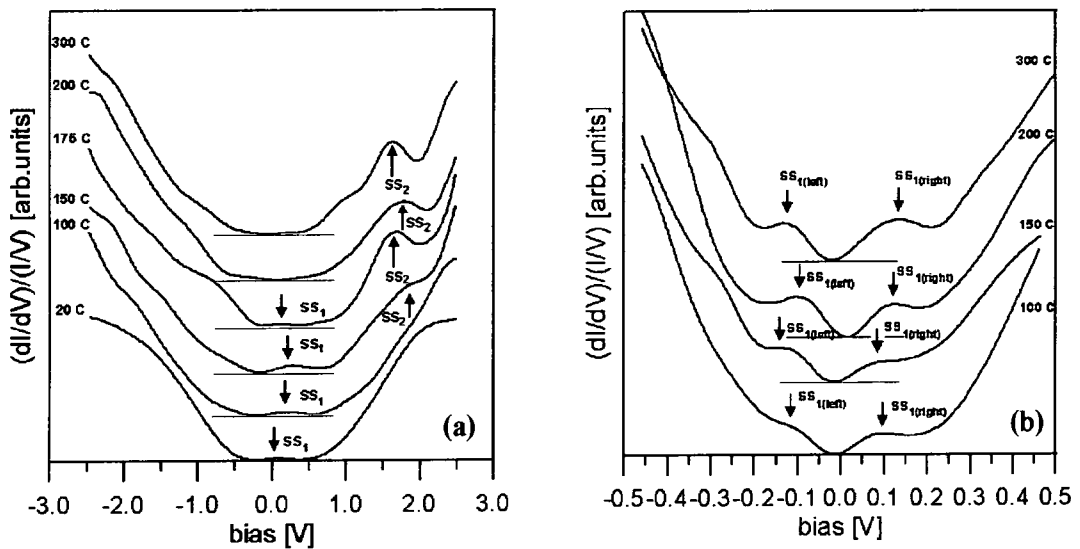


Figure 7.9 (a) High energy spectroscopy results at different temperatures indicating the additional features SS_1 near the Fermi level and SS_2 at about $\sim +1.6$ eV (b) Low energy spectroscopy showing the evolution of peaks around the Fermi level at $\sim \pm 150$ meV

the figure 7.9 (a) as SS_1 . The other noticeable feature in figure 7.9 (a) was the appearance of a peak at around $\sim +1.6$ eV in the unoccupied part of the spectra (SS_2). The appearance of the peak was completely reversible and it disappeared when the temperature was lowered. There were some other features in the occupied part of the

spectra as well at higher temperatures although they were not well differentiated and are thus not discussed.

The low energy range spectroscopy results, which were carried out to study the electronic structures close to the Fermi level in more detail and in particular the feature denoted by SS_1 are shown in figure 7.9 (b). The results confirmed the shape of the LDOS around the Fermi level to be parabolic with maxima at around $\sim \pm 150$ meV evolving with increasing temperatures. The evolution of these features, which appeared on both the occupied and the unoccupied parts of the spectra was well differentiated from 100°C onwards. As in the high energy spectroscopy the behaviour of the peaks in the low energy range was completely reversible and they disappeared after the sample was cooled down to room temperature.

Mott et. al. [12] suggested that in amorphous semiconductors, states are present in the energy gap due to impurities, defects and microvoids as in crystalline semiconductors. In amorphous films of germanium and silicon and some compounds of these elements for example, the electrical conductivity mechanism is often hopping of electrons with energies very near the Fermi level, between these defect states. Spear et. al. [13] found that the Fermi level of silicon films prepared by glow discharge decomposition of SiH_4 was located near a minimum between two maxima in the density of states. He suggested that the centres responsible for this effect could have originated from pairs of dangling bonds at defects similar to the commonly observed divacancy in silicon crystals. The state above the Fermi level was associated with the anti-bonding states and the one below the Fermi level with the bonding states. Although the material system used in the current investigation was quite different from silicon, the evolution of two maxima above and below the Fermi level was similar in character to those reported by Spear et.

al.[13]. Due to similarities between the observed behavior of nickel manganate in the present study and that of silicon films in terms of the conduction mechanism, similar conclusions may be drawn about the states observed around the Fermi level for nickel manganate. In the absence of any theoretical models for nickel manganate, these conclusions remain speculative. Also in the present study these maxima evolved with increasing temperature and were not clearly resolved at lower temperatures. The reversible character of the features ruled out any change in stoichiometry as discussed earlier in this section. Experiments were carried out under various conditions to rule out any effects from the experimental artifacts.

7.6 CONCLUSIONS

In this chapter the electronic structure of nickel manganate thin films was studied using STM and STS. The effect of post deposition annealing at 800°C on the electronic properties was investigated and the results confirmed that the inhomogeneity of the surface electronic states was considerably reduced as a result of that process. The as-deposited films showed islands of high conductivity with other areas showing semiconducting characteristics. The inhomogeneity of the surface was attributed to defects induced during the growth process of the films.

STS measurements of annealed films deposited at various oxygen partial pressures were studied in the energy range of ± 3 eV as a function of temperature. The room temperature measurements indicated that the material showed semiconductor characteristics with a very low LDOS at the Fermi level, however a definite forbidden gap could not be seen. The shape of the LDOS in the energy range studied was parabolic which supported the assumption made in the variable range hopping model

proposed by Shklovskii and Efros. This model has been used to explain the transport properties of films deposited in oxygen rich ambients ($O_2 > 1\%$) in chapter 6. The distribution of the LDOS did not show any noticeable difference for films deposited in ambients with different amounts of oxygen. At higher temperatures however, additional features in the form of maxima around $\sim \pm 150$ meV and $\sim + 1.6$ eV were observed. The maxima at lower energies could only be observed when the spectroscopy was carried out over a smaller energy range (± 1 eV). These low energy features showed some similarities with what was observed in amorphous silicon films. For silicon they are thought to arise due to dangling bonds at defect sites in the material.

This has been a first attempt to study the electronic structure as a function of temperature for this class of spinel structured material by scanning tunneling spectroscopy. The results clearly showed the temperature dependence of the conductance spectra of nickel manganate. The conductance spectra of the material also supported the transport model proposed for this material as discussed in chapter 6.

The next chapter will attempt to summarise the results and discussions presented in this thesis. Scope for future work, which may enhance the understanding of the nickel manganate material system will be proposed.

7.7 REFERENCES

- [1]. Chen, C.J. (1993) *Introduction to scanning tunneling microscopy*. Oxford University Press, New York.
- [2]. Feltz, A., Kriegel, R., Poelzl, W. *Sr₇Mn₄O₁₅ ceramics for high temperature NTC thermistors*, (1999) *Journal of Materials Science Letters*, **18**, 1693-1695.
- [3]. Maggio-Aprile, I., Renner, C., Erb, A., Walker, E., Revaz, B., Genoud, J.Y., Kadowaki, K., Fischer, O. *Temperature dependence of tunneling spectra in YBa₂Cu₃O_{7-d} and Bi₂Sr₂CaCu₂O_{8+d} single crystals*, (2000) *Journal of Electron Spectroscopy and Related Phenomena*, **109**, 147.
- [4]. Yao, B.C., Lee, J.B., Chi, C.C., Wu, M.K., Yang, H.C. *Temperature dependence of tunneling spectroscopy in epitaxial thin film Pr_{0.5}Sr_{0.5}MnO₃*, (2000) *Journal of Magnetism and Magnetic Materials*, **209**, 103.
- [5]. Biswas, A., Raychoudhuri, A.K. *Tunnelling spectroscopy and the density of states of La_{0.8}Ca_{0.2}MnO₃*, (1996) *Journal of Physics : Condensed Matter*, **8**, L739.
- [6]. Binnig, G., Rohrer, H. *Scanning Tunneling Microscopy*, (1982) *Helvetica Physica Acta*, **55**, 726.
- [7]. Binnig, G., Rohrer, H., Gerber, C., Weibel, E. *7 x 7 reconstruction on Si(111) resolved in real space*, (1983) *Physical Reviews Letters*, **50**.
- [8]. Binnig, G., Fuchs, H., Gerber, C., Rohrer, H., Stoll, E., Tosatti, E. *Energy dependent state-density corrugation of a graphite surface as seen by scanning tunnelling microscopy*, (1983) *Europhysics Letters*, **1**, 31.
- [9]. Feenstra, R.M., Strociro, J.A., Fein, A.P. *Tunneling spectroscopy of the Si(111) 2x1 surface*, (1987) *Surface Science*, **181**, 295.
- [10]. Hammers, R.J., Tromp, R.M., Demuth, J.E. *Surface electronic structure of Si (111) 7x7 resolved in real space*, (1986) *Physical Reviews Letters*, **56**, 1972.
- [11]. Kowalczyk, P, University of Lodz, Department of Solid State Physics, Poland.
- [12]. Mott, N.F., Davis, E.A. (1979) *Electronic Processes in Non-crystalline Materials*. Clarendon Press, Oxford.
- [13]. Spear, W.E., Le Comber, P.G. *Substitutional doping of amorphous silicon*, (1975) *Solid State Communications*, **17**, 1193.

Conclusions and Scope for Future Work

8.1 CONCLUSIONS

The aim of this project was to design and construct a rf magnetron sputtering system for depositing nickel manganate thin films from a ceramic target and to study the structural and electrical characteristics of the resulting films. The rf magnetron system, which took 14 months to design, build and commission was capable of depositing eight films per vacuum cycle. It was designed so that the substrate temperature, the composition and the flow of the sputtering gas, the sputtering pressure and the incident power could be controlled separately and monitored throughout the deposition process. Provision was also made to be able to adjust the substrate to target distance, although this had to be done when the deposition chamber was open. The effects of all the parameters on the deposition rate were studied and it was found that the rate decreased when the substrate temperature, the oxygen percentage or the separation between the target and the substrate were increased. On the other hand the rate increased linearly with an increase in the incident power and remained largely unaffected by changes in pressure during sputtering.

A factorial experimental design experiment was carried out using the four most important factors at two levels. It showed that substrate temperature had the least effect on the growth rate and revealed that the rate of deposition increased with an increase in the substrate temperature but not independently of the sputtering gas composition. This was explained by an increased rate of reaction of oxygen with the deposited material resulting in an increased rate of compound formation, at higher substrate temperatures. The interaction plots between the factors highlighted the importance of the oxygen content in the ambient during sputtering. The incident power and the distance between the target and the substrate were found to be statistically most significant, followed by the oxygen percentage and the interaction between the oxygen content and incident power. The FED experiments provided a good insight into the role of each of the parameters on the deposition rate, both individually and in combination. Deposition rates as high as ~19 nm/min were obtained when the incident power was 70 Watts (~8 Watts cm⁻²) but it was found that such a high power caused excessive heating of the target and ultimately its destruction. It was not possible to use more than 30 Watts (~3.5 Watts cm⁻²) power without damaging the target.

Structural and electrical characterisation of bulk $Ni_xMn_{3-x}O_{4+\delta}$ was carried out. Compositional analysis was done using EDAX and it was in good agreement with the precursor ratios used in preparing the material. However, Rietveld refinement of the x-ray diffraction data of all the compositions quenched directly from the sintering temperature, showed that single-phase material could not be obtained unless it had been annealed for a long period (40 hours) at 800°C following sintering. Single phase stoichiometric nickel manganate ($R=0.66$) could only be prepared when sintering took place at 1100°C followed by annealing. Monophasic nickel deficient spinels were obtained after sintering at lower temperatures of 1000°C ($R=0.71$) and 900°C ($R=0.73$),

0.74 and 0.75) followed by annealing at 800°C before quench cooling in liquid nitrogen. The target composition used for this study was the nickel deficient ($R = 0.71$) material sintered at 1200°C for 24 hours and annealed at 800°C for 40 hours. The lattice parameters of the monophasic material increased linearly with decreasing amounts of nickel in the compositions.

The spinel phase present in the material quenched directly after sintering, was always manganese rich and the nickel deficiency increased with increasing sintering temperature for the compositions with $R = 0.66, 0.71, 0.73$. For the other two compositions there was some degree of nickel incorporation when sintered above 1000°C. The composition of the spinel phase for the material with $R = 0.71$ at each temperature was calculated using the lattice parameter and the possible reaction taking place was proposed. However the reactions could not take into account the oxygen loss at those temperatures. The results of the experiments did not correspond well with a previously published phase diagram which indicated that the nickel deficient compositions ($R = 0.73, 0.74$ and 0.75) existed as single phases when sintered at temperatures above 1000°C. Hence a modification to the phase diagram was proposed which showed that all the compositions had *NiO* as a secondary phase in the temperature range of 900°C to 1200°C and only existed in single phase within a narrow range of temperature.

The microstructure of the materials showed the formation of a dense ceramic body with considerable grain growth with increasing temperature. The grain size distribution was calculated for the annealed materials and was fitted to a Rayleigh distribution function. The mode size of the distribution function increased with rising sintering temperatures from 0.58 μm at 800°C to 1.81 μm at 1200°C. A sharp increase in the density of the

pellets was also observed when sintered at 1200°C, with a significant decrease in the porosity (~4% for the target material).

The R - T measurements carried out in the range of 120K up to 350K indicated that all the materials showed good NTCR characteristics. The data were fitted to the conventional electron hopping models and it was clear that the nearest neighbour hopping model could not be applied to the entire data range. The data fitted the variable range hopping model proposed by Mott [1] reasonably well, but the characteristic temperature (T_0) value was too high ($\sim 10^9$ K). The density of states, which is inversely proportional to the T_0 was therefore found to be too low for this type of material and hence the model could not be applied. The data also fitted the variable range hopping model proposed by Shklovskii and Efros [2] and the characteristic temperature was found to be more reasonable (in the order of 10^5 K) and gave a realistic estimate of the effective radius for the material of $\sim 2.5 \times 10^{-10}$ m.

However when the value of the exponent p in the relevant expression (5.7) was determined using Zabrodskii's [3] method, it was found that the Shklovskii and Efros VRH model could only be applied up to 300K. Above that temperature a change in the value of p was observed indicating a change in the mechanism and the conduction could be better described by the NNH model with an activation energy (~ 320 meV) similar to that found in the literature. The mechanism responsible for this change in the conduction process as found from the analysis remained largely unexplained. The resistivity of the material was found to be dependent both on the nickel content and the sintering temperature. The change in resistivity of the material could be attributed to the change in the ratio of Mn^{3+} to Mn^{4+} which is indicated in the pre-exponential term ρ_0 in the resistivity expression of the NNH (polaronic) model. The results showed that

annealing for a long time at 800°C was not enough to restore the oxygen stoichiometry of the material although complete reincorporation of *NiO* was taking place in most cases. It was evident from the results that the resistivity of the nickel manganate system could be tuned to suit particular applications by altering either the nickel content in the composition or/and the sintering temperature, from as low as 1.2 Kohm-cm up to 30 Kohm-cm at 323K.

Thin films were produced using the rf magnetron sputtering system and structural characterisation was carried out on films deposited in an argon atmosphere. The films in the as-deposited state showed poor crystallinity even when deposited at a substrate temperature of 250°C. However a marked improvement in the crystallinity was observed for most films when they were annealed at 750°C, with the peaks in the XRD pattern becoming much sharper compared to the ones for films annealed at 700°C. The exceptions were films deposited at 250°C where the annealing temperature had to be raised to 800°C before any improvement in crystallinity could be observed. Williamson-Hall analysis [4] [5] of the XRD patterns confirmed that the change in the peak shape was primarily due to a change in the grain size and that the contribution from lattice strain was negligible. This was also evident from the grain size values obtained using the Scherrer equation with the (400) reflection. The peaks showed some degree of broadening after annealing at 900°C, which suggested possible presence of secondary phases. The temperature range where the peak shape was sharp corresponded well with the phase diagram of the nickel manganate system. The films, irrespective of the substrate temperature, exhibited preferred orientation (ratio of 311:400) towards the <100> direction after annealing at 800°C. The lattice parameters of the films were lower than those of the target material suggesting that the films were nickel rich, but the results of the elemental analysis of the films using EDAX showed that the ratio of nickel to manganese was very similar to the target material. Hence this discrepancy was

thought to be due to the lack of oxygen in the films. The degree of preferred orientation was dependent on the substrate temperature, with the films deposited at 200°C showing the largest preference towards the <100> direction.

The microstructure, studied using AFM, of the films showed marked differences after annealing at 800°C. The films deposited with the substrate at 200°C and 250°C showed a dense structure with clearly defined grain boundaries and regular shaped grains ~ 30-90 nm in size. The microstructure of the films deposited at lower substrate temperatures had a very different microstructure although some ordering was observed after annealing. The films deposited in argon/oxygen ambients had similar microstructures to those deposited in pure argon.

The resistivity of the as-deposited films decreased as the oxygen content in the sputtering environment increased. Annealing in air and in ambients similar to those used during sputtering resulted in an overall decrease in the resistivity to the levels of that of the as-deposited films produced with 15% oxygen in the ambient. This suggested that the annealing process changed the oxygen stoichiometry of the films and the films deposited in lower oxygen containing environments were most affected. The resistivity of the films after annealing was lower than that of the target material, which could have resulted from a difference in oxygen stoichiometry and/or a better intergranular contact in thin films compared to the target.

All the films showed NTCR characteristics and the data statistically fitted all the conventional models of charge transport well. The same analyses were carried out as done for the bulk material and it showed that the Mott VRH model could not be applied due to the very high values of the characteristic temperature (T_0) obtained. The Shklovskii and Efros VRH model could be applied satisfactorily and the characteristic

temperature (T_0) value was very similar to that of the target material. The characteristic temperature of the films deposited in very low oxygen containing ambients (0.3% and 1%) were found to be quite high compared to the others. However no trends in the characteristic temperature with different oxygen content in the ambient during sputtering were observed. The activation energies obtained by fitting the data to the NNH model were also in the range of those reported in the literature.

The analysis to determine the value of p in the resistivity expression, revealed that the films deposited in low oxygen containing environments (0.3%, 1% and possibly 2.5%) had values very near to 1 which suggested that the NNH model could be used to explain the conduction mechanism satisfactorily. However, the films deposited in oxygen rich ambients had values of p of around 0.6 – 0.75. This was an indication that the conduction mechanism in these films was the VRH mode as proposed by Shklovskii and Efros. Since some of the values were very near to 0.75, it is possible that for some films there was a mixed conduction where both the NNH and VRH models were contributing.

It was evident from the analysis of the $R-T$ data of both the bulk and the thin films that merely fitting the data to the models did not always determine the underlying mechanism definitively. As in most cases more than one model could be fitted to the data, hence independent methods such as the one used in this study are needed to resolve this problem.

The electronic structure of the thin films was investigated using scanning tunneling spectroscopy in the energy range of $\pm 3\text{eV}$. The CITS maps of as-deposited films showed inhomogeneity on the surface. There were areas with a high value of LDOS at the Fermi level showing almost metallic characteristics and other areas showing more semiconducting characteristics with a very low value of LDOS at the Fermi level. After

annealing the surface became more homogeneous although a few of the highly conducting regions could still be seen. The conducting regions on the surface were isolated by the less conductive regions, which probably resulted in a lack of percolation paths and a higher resistivity of the films in the as-deposited state. After annealing the surface was more homogeneous making the films less resistive. The overall distribution of the LDOS of the semiconducting regions was parabolic and that was true for all films irrespective of the deposition conditions.

When the spectroscopy was done at higher temperatures ($>100^{\circ}\text{C}$), additional features in the form of maxima were seen in the LDOS spectra around $\sim+1.6$ eV and $\sim\pm 0.15$ eV. The features at low energy were very similar to those seen in amorphous *Si* thin films, believed to result from defects such as dangling bonds on the surface. All the features were reversible with temperature suggesting no permanent change in the electronic structure of the films. The cause of these phenomena could not be resolved within the scope of this work. It is worth mentioning that much care was taken to rule out any effects on the results due to instrumentation. The distribution of the LDOS in these films was found to be highly temperature dependent. The parabolic nature of the distribution of LDOS was also consistent with the assumption in the VRH model proposed by Shklovskii and Efros, which was used to explain the conduction process in films deposited in oxygen rich atmospheres.

This was believed to be a first attempt to study the electronic structure of this class of material using STS and also no evidence has been found of any published work of STS performed above room temperatures.

8.2 SCOPE FOR FUTURE WORK

Although this study provided a good understanding of the structural and electrical properties of the $Ni_xMn_{3-x}O_{4+\delta}$ material system in bulk form and thin films, some issues remained unexplained. This final section is therefore intended to present some ideas for further experiments that might provide additional insight into the unresolved questions.

A change in the conduction mechanism was observed around 300K for the bulk materials but the reasons for this were not apparent. It would be useful to carry out temperature dependent x-ray diffraction, which would highlight any possible phase changes.

No quantitative data of charge distribution in materials with varying amounts of nickel could be obtained, although it was shown that the ratio of Mn^{3+} to Mn^{4+} was changing with varying amounts of Ni in the system. The situation was further complicated by a lack of knowledge of the oxygen stoichiometry and how this might affect the electrical properties. X-ray photoelectron spectroscopy (XPS) is one of the techniques, which could provide information as to the charge states and help to determine the charge distribution of the material. Similarly neutron diffraction can provide important information about the oxygen content in the material which it is not possible to obtain directly using x-ray diffraction. Neutron diffraction results together with results from XPS of the materials would provide comprehensive information on the role of varying amounts of nickel and oxygen in the material. It could also help to determine the relationship between the resistivity and these two factors, which can be used to produce material with a specific resistivity. Increasing the time of annealing should restore the oxygen stoichiometry of the materials sintered at different temperatures. However,

results of this work suggested that the annealing time might have to be very long in order to achieve that, which may not be attractive for commercial applications.

The effect of varying the annealing time for thin films should also provide interesting results, as this would change the oxygen stoichiometry of the films. Annealing films in a reducing atmosphere and in pure oxygen may provide good information about the effect of oxygen on the electrical characteristics. This may also provide additional information about the possible cause(s) of the different conduction mechanisms observed for films deposited in different oxygen containing ambients. Elemental analysis of the surface using Auger electron spectroscopy, together with CITS mapping would help in identifying the reasons for the inhomogeneities of the surface seen in the films.

The STS results provided an insight into the electronic structure of the material, however in the absence of a theoretical model it was difficult to interpret the results. Developing a model of the electronic structure would be a significant step towards understanding the electrical characteristics. It may also help in explaining the additional features in the STS spectra of the thin films. STS should also be carried out on bulk target material.

Preliminary STS results (not presented in this thesis) indicated that the grain boundaries may be electrically active and possibly play a role in the conduction process. This work needs to be carried out more extensively along with micro-measurement of resistance, similar to that used by Leach et. al. [6] across a single grain boundary and within one grain, which may provide invaluable information. The latter technique has an advantage over EBIC, as temperature dependent measurements can be carried out which is relatively difficult and expensive in case of EBIC.

Reconstruction of the film surface by repeated sputtering and annealing inside a STM would be another way of identifying the difference in characteristics between the grains and the grain boundaries. Although this technique is mostly applied to single crystals, it has been successfully carried out for polycrystalline TiO_2 [7], which is yet to be published. STM provides atomic resolution images highlighting any abnormalities on the surface.

In conclusion, a rf magnetron sputtering system has been designed and constructed and characterisation of the structure and electrical properties of the resulting films were carried out. The target was prepared from oxide precursors and characterisation of five different compositions of the $Ni_xMn_{3-x}O_{4+\delta}$ material system was done. Finally the electronic structure of the thin films was studied using STM/STS.

8.3 REFERENCES

- [1]. Mott, N.F., Davis, E.A. (1979) *Electronic Processes in Non-crystalline Materials*. Clarendon Press, Oxford.
- [2]. Shklovskii, B.I., Efros, A.L. (1984) *Electronic properties of doped semiconductors*. Springer - Verlag, Berlin.
- [3]. Zabrodskii, A.G. *Electrical conductivity of heavily doped compensated n-type germanium produced by neutron doping*, (1980) Soviet Physics Semiconductors, **14**, 670-676.
- [4]. Guinier, A. (1994) *X-ray diffraction in crystals, Imperfect crystals and amorphous bodies*. Dover Publications.
- [5]. Hase, T.P.A. (1999) *Condensed matter physics course: x-rays & neutrons*. University of Durham.
- [6]. Seaton, J., Leach, C. *Local property measurement in PTC thermistors*, (2002) Journal of European Ceramic Society, **In Submission**.
- [7]. Klusek, Z., Peirzgalski, S., Datta, P.K. *Investigation of defect states on reduced TiO₂ (110)-(1x1) surface by scanning tunneling spectroscopy*, (2002) Surface Science, **In Submission**.

List of Publications

NTC characteristics of bismuth based ceramic at high temperature

A Basu, A W Brinkman, and T Hashemi

Department of Physics, University of Durham, South Road, Durham, DH1 3LE, UK

Abstract

NTC characteristics of a ceramic based on Bi_2O_3 doped with TiO_2 , Ta_2O_5 and WO_3 have been studied over a temperature range of 100°C to 700°C. The material was pressed into pellets and sintered in air from 700°C to 1000°C at 100°C intervals for 14 hours. The microstructure was studied using SEM and evidence of a sintered body with grain sizes approximately 7-10 μ m was observed in the material fired at 1000°C. XRD analysis indicated the emergence of a monophasic material when sintered at 1000°C, which clearly verified along with the SEM studies, the completion of the sintering process. Electrical characterisation of the material was done by measuring the resistance and the capacitance over a temperature range of 100°C to 700°C, in air. The material showed good NTC characteristics over the whole range of temperature with thermistor constants $B = 4840$ K and $\Delta E = 386$ meV. The capacitance changed significantly over the temperature range ($\sim 10^{-11}$ F at 100°C to $\sim 10^{-6}$ F at 700°C).

Publication Details

International Journal of Inorganic Materials

Year 2001, Volume 3, Page 1219

In situ study of the effect of temperature on the electronic structure of $Ni_xMn_{3-x}O_{4+\delta}$ thin films using scanning tunneling spectroscopy

A Basu¹, A W Brinkman¹, Z Klusek², P K Datta², P Kowalczyk²

¹Department of Physics, University of Durham, South Road, Durham, DH1 3LE, UK

²Advanced Materials Research Institute, Northumbria University, Newcastle Upon Tyne, NE1 8ST, UK

Abstract

$Ni_xMn_{3-x}O_{4+\delta}$ ($0.4 \leq x \leq 1$) are a series of cubic spinel structured material exhibiting a negative temperature coefficient of resistance. The resistance as a function of temperature (T) has been measured from 20°C to 200°C and the data has been fitted to a variable range hopping model in which the resistivity is described as $\rho = \rho_0 T \exp(T_0/T)^{0.5}$ where T_0 was found to be 2.24×10^5 K. Scanning tunneling spectroscopy measurements were carried out over the temperature range of 20°C to 300°C, to study the shape of the local density of states (LDOS). The distribution of the LDOS around the Fermi level was parabolic in agreement with the model of variable range hopping. The evolution of a peak around 1.8eV was observed with increasing temperature and found to be completely reversible with temperature

Publication Details

Journal of Applied Physics

Year 2002, Volume 92, Page 4123

Effect of oxygen partial pressure on the NTCR characteristics of sputtered $Ni_xMn_{3-x}O_{4+\delta}$ thin films

A Basu, A W Brinkman and R Schmidt

Department of Physics, University of Durham, South Road, Durham, DH1 3LE, UK

Abstract

$Ni_xMn_{3-x}O_{4+\delta}$ are ceramic materials with a spinel structure exhibiting a negative temperature coefficient of resistivity (NTCR). This inherent property makes this class of material ideally suited for temperature sensing applications. Films of $Ni_xMn_{3-x}O_{4+\delta}$ were deposited on oxide coated <100> silicon (SiO_x), using rf magnetron sputtering in an oxygen / argon atmosphere with different oxygen partial pressures (0.3, 1, 2.5, 5, 7.5, 10, 12.5, 15 percent oxygen). A first set of films were annealed in air at 800°C for 1 hour and quenched to room temperature. A second set of films were annealed in an atmosphere similar to that used during deposition (oxygen / argon), at 800°C for 1 hour and quench cooled to room temperature. The resistance versus temperature measurements were done from room temperature up to 200°C and the data fitted to a variable range hopping model where the resistivity can be expressed as $C_0 T \exp(T_0/T)^{0.5}$. The characteristic temperature T_0 (range ~ 1.9×10^5 to 2.42×10^5 K) of the films was not noticeably different from the target material, with exception of the films deposited at low oxygen partial pressure, which showed higher values of T_0 (~ 3.1×10^5 K). The resistivity of the as-deposited films was dependent on the oxygen percentage in the ambient during sputtering, such that the resistance decreased with increasing oxygen. On annealing independent of the ambient, the resistivity of the films decreased considerably (~300 ohm cm). The films produced in ambients with higher oxygen had a resistivity in the as-deposited state similar to that of the annealed films and showed least variation on annealing.

Publication Details*Journal of European Ceramic Society**Year 2002, In Press*

Production of NTCR thermistor devices based on $NiMn_2O_{4+\delta}$

R Schmidt, A Basu and A W Brinkman

Department of Physics, University of Durham, South Road, Durham, DH1 3LE, UK

Abstract

$NiMn_2O_{4+\delta}$ ceramics exhibit a logarithmic increase of resistance with decreasing temperature (NTCR), which makes the compound well suited for use as a thermistor material in temperature sensing applications. In bulk material there are often problems with poor stability and reproducibility due to incomplete intergranular contact. These difficulties can be minimised in even and dense polycrystalline films. Screen-printing, electron-beam evaporation and rf magnetron sputtering processes have been developed for the production of thin and thick film NTCR thermistor devices. The source powder production, the experimental set-up, the process parameters and the resulting film properties for each of the processes are presented and compared. The surface topology was examined by scanning-electron microscopy (SEM) and atomic force microscopy (AFM). The phase purity of the source powder and the films was assessed by X-ray diffractometry (XRD). The electrical properties were analysed by measuring the resistance - temperature characteristics. This study suggests that rf magnetron sputtering processes are most advantageous.

Publication Details

Journal of European Ceramic Society

Year 2002, In Press

Effect of substrate temperature on the structural properties of rf magnetron sputter deposited $Ni_xMn_{3-x}O_{4+\delta}$ thin films

A Basu¹, A W Brinkman¹, T P A Hase¹, Z Klusek², S Pierzgalski² and P K Datta²

¹Department of Physics, University of Durham, South Road, Durham, DH1 3LE, UK

²Advanced Materials Research Institute, Northumbria University, Newcastle Upon Tyne, NE1 8ST, UK

Abstract

The material series $Ni_xMn_{3-x}O_{4+\delta}$ ($0.4 < x \leq 1$) display negative temperature coefficient characteristics and are often employed as temperature sensors. Thin films (thickness ~ 450 nanometers) have been produced on $\langle 100 \rangle$ silicon substrates using rf magnetron sputtering in an argon atmosphere at four different substrate temperatures (50° , 100°C , 200°C and 250°C) and subsequently annealed in air from 600°C to 900°C in steps of 50°C . X-ray diffraction studies showed that the films recrystallised from a nanocrystalline, near amorphous structure to a cubic spinel phase with a pronounced $\langle 100 \rangle$ orientation when annealed at 750°C . The preferred orientation along the $\langle 100 \rangle$ direction increases (intensity ratio I_{311} to I_{400} decreases) from 2.27 to 0.06 with increasing substrate temperature upto 200°C for films annealed at 800°C . The surface roughness and topography of as-deposited and recrystallised films were studied using atomic force microscopy. As-deposited films were characterised by agglomerations of small clusters of nano-sized grains with a surface roughness of $< 10\text{nm}$. Annealed films showed significant grain growth ($\sim 50\text{nm}$) with a simultaneous increase in surface roughness ($\pm 30\text{ nm}$) The lattice constant of the thin films was lower than the bulk target material.

Publication Details

Thin Solid Films

Year 2002, In submission

A study of the electronic states of $Ni_xMn_{3-x}O_{4+\delta}$ thin films using scanning tunneling microscopy and current imaging tunneling spectroscopy

A Basu¹, A W Brinkman¹, R Schmidt¹, Z Klusek², P Kowalczyk² and P K Datta²

¹Department of Physics, University of Durham, South Road, Durham, DH1 3LE, UK

²Advanced Material Research Institute, Northumbria University, Ellison Building, Newcastle Upon Tyne, NE1 8ST, UK

Abstract

$Ni_xMn_{3-x}O_{4+\delta}$ ($0.4 \leq x \leq 1$) are a series of spinel structured materials exhibiting NTCR characteristics. Thin films were produced on <100> silicon substrates using rf magnetron sputtering in an oxygen/argon atmosphere (2.5% oxygen). Following deposition, the films were annealed at 800°C in air and the crystalline structure studied using X-ray diffraction. Scanning tunneling microscopy (STM) was used to study the topology of the layers in both the as-deposited and annealed states. Annealing resulted in a more uniform and ordered structure. Tunneling conductance (dI/dV vs V) and normalised tunneling conductance $\{(dI/dV)/(1/V)$ vs $V\}$ characteristics were measured and used to generate conductance maps $\{dI/dV(x,y,eV)\}$ and to study the local density of states (LDOS) of the film surface. The tunneling conductance maps showed islands of bright contrast in an otherwise relatively uniform background of dark contrast. There were substantially fewer bright contrast islands in annealed films and they appear to bear no relation to any topographical features. The distribution of the LDOS in the bright regions was similar to that normally associated with metallic behaviour, while in the regions of dark contrast, the LDOS was more characteristic of semiconductors (LDOS ~ 0 at Fermi level). The resistance – temperature characteristics were measured and found to be consistent with conduction models based on electron hopping.

Publication Details

Journal of European Ceramic Society

Year 2002, In Press

